



BRNO UNIVERSITY OF TECHNOLOGY

VYSOKÉ UČENÍ TECHNICKÉ V BRNĚ

FACULTY OF MECHANICAL ENGINEERING

FAKULTA STROJNÍHO INŽENÝRSTVÍ

INSTITUTE OF AUTOMOTIVE ENGINEERING

ÚSTAV AUTOMOBILNÍHO A DOPRAVNÍHO INŽENÝRSTVÍ

FITTING AND EXTRAPOLATION OF TURBOCHARGER TURBINE MAPS

PROKLÁDÁNÍ A EXTRAPOLACE MAP TURBODMYCHADLOVÝCH TURBÍN

DOCTORAL THESIS

DIZERTAČNÍ PRÁCE

AUTHOR

AUTOR PRÁCE

Ing. Adam Vondrák

SUPERVISOR

ŠKOLITEL

prof. Ing. Josef Štětina, Ph.D.

BRNO 2021

ABSTRACT

Modelling of turbine performance is a prerequisite for detailed simulation of gas exchange in turbocharged combustion engines. At the same time, the possibility to determine efficiency and mass flow capacity at arbitrary operating points is key to comparing different turbine stages. The objective of this work is to propose a single method for both purposes, so it is possible to do the comparison using exactly the same turbine performance model as in subsequent engine working cycle simulation. The source of input data is typically a gas stand measurement, which enables capturing of limited turbine operating range only. In this work, methods are proposed to improve the fidelity and robustness of turbine performance extrapolation, while optimization is employed to find the best fit in terms of agreement between the model and the input data.

ABSTRAKT

Modelování turbínových charakteristik je nutným předpokladem pro detailní simulaci výměny náplně válce turbodmychadlem přeplňovaných spalovacích motorů. Kromě toho je možnost stanovení účinnosti a průtokové kapacity v libovolných pracovních bodech klíčová pro porovnání různých turbínových stupňů. Cílem této práce je předložit jednotnou metodu pro oba účely tak, aby bylo možné provést porovnání použitím přesně stejných modelů turbín jako při následné simulaci pracovního oběhu motoru. Zdrojem vstupních dat je obvykle měření na plynové zkušebně, které však umožňuje zachycení pouze omezeného pracovního rozsahu turbíny. V této práci jsou navrženy metody umožňující zvýšení věrohodnosti a robustnosti extrapolace turbínových charakteristik, přičemž optimalizace je využita k určení takových parametrů hledaných funkcí, které vedou k nejlepší shodě mezi modelem a vstupními daty.

KEYWORDS

turbine, map, fitting, extrapolation, turbocharger, turbocharging

KLÍČOVÁ SLOVA

turbína, charakteristika, prokládání, extrapolace, turbodmychadlo, přeplňování

ROZŠÍŘENÝ ABSTRAKT

Disertační práce se zabývá problematikou prokládání a extrapolace charakteristik turbodmychadlových turbín. Tyto mohou být získány například měřením na plynovém zkušebním zařízení (tzv. gas stand), turbínovém dynamometru nebo predikcí prostřednictvím CFD. Ve všech uvedených případech je výstupem soubor ustálených pracovních bodů mapující určitý rozsah provozních podmínek. Inženýrské aplikace však vyžadují, aby bylo možné stanovit vlastnosti turbíny v libovolném pracovním bodě. Typickým příkladem je porovnání účinností dvou různých turbín, které je třeba provést pro určitý expanzní poměr a korigované otáčky. Extrapolace pak hraje zásadní roli zejména při simulaci pracovního oběhu přeplňovaného spalovacího motoru. Turbodmychadla automobilů zpravidla pracují s výrazně pulsujícím přívodem spalin, který je dán počtem válců a otáčkovou frekvencí motoru. V takovém případě během jednoho pracovního cyklu výrazně kolísá expanzní poměr na turbíně, zatímco její otáčky se kvůli vysoké rychlosti celého děje téměř nemění. Simulační software proto musí mít možnost určit účinnost a hmotnostní průtok turbínou v širokém rozpětí pracovních podmínek, které zpravidla výrazně překračuje měřitelný rozsah na konvenčních zkušebních zařízeních.

Cílem práce je vytvořit aplikaci, která umožní uživateli automatizovanou tvorbu modelu turbíny na základě zadaných měřených dat a následné zpracování všech údajů. To zahrnuje, mimo jiné, vizualizaci extrapolovaných charakteristik, jejich porovnání a export pro použití v simulačních programech. Jako vývojové prostředí je zvolen MATLAB™. Mezi jeho výhody patří podpora návrhu aplikací s grafickým uživatelským rozhraním, knihovna předpřipravených ovládacích a zobrazovacích prvků nebo možnost spuštění kódu bez předchozí kompilace.

V prvním kroku je analyzována metoda extrapolace turbínové mapy využívaná v průmyslově rozšířeném nástroji pro simulaci pracovního oběhu přeplňovaného spalovacího motoru GT-SUITE™. Vzhledem ke komerční povaze daného software však není příslušný algoritmus detailně zdokumentován v dostupných informačních zdrojích. Proto je nutné implementovat jednotlivé fáze procesu s použitím vhodných numerických postupů.

Klíčovým aspektem zkoumané metody je identifikace pracovních bodů, ve kterých turbína pracuje s maximální účinností. Výstupem je závislost optimálních korigovaných otáček na expanzním poměru. Tyto body však obecně nejsou obsaženy mezi výsledky měření na zkušebních zařízeních, a proto musí být parametry prokládaných funkcí odhadnuty. Předmětný model turbíny je tvořen pěti charakteristickými funkcemi, ze kterých tři popisují provoz s maximální účinností a dvě extrapolaci do oblastí s nižší účinností. Zatímco parametry určující extrapolaci do sub-optimálních pracovních režimů lze odhadnout pomocí lineární regrese, závislosti spojené s provozem při maximální účinnosti jsou nelineární a musí být stanoveny pomocí optimalizačních metod.

V navržené implementaci výchozí metody prokládání a extrapolace turbínových map je využíván postup cyklické optimalizace, při které jsou nejprve hledány parametry lineární funkce aproximující optimální rychlostní poměr turbíny v závislosti na expanzním poměru. V druhém kroku je zpřesňován splajn charakterizující maximální účinnost v závislosti na korigovaných otáčkách. Třetí krok zahrnuje tutéž proceduru pro optimální korigovaný průtok. Celý proces se

opakuje, dokud není splněna podmínka pro ukončení optimalizace. Účelovou funkcí je střední kvadratická odchylka měřených pracovních bodů od modelu turbíny, která je postupně minimalizována.

Kvalita získaného modelu turbíny je hodnocena metodami statistické analýzy a vizuální kontrolou plně extrapolovaných map účinnosti a korigovaného hmotnostního průtoku. V prvním případě je studován rozdíl mezi měřenými daty a numerickým modelem, přičemž jsou vyhodnoceny minimální, maximální, průměrná, mediánová, průměrná absolutní a střední kvadratická odchylka. Vizuální kontrola pak slouží především k odhalení případné deformace očekávaných průběhů sledovaných veličin v extrapolovaných oblastech vygenerovaných map. Právě druhý z uvedených postupů umožnil identifikaci nežádoucího zkreslení průtokové charakteristiky vzorové radiální turbíny v oblasti nízkého expanzního poměru, kde se očekává výrazný pokles hmotnostního průtoku s rostoucími otáčkami působením odstředivých sil (vstupní data byla získána měřením na plynovém zkušebním zařízení).

V důsledku výše popsaného pozorování je prozkoumána možnost použití teorie radiální rovnováhy v rotující tekutině pro stanovení závislosti expanzního poměru na otáčkách turbíny při nulovém hmotnostním průtoku. Tímto způsobem lze analyticky vyčíslit jeden ze dvou nezávislých parametrů charakteristické funkce určující extrapolaci korigovaného hmotnostního průtoku. Současně však dochází u vzorové turbíny ke zkreslení extrapolace při vysokém expanzním poměru. Zatímco odchylka měřených bodů od modelu zůstává nízká, křivky konstantních otáček jsou v této oblasti zhuštěny, což opět odporuje očekávanému trendu s účinkem odstředivých sil (korigovaný hmotnostní průtok by měl klesat s rostoucími otáčkami turbíny).

Pro hlubší pochopení sledovaného fenoménu je zkoumána analogie mezi průtokem turbínou a izoentropickým výtokem ideální tryskou. Zásadní roli zde hraje především bod zahlcení, který souvisí s dosažením rychlosti zvuku v nejužším místě ideální trysky a má za následek limitaci korigovaného hmotnostního průtoku. Reálná turbína sice nemá parametry ideální trysky, lze však konstatovat, že při určitém expanzním poměru dosáhne proudící plyn v některé části turbínového stupně rychlosti zvuku a s tím souvisejícího zahlcení. Při nulových otáčkách turbíny navíc hmotnostní průtok neovlivňuje účinek odstředivých sil v rotoru. Současně lze poukázat na skutečnost, že korigovaný hmotnostní průtok při nulových otáčkách je určen jako násobek optimálního korigovaného hmotnostního průtoku. Ve stavu zahlcení tudíž musí mít korigovaný hmotnostní průtok konstantní průběh jak pro nulové, tak pro optimální otáčky turbíny. Tento závěr je však v rozporu s topologií charakteristické funkce modelu turbíny popisující optimální rychlostní poměr. Vzhledem k tomu, že se jedná zpravidla o neklesající lineární funkci, optimální korigované otáčky rostou s expanzním poměrem.

Aby mohl korigovaný hmotnostní průtok při optimálních otáčkách zůstat konstantní, křivky konstantních korigovaných otáček turbíny by se musely asymptoticky sblížovat s rostoucím expanzním poměrem, což neodpovídá provedenému měření. Navíc, pokud by byla teorie radiální rovnováhy použita pro aproximaci účinku odstředivých sil za podmínek nenulového hmotnostního průtoku, výsledný vztah by byl nezávislý na expanzním poměru (tzn. křivky konstantních korigovaných otáček by byly při zahlcení turbíny paralelní). Jedinou

možností, jak současně splnit všechny uvedené podmínky, je limitace optimálních korigovaných otáček v okamžiku zahlcení průtoku turbínou.

Druhá část práce se zabývá návrhem nového modelu turbíny, který zohledňuje režim zahlcení a umožňuje limitaci maximálních korigovaných otáček. Hlavní změnou oproti referenčnímu modelu je náhrada lineární charakteristické funkce popisující optimální rychlostní poměr splajnem, jehož hodnota je nad kritickým expanzním poměrem konstantní. Současně je upravena funkce pro výpočet rychlostního poměru tak, že se v okamžiku zahlcení využívá kritická izoentropická výtoková rychlost. Díky tomu jsou konstantní také optimální korigované otáčky turbíny za konstantního optimálního rychlostního poměru při zahlcení.

Na tomto místě je vhodné poukázat na skutečnost, že rychlostní poměr je také měřítkem pro zatížení turbíny. Tedy optimální rychlostní poměr lze interpretovat jako optimální otáčky pro určitý expanzní poměr, které společně představují optimální zatížení. Změna otáček naopak vede ke zhoršení účinnosti, což je dáno zejména odchýlením od ideálního náběžného úhlu proudění na lopatkách turbíny. V režimu zahlcení průtoku je rychlost proudění vstupujícího do turbínového kola nezávislá na celkovém expanzním poměru, takže pro dosažení ideálního úhlu náběhu by měly být konstantní také otáčky turbíny. Z toho důvodu lze považovat postup limitace optimálních korigovaných otáček turbíny při zahlcení průtoku za oprávněný.

Nový model turbíny je testován v pěti fázích. Nejprve je použit pro aproximaci vzorových dat získaných měřeními na plynovém zkušebním zařízení. V tomto případě došlo k podstatnému snížení střední kvadratické odchylky mezi zadanou a modelovanou účinností, na straně hmotnostního průtoku se odchylka mírně zvýšila. Zásadní je však průběh extrapolovaného korigovaného hmotnostního průtoku, který nyní splňuje požadavky na rozlišení účinku odstředivých sil a režimu zahlcení.

V druhém kroku je algoritmus ověřen na datech získaných měřeními na turbínovém dynamometru, kdy byla opět dosažena velmi dobrá shoda s modelem včetně očekávaných průběhů extrapolovaného korigovaného hmotnostního průtoku.

Třetí fází je vykreslení složených grafů mapujících účinnost a průtokovou kapacitu pro různé velikosti turbínových stupňů. Tímto způsobem je nový aproximační algoritmus ověřen na desítkách map, přičemž získané průběhy sledovaných veličin potvrzují očekávané trendy maximální účinnosti v závislosti na velikosti rozváděcí spirály (tzv. A/R parametru) a turbínového kola.

Čtvrtou fází je import získaných modelů vzorové turbíny měřené na plynovém zkušebním zařízení a dynamometru do programu pro simulaci pracovního oběhu přeplňovaného spalovacího motoru (GT-SUITE). Na základě porovnání extrapolovaných charakteristik získaných modelováním výchozí metodou programu GT-SUITE a navrženým algoritmem lze konstatovat, že obě metody dosáhly podobného výsledku v případě dat pocházejících z plynového zkušebního zařízení, větší rozdíl je však patrný u mapy měřené na dynamometru. S výchozím algoritmem lze u obou map pozorovat zhuštění křivek konstantních korigovaných otáček v průtokových charakteristikách při nízkém expanzním poměru, což značí potlačení efektu odstředivých sil. V případě mapy získané měřeními na dynamometru je navíc patrný náhlý propad účinnosti v oblasti

nízkých korigovaných otáček, který je způsobený absencí měřených pracovních bodů s maximální účinností. Dále jsou mezi oběma metodami patrné odchylky v extrapolaci korigovaného hmotnostního průtoku při vysokém expanzním poměru, což lze přičíst absenci režimu zahlcení u výchozího algoritmu.

V poslední fázi testování jsou připravené modely turbíny využity pro simulaci pracovního oběhu přeplňovaného spalovacího motoru pracujícího ustáleně při plném zatížení a v přechodových režimech. V případě map získaných měření na plynovém zkušebním zařízení lze konstatovat dobrou shodu výkonových parametrů motoru v obou pracovních režimech pro novou i výchozí metodu aproximace. Při použití dat obdržných měření na turbínovém dynamometru však dochází k výraznému zpomalení nárůstu točivého momentu motoru v přechodových režimech s výchozím modelem turbíny, které je dáno zkreslením účinnosti při nízkých korigovaných otáčkách. Rozdíly jsou však patrné i mezi dosaženým točivým momentem motoru při ustáleném provozu s plným zatížením v nízkých otáčkách.

Vytvořená metodika umožňuje přípravu numerických modelů turbínových stupňů na základně experimentálních dat získaných měřeními na plynovém zkušebním zařízení nebo turbínovém dynamometru. Pro usnadnění celého procesu byla na platformě MATLAB vyvinuta aplikace s grafickým uživatelským rozhraním, která disponuje nástroji jak pro vizualizaci a porovnání samotných charakteristik, tak pro jejich export za účelem následné simulace pracovního oběhu přeplňovaného spalovacího motoru ve specializovaných programech. Proces tvorby modelu je přitom automatizovaný a robustní vůči proměnlivosti měřených dat. Díky implementaci SQLite databáze je navíc aplikace připravena pro správu většího množství vstupních údajů i hotových modelů, které lze kombinovat s cílem mapování trendů napříč produktovým portfoliem.

V rámci budoucího rozvoje práce se očekává zejména zpřesnění charakteristické funkce modelu turbíny, která popisuje optimální rychlostní poměr v závislosti na expanzním poměru. Podle současné definice je příslušný splajn složen ze tří částí, přičemž zakřivení středního úseku je řízeno pouze předepsanými prvními derivacemi v koncových bodech daného intervalu. Dalším krokem bude rozšíření podporovaných technologií na straně turbíny, jako jsou variabilní geometrie rozváděcích lopatek, zdvojená rozváděcí spirála apod. V širším časovém horizontu bude přínosné navázat na soudobý trend odděleného řešení některých aspektů modelování turbodmychadla. Jedná se především o přestup tepla mezi jednotlivými součástmi, pracovními médii a okolím, ale také o třecí ztráty v uložení rotoru. Účinky těchto procesů jsou za normálních okolností obsaženy v mapách získaných měřeními na plynové zkušebně, a proto musí být odebrány před zahájením takto rozšířených simulací.

BIBLIOGRAPHIC CITATION

VONDRÁK, Adam. *Fitting and Extrapolation of Turbocharger Turbine Maps*. Brno, 2021. Available also at: <https://www.vutbr.cz/studenti/zav-prace/detail/130074>. Doctoral thesis. Brno University of Technology, Faculty of Mechanical Engineering, Institute of Automotive Engineering. Supervisor Josef Štětina.

BIBLIOGRAFICKÁ CITACE

VONDRÁK, Adam. *Prokládání a extrapolace map turbodmychadlových turbín*. Brno, 2021. Dostupné také z: <https://www.vutbr.cz/studenti/zav-prace/detail/130074>. Dizertační práce. Vysoké učení technické v Brně, Fakulta strojního inženýrství, Ústav automobilního a dopravního inženýrství. Vedoucí práce Josef Štětina.

STATUTORY DECLARATION

I declare that this is my original work, which I created under the supervision of prof. Ing. Josef Štětina, Ph.D., using the information sources listed in references.

31st August 2021

.....
Ing. Adam Vondrák

ČESTNÉ PROHLÁŠENÍ

Prohlašuji, že tato práce je mým původním dílem, které jsem vypracoval pod vedením prof. Ing. Josefa Štětiny, Ph.D. a s použitím podkladů uvedených v seznamu zdrojů.

31. srpna 2021

.....
Ing. Adam Vondrák

ACKNOWLEDGEMENTS

This work could be completed thanks to the key resources provided by Garrett Motion Inc.

Many thanks to prof. Ing. Josef Štětina, Ph.D., the director of the Institute of Automotive Engineering at the Faculty of Mechanical Engineering of the Brno University of Technology, for his guidance and valuable consultations throughout my study.

With great gratitude, I acknowledge the tireless support from my family.

PODĚKOVÁNÍ

Tato práce mohla být vytvořena díky klíčovým zdrojům poskytnutým společností Garrett Motion Inc.

Mnohokrát děkuji prof. Ing. Josefu Štětinovi, Ph.D., řediteli Ústavu Automobilního a dopravního inženýrství při Fakultě strojního inženýrství Vysokého učení technického v Brně, za jeho vedení a cenné konzultace během celého mého studia.

S velkou vděčností oceňuji neúnavnou podporu od mé rodiny.

CONTENTS

INTRODUCTION	10
1 THEORETICAL BACKGROUND	11
1.1 TURBOCHARGING.....	11
1.1.1 Working principle of turbomachinery	13
1.1.2 Main turbomachinery stage design features	15
1.1.3 Static versus total quantities.....	17
1.1.4 Turbocharger performance mapping	18
1.1.5 Compression process	22
1.1.6 Expansion process	24
1.1.7 Corrected and reduced parameters	25
1.1.8 Blade speed ratio.....	28
1.1.9 Engine-turbocharger interaction.....	29
1.1.10 State-of-the-art turbine fitting process	31
1.2 INTERPOLATION	32
1.2.1 Polynomial interpolation	32
1.2.2 Linear spline interpolation.....	33
1.2.3 Cubic spline interpolation.....	34
1.3 CURVE FITTING.....	35
1.3.1 Linear least squares fitting	36
1.3.2 Least squares fitting using optimization	37
1.3.3 Descriptive statistics.....	38
1.4 OPTIMIZATION	40
1.4.1 Golden-section search	41
1.4.2 Quadratic fit method.....	42
1.4.3 Simplex method.....	43
1.4.4 Gradient descent method.....	45
1.4.5 Newton's multi-dimensional method.....	47
2 BASIC TURBINE FITTING METHOD	50
2.1 FITTING THE PERFORMANCE MODEL.....	50
2.1.1 Pre-processing of input data	50
2.1.2 Fitting the optimum blade speed ratio.....	51
2.1.3 Fitting the maximum efficiency.....	52

2.1.4	<i>Fitting the normalized efficiency</i>	53
2.1.5	<i>Fitting the optimum corrected mass flow rate</i>	54
2.1.6	<i>Fitting the normalized mass flow rate</i>	55
2.2	BACK-CALCULATION OF TURBINE PERFORMANCE.....	56
2.3	FIT QUALITY ASSESSMENT.....	59
2.3.1	<i>Statistical analysis</i>	59
2.3.2	<i>Analytical approach</i>	61
2.3.3	<i>Robustness check</i>	63
2.4	SENSITIVITY STUDY.....	64
2.4.1	<i>The shape of the optimum BSR function</i>	64
2.4.2	<i>The shape of the normalized ETATM function</i>	67
2.4.3	<i>The shape of the normalized WT function</i>	68
3	OPTIMIZATION OF TURBINE MODEL PROPERTIES	69
3.1	OPTIMUM BSR FUNCTION.....	69
3.2	MAXIMUM EFFICIENCY FUNCTION.....	74
3.3	OPTIMUM CORRECTED MASS FLOW RATE FUNCTION.....	77
3.4	COMPLETE TURBINE FITTING ALGORITHM.....	79
3.5	EVALUATION.....	81
4	NEW TURBINE FITTING ALGORITHM	82
4.1	RADIAL EQUILIBRIUM.....	82
4.2	IDEAL NOZZLE ANALOGY.....	86
4.3	OPTIMUM CORRECTED SPEED LIMITATION.....	88
4.4	FIT QUALITY.....	93
4.5	REMARKS ON IMPLEMENTATION.....	94
4.6	ROBUSTNESS CHECK.....	96
5	APPLICATIONS OF FITTED TURBINE MAPS	98
5.1	MAP DATABASE & FITTING WORKFLOW.....	98
5.2	COMPARISON OF TURBINE PERFORMANCE.....	100
5.3	COMPOUND CHARTS.....	105
5.4	SIZE EFFECT.....	107
5.5	ENGINE SIMULATION.....	108
5.5.1	<i>Steady-state performance with the gas stand map</i>	108
5.5.2	<i>Steady-state performance with the dyno map</i>	110

5.5.3	<i>Transient load step with the gas stand map</i>	112
5.5.4	<i>Transient load step with the dyno map</i>	113
CONCLUSION	115
REFERENCES	117
LIST OF AUTHOR'S PUBLICATIONS	119
DEFINITIONS/ABBREVIATIONS	120

INTRODUCTION

Turbocharged combustion engines represent, as of today, the main building block of most road vehicle powertrains. Ranging from the smallest to the largest, they can be found in all passenger and freight means of transport, as well as in off-highway and stationary applications. In the context of increasing climate protection efforts, it is of high importance to sustain continuous improvement of our technologies. This is only made possible by means of accurate simulation tools, which allow engineers to predict the impact of their innovative ideas.

Modelling of turbocharger performance is an important part of combustion engine development. Although working solutions are integrated in existing commercial software to enable simulations of boosted engine working cycles, tools for post-processing of measured or CFD predicted data are less common. Therefore, the main objective of this work is to develop an application that will allow engineers to visualize and compare the performance of different turbine stages. To study the trade-offs between efficiency and corrected mass flow rate at equal operating conditions, however, the scattered input data must be fitted by a mathematical model.

Contemporary industrial solutions include algorithms of diverse complexity. Simple algebraic models (e.g. Jensen et al. [17]) are commonly applied for control purposes, because they can be evaluated quickly even on low-power machines such as engine ECU's. Non-linear models, on the other hand, are used in simulation software (e.g. GT-SUITE™ [23]) and their biggest advantage is more accurate extrapolation. The most complex type is based on a mean-line turbine design theory (e.g. RITAL™ [26]), which uses physics principles to determine the average flow conditions in each part of a turbine stage. While such models enable physically accurate extrapolation, their biggest disadvantage is the requirement of detailed geometrical inputs.

The application in development will be equipped with a non-linear turbine performance model, the properties of which will be identified using optimization techniques. MATLAB™ is selected as the development environment, because it is suitable for both functional coding and graphical user interface design. In addition, an SQLite database will be used as storage for raw measured data and fitted models to facilitate database operations such as searching, filtering, or aggregation. To make sure engine performance is predicted using the same turbine model, an export function will be integrated. By this, it will be possible to generate fully extrapolated maps to be imported in engine simulation software (in the so-called *grid* format in the case of GT-SUITE).

Another advantage of the implementation of a database system is that it will make it possible to study trends spanning multiple turbine stages of varying properties, like e.g. the relationship between the maximum efficiency and the wheel size within the portfolio of certain aerodynamic design. To enable the creation of such a chart, however, the database will have to be filled with a set of fitted turbine maps covering not only the complete range of wheel diameters, but also some span of volute sizes (described by the so-called A/R parameter). Due to this, it will be possible to estimate the maximum efficiency achievable with each wheel size.

Finally, engine performance will be simulated using turbine models fitted by both the default and proposed methodologies.

1 THEORETICAL BACKGROUND

Modelling of turbine performance of automotive turbochargers is a complex, multi-disciplinary task. It spans the fields of turbomachinery, combustion engines, mathematics and computer programming. The product is, nevertheless, indispensable for engineering simulations and related operations, like the comparisons of turbine efficiency and mass flow capacity. In this work, an application is developed, the purpose of which is to facilitate pre-processing of measured turbine characteristics, so it is easier to select the best candidate for matching to a combustion engine. The basic concepts required to achieve this goal are explained in the following chapters.

1.1 Turbocharging

Turbochargers belong to a group of machines called turbomachinery. Their purpose is to transform the available energy of a flowing fluid into mechanical work on a shaft and vice versa. While the earlier is done by a turbine, the latter is the job of a pump (liquids) or a compressor (gases). A typical turbocharger consists of a turbine and a compressor, both of which are mounted on the same shaft (see Figure 1).

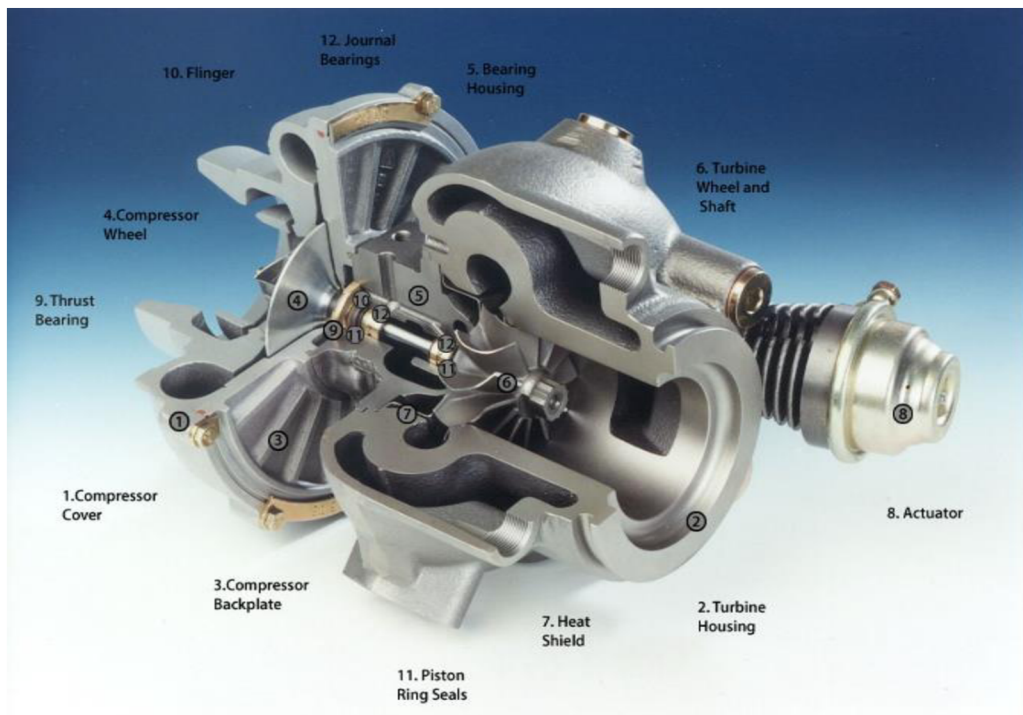


Figure 1: Turbocharger section view [21]

The task of a turbocharger is to push air into the cylinders of a combustion engine, so it can burn more fuel and produce more power. The proportion between the amounts of air and fuel in the mixture is given by the stoichiometric ratio and the excess air ratio. Under these conditions, the engine power output can be expressed as [1, 3, 5]

$$P_e = \eta_e \dot{m}_{air} \frac{H_u}{L_t \lambda} \quad (1)$$

where P_e [W] is the engine brake power, η_e [-] is the overall engine efficiency, \dot{m}_{air} [kg/s]

is the air mass flow rate, H_u [J/kg] is the fuel lower heating value, L_t [-] is the stoichiometric ratio and λ [-] is the air excess ratio. While a stoichiometric ratio determines the ideal amount of fuel that can be completely burned with a certain amount of air, a lambda is the extent to which the actual air charge exceeds or falls behind the theoretical demand. It is common that petrol engines (spark-ignited) are operated mostly close to the stoichiometric conditions, whereas diesel engines (compression-ignited) are always running lean (with air excess). The average air mass flow through a piston engine depends on several factors, including the intake air density and the total cylinder displacement [1, 2, 3]

$$\dot{m}_{air} = \eta_v \rho_{int} V_d \frac{n_e}{60\tau} \quad (2)$$

where η_v [-] is the volumetric efficiency, ρ_{int} [kg/m³] is the intake air density, V_d [m³] is the total cylinder displacement, τ [-] is the number of crankshaft revolutions per one engine cycle (a four-stroke engine needs two revolutions) and n_e [1/min] is the engine speed. Volumetric efficiency is a factor that represents the effect of valve timing combined with the dynamics of the intake and exhaust gases, all of which influence the amount of charge trapped in the cylinders. It can be determined either experimentally, or by simulation (e.g. using 1D engine gas dynamics software). The quantity that can be influenced by a turbocharger is the intake air density. Based on the ideal gas equation of state, it depends on the pressure and temperature of the intake air [1, 2, 3, 5, 9]

$$\rho_{int} = \frac{p_{int}}{r_{air} T_{int}} \quad (3)$$

where p_{int} [Pa] is the intake air pressure, r_{air} [J/(kg·K)] is the specific gas constant and T_{int} [K] is the intake air temperature. A compressor adds energy to the intake air flow by increasing its pressure and temperature. A common practice is to cool the flow down in a heat exchanger placed upstream of the cylinder head, making the density grow even higher (see Figure 2). The power needed to drive the compressor is generated by the turbine, which is propelled by exhaust gases created as a product of combustion in the engine. The transfer of mechanical power is performed by a shaft. [2, 3, 5]

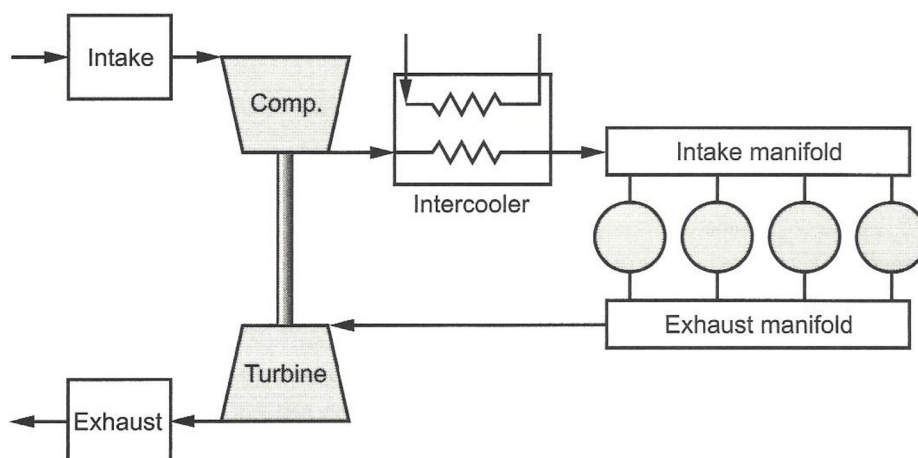


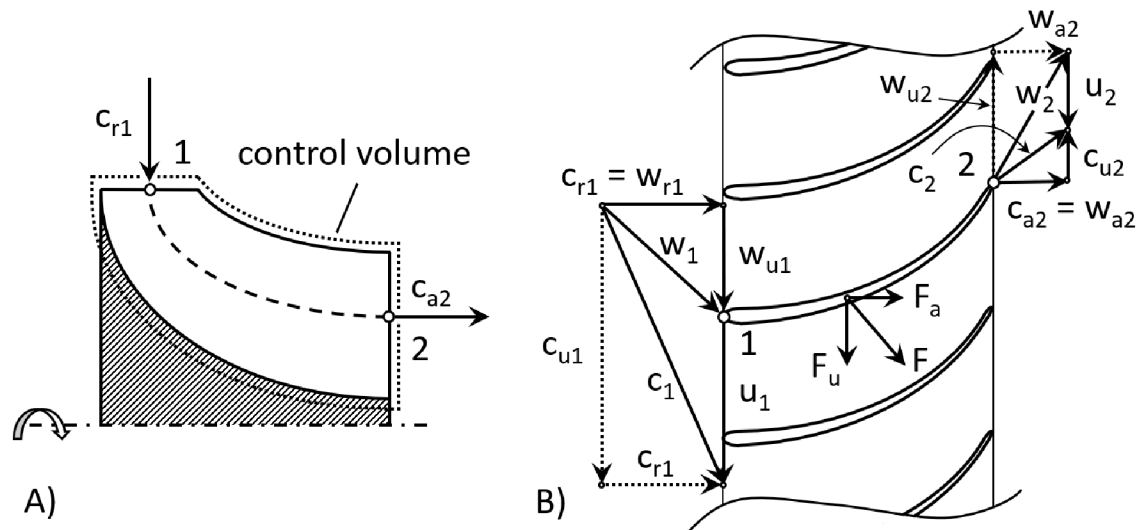
Figure 2: Turbocharged engine gas flow scheme [3]

1.1.1 Working principle of turbomachinery

Turbomachinery enables power transfer between a flowing fluid and the shaft. The solid parts in interaction with the working gas or liquid are typically the blades; however, bladeless machines exist too (e.g. the Tesla turbine). A blade row forms channels between each pair of blades that the working fluid must pass through and, due to the blade curvature, changes its direction of flow (see Figure 3). By that the vector of momentum of the flowing fluid is changed, which is linked to a force according to Newton’s second law of motion [2, 4]

$$\mathbf{F}_f = \frac{d\mathbf{H}_f}{dt} \tag{4}$$

where \mathbf{F}_f [N] is the vector of force acting on the fluid, \mathbf{H}_f [kg·m/s] is the vector of momentum of the fluid passing through the blade channels, t [s] stands for time.



Quantities:

- u – wheel circumferential velocity at the mean-flow radius
- c – absolute gas velocity (stationary frame of reference)
- w – relative gas velocity (rotating frame of reference)
- F – aerodynamic force acting on the blade row

Indices:

- 1 – wheel inlet
- 2 – wheel outlet
- r – radial
- u – circumferential
- a – axial

Figure 3: Radial turbine wheel cross-section (A) and velocity triangles in an unfolded blade row view (B)

According to Newton’s third law of motion, the fluid and the blade channel walls are subjected to forces of the same magnitude, yet acting in opposite directions [2, 4]

$$\mathbf{F} = -\mathbf{F}_f \tag{5}$$

where \mathbf{F} [N] is the vector of force acting on the blade channel walls. To get the full information about the aerodynamic pressure distribution on the blades, a CFD solver would be needed. In the early stages of turbomachinery design, the aim is usually to determine the overall force acting on the blading, which can be obtained as the sum of momentum fluxes entering or exiting the control volume (see Figure 3) [2, 4]

$$\mathbf{F}_{f_overall} = \sum_i \dot{\mathbf{H}}_{f_i} \quad (6)$$

where $\mathbf{F}_{f_overall}$ [N] is the vector of force acting on the fluid in the control volume, i [-] is the index of each control volume inlet or outlet area. A momentum flux is defined as the amount of momentum entering or leaving the control volume per unit of time [2, 4]

$$\dot{\mathbf{H}}_f = \dot{m} \mathbf{c} \quad (7)$$

where $\dot{\mathbf{H}}_f$ [kg·m/s²] is the momentum flux, \dot{m} [kg/s] is the mass flow rate, \mathbf{c} [m/s] is the vector of fluid velocity in the stationary frame of reference (assumed constant). In the case of a blade channel, there is one inlet and one outlet flow (see Figure 3). For the initial aerodynamic assessment, it is common to reduce the inlet and outlet areas to the so-called mean-flow points (see points 1 & 2 in Figure 3). The average fluid velocity and density are considered in each. This is also referred to as the *mean-flow design*. The overall momentum flux through the control volume is calculated as [2, 4]

$$\dot{\mathbf{H}}_{f_overall} = \dot{m}_1 \mathbf{c}_1 + \dot{m}_2 \mathbf{c}_2 \quad (8)$$

where $\dot{\mathbf{H}}_{f_overall}$ [kg·m/s] is the overall momentum of the fluid enclosed in the blade channels, \dot{m}_1 [kg/s] is the inlet mass flow rate, \dot{m}_2 [kg/s] is the outlet mass flow rate, \mathbf{c}_1 [m/s] is the vector of speed in the inlet to the control volume, \mathbf{c}_2 [m/s] is the vector of speed in the outlet from the control volume. In engineering applications, power transfer on the shaft is sought for in the first place. It can be calculated as a product of torque acting on the rotor and the angular velocity of the shaft [2, 4]

$$P_{shaft} = \mathbf{M} \boldsymbol{\omega} \quad (9)$$

where P_{shaft} [W] is the shaft power, \mathbf{M} [N·m] is the vector of torque acting on the rotor, $\boldsymbol{\omega}$ [rad/s] is the rotor angular velocity. The torque on the blading is of the same size, but acting in the opposite direction compared to the overall torque acting on the working fluid. Following the mean-flow design approach, it can be determined at the inlet and at the outlet points as (see Equations 5, 6 and 8) [2, 4]

$$\mathbf{M} = -(\dot{m}_1 \mathbf{c}_1 \times \mathbf{r}_1 + \dot{m}_2 \mathbf{c}_2 \times \mathbf{r}_2) \quad (10)$$

where \mathbf{r}_1 [m] is the vector of inlet mean-flow radius and \mathbf{r}_2 [m] is the vector of outlet mean-flow radius. In the case of a radial turbine, the inlet mean-flow radius is one half of the maximum wheel diameter (see Figure 3). At the outlet, however, the mean-flow radius divides the annulus section in two parts of the same area (even distribution of mass flow is assumed). As each part is again an annulus, the mean-flow radius can be determined as a quadratic mean of the minimum and maximum radii [2, 4]

$$r_2 = \frac{1}{2} (r_{2_min}^2 + r_{2_max}^2) \quad (11)$$

where r_{2_min} [m] is the vector of hub radius at the outlet and r_2 [m] is the vector of blade tip radius at the outlet. Based on Equations 9 & 10, the shaft power is

$$P_{shaft} = -(\dot{m}_1 \mathbf{c}_1 \times \mathbf{r}_1 + \dot{m}_2 \mathbf{c}_2 \times \mathbf{r}_2) \boldsymbol{\omega} \quad (12)$$

Since vectors \mathbf{r}_1 and \mathbf{r}_2 are perpendicular to the shaft axis of rotation, Equation 12 can be simplified as follows

$$P_{shaft} = -(\dot{m}_1 c_{u1} u_1 + \dot{m}_2 c_{u2} u_2) \quad (13)$$

where c_{u1} [m/s] is the circumferential component of fluid speed in the inlet to the control volume, u_1 [m/s] is the circumferential speed of the blading at the inlet to the control volume, c_{u2} [m/s] is the circumferential component of fluid speed in the outlet from the control volume and u_2 [m/s] is the circumferential speed of the blading at the outlet from the control volume. Due to the conservation of mass

$$\dot{m}_1 = -\dot{m}_2 \quad (14)$$

Putting Equations 13 and 14 together yields the Euler equation, which is also referred to as the basic equation of turbomachinery [2, 4]

$$\frac{P_{shaft}}{\dot{m}} = -\Delta h_{tot} = c_{u1} u_1 - c_{u2} u_2 \quad (15)$$

where \dot{m} [kg/s] is the mass flow rate through a blade row, Δh_{tot} [J/kg] is the change of total enthalpy of the working fluid (at stagnation conditions, see Chapter 1.1.3). From Equation 15 follows that the power produced or consumed by a turbomachine depends on the change of swirl of the working fluid and the rotor speed. While the direction of flow is largely driven by the inlet and the outlet blade angles, the circumferential velocity of the rotor is closely related to the geometry of the stage.

1.1.2 Main turbomachinery stage design features

A typical automotive turbocharger consists of a radial compressor and a radial turbine, but there are other types of machines too, the distinguishing parameter of which is the main flow direction (see Figure 4).

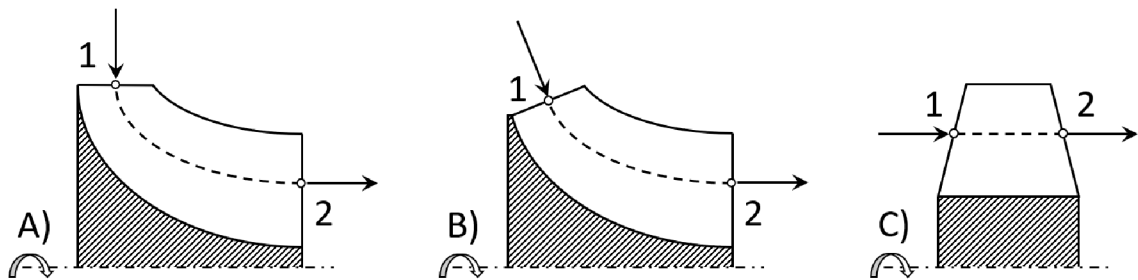


Figure 4: Turbine wheel types according to the main direction of flow (A – radial, B – mixed-flow, C – axial)

In the case of a radial turbine, the inlet point is located at a bigger radius than the outlet, where the blade circumferential velocity is lower. It means that if there were an axial and a radial turbine with the same inlet point radii, gas and rotor angular velocities, the radial turbine would produce a larger specific power. [2, 3, 4, 5]

Another important implication of Equation 15 is that shaft power is proportional to the change of state of the working fluid, which is related to the total specific enthalpy difference. As the fluid is a gas on both the compressor and turbine sides, the process can be generally described as polytropic. In the engineering praxis, however, it is desired to identify an ideal case to compare the real process with, so one can establish a gauge of efficiency. For this purpose, the isentropic process is usually used. [2, 3, 4, 5]

Apart from the main flow direction, the volute design has a major implication on the overall performance of a turbomachine too. The so-called A/R parameter indicates the ratio between the volute cross section area and the distance from its centre of gravity to the axis of rotation (see Figure 5). It determines mainly the flow capacity, but there is certain impact on the efficiency too (see Chapter 5.3). [2, 3, 4, 5]

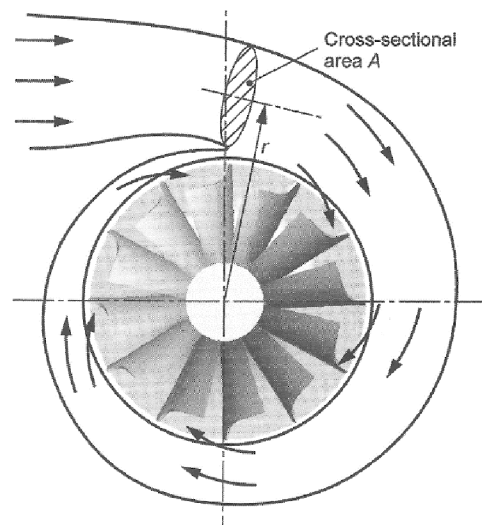


Figure 5: Definition of the A/R parameter of a turbine volute (r is the distance from the axis of wheel rotation to the centre of gravity of the area A) [3]

Another feature, which is widely used to calibrate the stage flow capacity of both turbines and compressors, is the trim. It indicates the blade length at the smaller end of the wheel (compressor inlet or turbine outlet) and impacts the complete shroud contour (see Figure 6). [2, 3, 5]

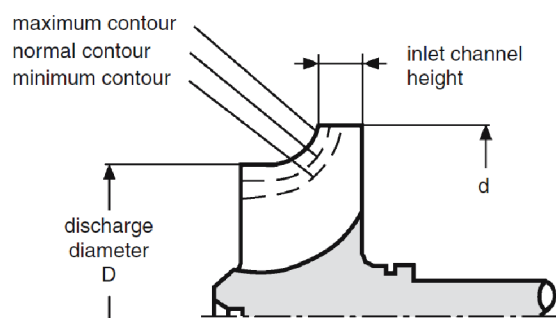


Figure 6: Definition of the wheel trim [5]

Numerically is the wheel trim defined as the ratio between the squares of the smaller and the bigger wheel diameter [2, 3, 5]

$$Trim = 100 \frac{d_W^2}{D_W^2} \quad (16)$$

where $Trim$ [%] is the wheel trim, d_W [mm] is the smaller wheel diameter and D_W [mm] is the bigger wheel diameter.

1.1.3 Static versus total quantities

In thermodynamics, state quantities of fluid flows can be divided in two main groups, namely the static and the total (also referred to as stagnation). The concept of the total fluid property is derived from the idea of isentropic stopping of the flow, which, according to the Bernoulli's principle, is related to an increase of potential energy. In terms of enthalpy, the relationship can be written as [2, 9]

$$h_{tot} = h + \frac{c^2}{2} \quad (17)$$

where h_{tot} [J/(kg·K)] is the total (or stagnation) specific enthalpy, h [J/(kg·K)] is the static specific enthalpy and c [m/s] is the flow velocity. For ideal gases applies [2, 9]

$$h = c_p T \quad (18)$$

where c_p [J/(kg·K)] is the specific heat capacity at constant pressure. Therefore, the total temperature can be derived from Equation 17 [2, 9]

$$T_{tot} = T + \frac{c^2}{2c_p} \quad (19)$$

where T_{tot} [K] is the total (or stagnation) temperature and T [K] is the static temperature. The formula for the total pressure can be derived from Equation 19 based on the relationships of the isentropic process [2, 9]

$$\frac{p_{tot}}{p} = \left(\frac{T_{tot}}{T} \right)^{\frac{\gamma}{\gamma-1}} \quad (20)$$

where p_{tot} [Pa] is the total (or stagnation) pressure, p [Pa] is the static pressure and γ [-] is the specific heat ratio (the Poisson's constant). Finally, the total density is obtained with help of the ideal gas equation of state [2, 9]

$$\frac{\rho_{tot}}{\rho} = \left(\frac{T_{tot}}{T} \right)^{\frac{1}{\gamma-1}} \quad (21)$$

where ρ_{tot} [kg/m³] is the total (or stagnation) density and ρ [kg/m³] is the static density.

It is needed to emphasize that the above described relationships are representative of an ideal gas behaviour only. In the case of real gases, the molecular size is not negligible, which means they are not perfectly compressible. Furthermore, the latent heat of vaporization is absorbed or released during phase changes. For both these reasons, the

specific gas constant r , the specific heat ratio γ and the specific heat capacities c_p and c_v are generally functions of the pressure and the temperature with real gases. [9]

Turbochargers process two different gas mixtures. The atmospheric air is pressurized by the compressor, while turbines are propelled by the products of combustion (see Chapter 1.1). These are both gas phases, the state variables of which attain values far enough from the respective condensation points. Furthermore, the operating pressures are way below the order of magnitude, where the limited compressibility starts to be significant. Therefore, using of ideal gas models is reasonable and adopted throughout this work. Nevertheless, water vapor included in the atmospheric air may impact the actual change of enthalpy during experimental compressor characterizations (see further in Chapter 1.1.4). Humid air models can be used to account for this effect.

1.1.4 Turbocharger performance mapping

Performance mapping is a common way to assess the efficiency and the flow capacity of turbomachines. It can be done either experimentally or with help of simulation tools (e.g. CFD). The output is an indispensable resource for important engineering calculations, including the matching of a turbocharger to a combustion engine.

Hot gas stand measurement is an industry standard process, in which a complete turbocharger is mounted on the test rig (see Figure 7). An electrically driven compressor delivers fresh air to a combustion chamber, where natural gas is burnt (600°C or more). Pressurized hot fumes propel the turbine making the rotor spin up, while the load of the compressor is controlled by throttling of its outlet flow. The final speed is a result of power balance on the shaft. [2, 3, 5]

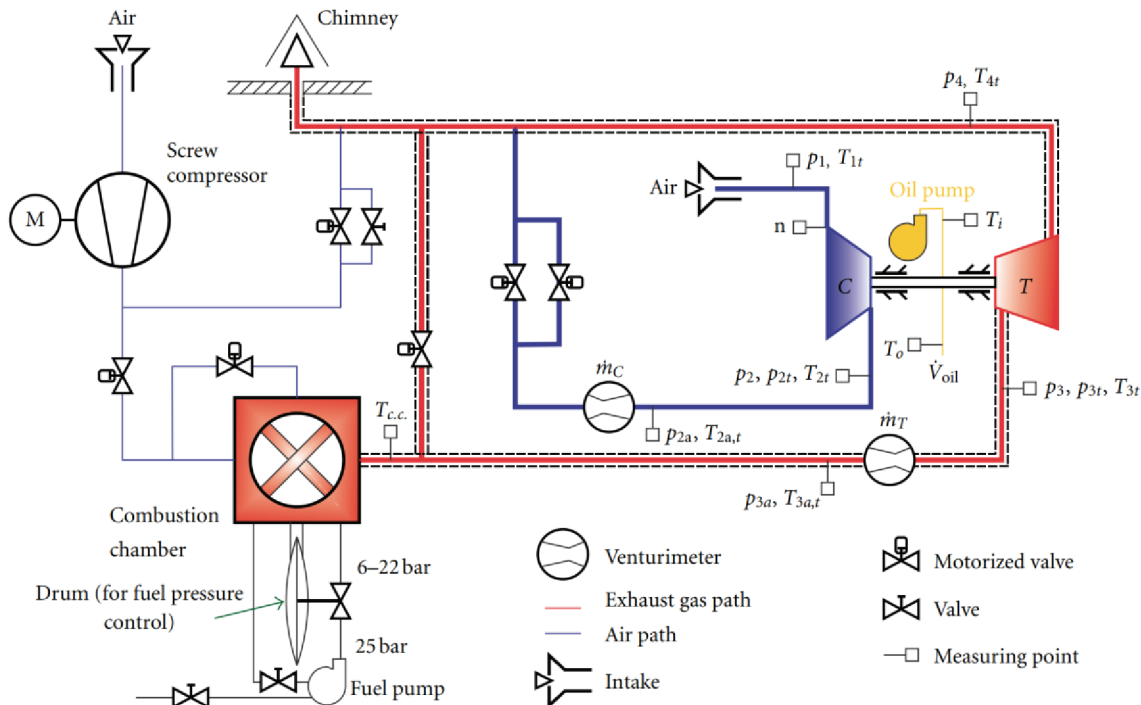


Figure 7: Hot gas stand scheme [12]

The test data is acquired at steady state conditions covering the largest feasible operating range of the attached turbocharger. Here, the primary limiting factor is the

compressor aerodynamic stability, which is constrained by the surge boundary in the low-flow region and by the choke on the opposite side. Mechanical properties of the wheel restrict the maximum spinning speed and the related maximum achievable outlet pressure. In the typical visualization of a compressor performance map, the total pressure ratio is plotted over the corrected mass flow rate (see chapter 1.1.7), however the volumetric flow rate can be assigned to the x-axis too (see Figure 8). On top of that, the isentropic efficiency is displayed as a contour or in the form of iso-lines. [2, 3, 4, 5]

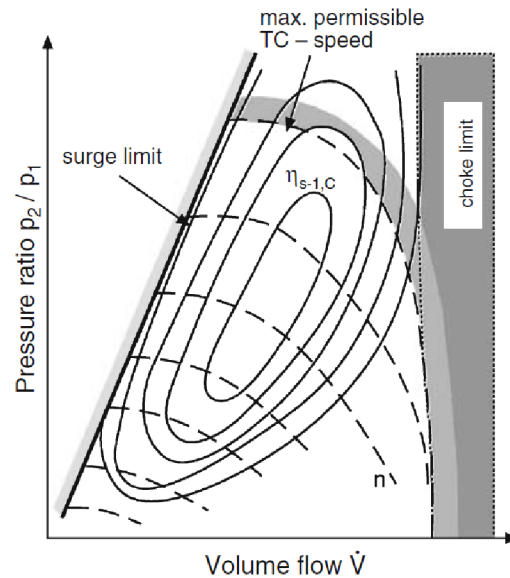


Figure 8: Compressor performance map, showing highlighted boundaries of the stable operating range, speed lines and iso-efficiency islands [5]

The danger of the surge phenomenon is related to mechanical loading of turbocharger components. A loss of aerodynamic stability in one or more blade channels results in an unsteady local reversal of flow that is followed by oscillations of both mass flow rate and pressure ratio. Not only does this impact the stability of the attached engine operation but induces vibration and increased load on the bearing system too. A hard surge (high pressure ratio and speed) can even lead to a fast system failure caused by a contact between the compressor or the turbine wheels with their housings. [2, 3, 4, 5]

In the case of a turbine, reduced mass flow rate (see Chapter 1.1.7) and efficiency are usually displayed as functions of expansion ratio in two separate diagrams (see Figure 9 and Figure 10 respectively). Nevertheless, turbine efficiency can be plotted as a contour in the mass flow rate map too (see Figure 17). It is worth noting that the mass flow rate reduces with the increasing spinning speed at a constant expansion ratio. This effect is a consequence of the centrifugal force acting on the gas. It is most pronounced with radial turbines, where the main direction of flow is centripetal (see Figure 4). However, certain impact can be identified with axial turbines too, which is driven by the contraction of streamlines near the shroud wall (the blade tip area). [2, 3, 4, 5]

An important aspect of the turbocharger mapping on a hot gas stand is the fact that turbine load is derived from a power balance with the compressor. It means that only such operating points can be measured, which allow the compressor to work steadily in

its stable operating area (see Figure 8). This typically restricts the measurable turbine performance map to narrow intervals of expansion ratio at each speed line.

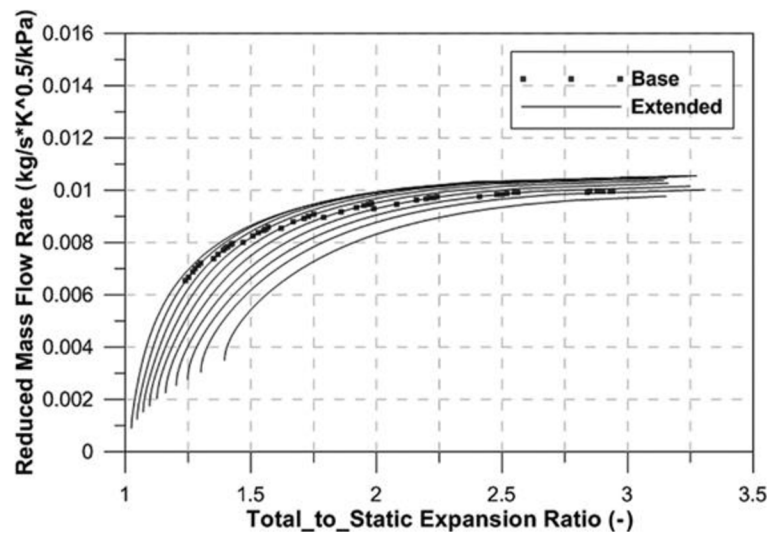


Figure 9: Turbine mass flow rate map with extrapolated speed lines obtained on a hot gas stand [15]

In Figures 9 and 10, extended speed lines are displayed to illustrate the extrapolation into the full range of expansion ratio.

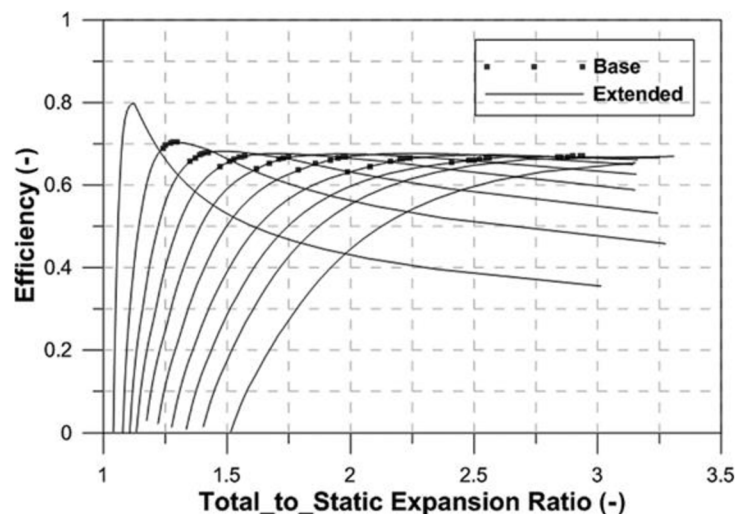


Figure 10: Turbine efficiency map with extrapolated speed lines (hot gas stand) [15]

Turbine dynamometer is often utilized as an alternative to the hot gas stand measurement for its advantage in the complete independence of the compressor. A turbine stage alone is mounted on an electric generator, which controls the load (see Figure 11). The output performance map is, however, not directly comparable to the one obtained on a hot gas stand due to the large difference in the turbine operating conditions. Firstly, the propellant gas is usually a moderately heated air ($\sim 100^\circ\text{C}$ to avoid freezing at the outlet). Furthermore, the lower temperature gradient results in a lower heat loss to the environment. On a hot gas stand, turbine efficiency is calculated based on the power balance with the compressor, the efficiency of which is determined using

the boundary pressures and temperatures (see Equation 26). The measurement of the compressor outlet temperature is, however, influenced by the heat transfer from the coolant, oil or the turbine stage. As a result, the compressor efficiency at low spinning speeds appears lower (the compressed air temperature is lower than the coolant temperature) and the calculated turbine efficiency appears higher (see [19]). Bearing friction is typically included in the so-called turbine thermo-mechanical efficiency, as it is difficult to be isolated on a hot gas stand. A dynamometer, on the contrary, enables direct shaft power measurement, so the output efficiency corresponds more closely to the actual turbine aerodynamic performance. [3]

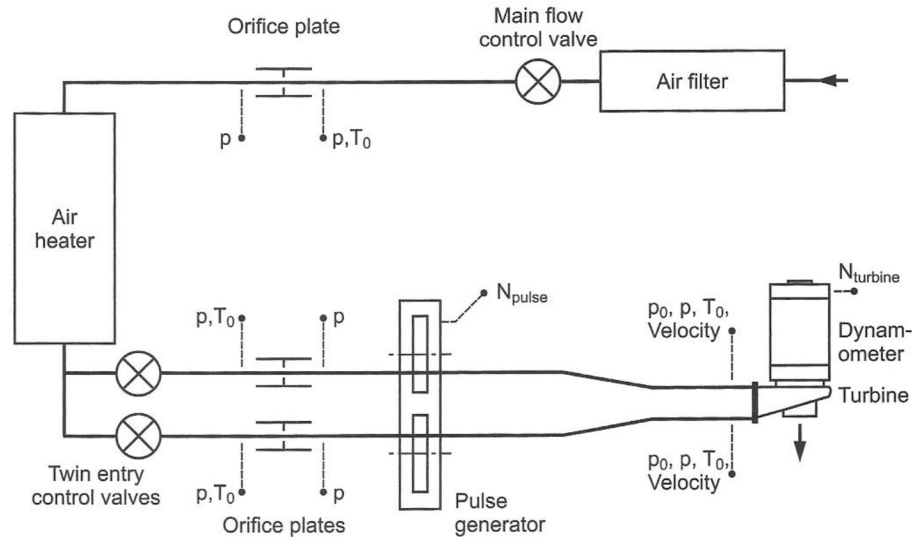


Figure 11: Turbine dynamometer with a pulse flow generator [3]

The main benefit of a turbine dynamometer measurement, nonetheless, is the possibility to capture the performance in much wider range of expansion ratio at each speed line (see Figure 12). As there is no compressor with constrained stability of operation, the true limit is the measurable range of required thermodynamic quantities (the temperature, the pressure and the mass flow rate).

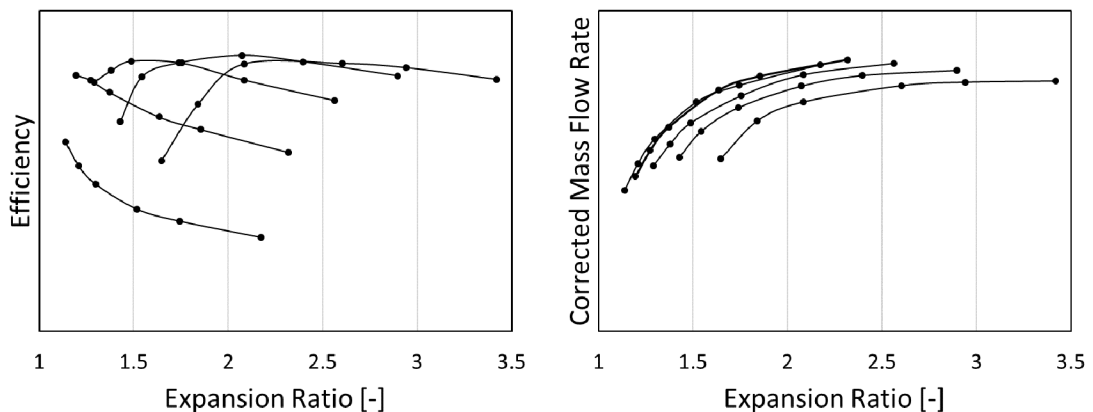


Figure 12: Turbine map obtained on a dynamometer (source: Garrett Motion Inc.)

CFD simulation is the third most common way a turbine performance map can be produced. In contrast to the first two options, numerical assessment is not limited by

the machine size, nor measurable operating conditions. On the other hand, predicted turbine performance is always only an approximation of reality and must be used with caution. Despite that, it is a convenient way to assess different designs in early stages of development mainly for the possibility to isolate the aerodynamic performance from any disturbances related to the actual machine operation. Furthermore, the detailed spatial resolution of flow conditions across the complete fluid domain makes it possible to identify local irregularities that potentially contribute to the overall efficiency loss, which would otherwise be difficult in real world conditions.

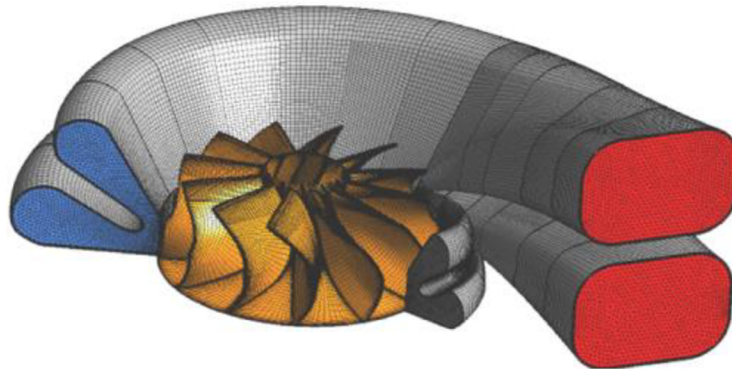


Figure 13: CFD meshes of a turbine volute and the wheel [13]

1.1.5 Compression process

The real thermodynamic process in gas compressors is compared to the isentropic compression with an associated isentropic efficiency. The outlet pressure is determined by the operating point (driven by boost demand), while the outlet total temperature includes the effect of irreversibility, which is linked to an increase of entropy. [2, 3, 4, 5]

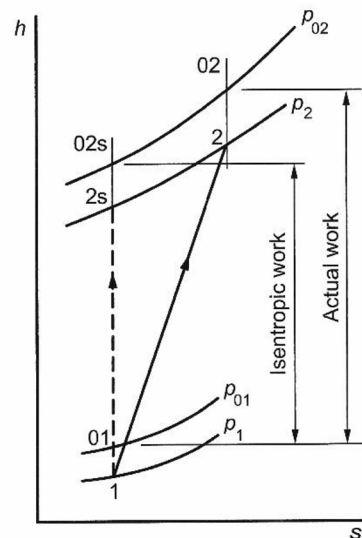


Figure 14: The ideal and real compression in the h - s diagram [3]

From the h - s diagram in Figure 14 follows that an increase of entropy for a constant outlet pressure is linked to an increase of enthalpy and the corresponding gas temperature [2, 3, 4, 5, 9]

$$\Delta h_{tot} = c_p \Delta T_{tot} \quad (22)$$

where ΔT_{tot} [K] is the change of total temperature. Therefore, a real compression is always more demanding in terms of power input than the ideal (isentropic) process. Isentropic efficiency is defined as the ratio between the ideal and the actual power inputs [2, 3, 4, 5]

$$\eta_c = \frac{P_{C_{is}}}{P_C} \quad (23)$$

where η_c [-] is the isentropic compressor efficiency, $P_{C_{is}}$ [W] is the isentropic compressor power input and P_C [W] is the real compressor power input. Since the real power input cannot be measured directly on a hot gas stand, it is calculated using the boundary conditions [2, 3, 4, 5]

$$P_C = \dot{m}_C c_{p_{air}} (T_{2C_{tot}} - T_{1C_{tot}}) \quad (24)$$

where \dot{m}_C [kg/s] is the compressor mass flow rate, $c_{p_{air}}$ [J/(kg·K)] is the specific heat capacity of air at constant pressure, $T_{2C_{tot}}$ [K] is the outlet total temperature and $T_{1C_{tot}}$ [K] is the inlet total temperature. The isentropic power input can be calculated using the same formula (see Equation 24), however, the outlet total temperature must be derived from the isentropic process [2, 3, 4, 5]

$$T_{2C_{tot_{is}}} = T_{1C_{tot}} \left(\frac{p_{2C_{tot}}}{p_{1C_{tot}}} \right)^{\frac{\gamma_{air}-1}{\gamma_{air}}} \quad (25)$$

where $T_{2C_{tot_{is}}}$ [K] is the isentropic total outlet temperature, $p_{2C_{tot}}$ [Pa] is the total outlet pressure, $p_{1C_{tot}}$ [Pa] is the total inlet pressure and γ_{air} [-] is the specific heat ratio of air. The final expression for the isentropic compressor efficiency is a ratio between the ideal and the measured changes of total temperatures [2, 3, 4, 5]

$$\eta_c = \frac{T_{1C_{tot}} \left(\left(\frac{p_{2C_{tot}}}{p_{1C_{tot}}} \right)^{\frac{\gamma_{air}-1}{\gamma_{air}}} - 1 \right)}{T_{2C_{tot}} - T_{1C_{tot}}} \quad (26)$$

The important consequence of Equation 26 is that the isentropic efficiency is fully defined by the ratio of total pressures and by the total temperatures of the entering and the exiting gas. Due to its importance, the ratio of total pressures is often referred to as the *Pressure Ratio on Compressor* (PRC) [2, 3, 4, 5]

$$PRC = \frac{p_{2C_{tot}}}{p_{1C_{tot}}} \quad (27)$$

An example of a complete compressor performance map for a common turbocharger is shown in Figure 8.

1.1.6 Expansion process

The real thermodynamic process in gas turbines is compared to the isentropic expansion with an associated isentropic efficiency. In automotive applications, the outlet pressure is usually higher than the atmospheric due to a pressure loss induced by the exhaust aftertreatment systems. The outlet total temperature, on the other hand, includes the effect of irreversibility, which is linked to an increase of entropy. [2, 3, 4, 5]

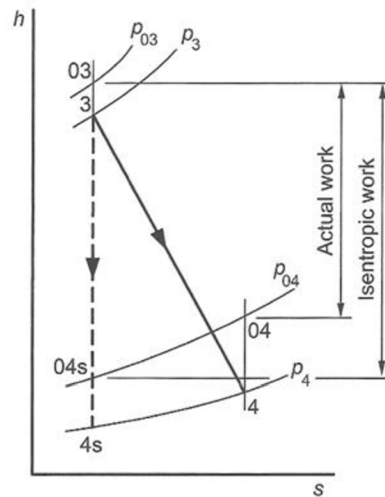


Figure 15: The ideal and real expansion in the h-s diagram [3]

From the h-s diagram in Figure 15 follows that the increase of entropy for a constant outlet pressure is linked to an increase of enthalpy and the corresponding gas temperature (see Equation 22). Therefore, a real expansion is always less useful in terms of power output than the ideal isentropic process. Isentropic efficiency is defined as the ratio between the actual and the ideal power outputs [2, 3, 4, 5]

$$\eta_T = \frac{P_T}{P_{T_{is}}} \quad (28)$$

where η_T [-] is the isentropic turbine efficiency, P_T [W] is the real turbine power output and $P_{T_{is}}$ [W] is the isentropic turbine power output. According to the convention, total-to-static turbine operating conditions (inlet-to-outlet) are usually considered with automotive turbochargers. Therefore, expansion ratio, which is also referred to as the *Pressure Ratio on Turbine* (PRT), is defined as [2, 3, 4, 5]

$$PRT = \frac{p_{1T_{tot}}}{p_{2T}} \quad (29)$$

where $p_{1T_{tot}}$ [Pa] is the total inlet pressure and p_{2T} [Pa] is the static outlet pressure. Since the real power output cannot be measured directly on a hot gas stand, it is calculated using the boundary conditions [2, 3, 4, 5]

$$P_T = \dot{m}_T c_{p_{exh}} (T_{2T} - T_{1T_{tot}}) \quad (30)$$

where \dot{m}_T [kg/s] is the turbine mass flow rate, c_{p_exh} [J/(kg·K)] is the specific heat capacity of burnt gas at constant pressure, T_{2T} [K] is the outlet static temperature and T_{1T_tot} [K] is the inlet total temperature. Isentropic power output can be calculated using the same formula (see Equation 30), however, the outlet static temperature must be derived from the isentropic process [2, 3, 4, 5]

$$T_{2T_is} = T_{1T_tot} \left(\frac{p_{2T}}{p_{1T_tot}} \right)^{\frac{\gamma_{exh}-1}{\gamma_{exh}}} \quad (31)$$

where T_{2T_is} [K] is the isentropic static outlet temperature and γ_{exh} [-] is the specific heat ratio of burnt gas. Theoretically, isentropic turbine efficiency can be determined based on the measured inlet and outlet temperatures [2, 3, 4, 5]

$$\eta_T = \frac{T_{1T_tot} - T_{2T}}{T_{1T_tot} \left(1 - \left(\frac{p_{2T}}{p_{1T_tot}} \right)^{\frac{\gamma_{exh}-1}{\gamma_{exh}}} \right)} \quad (32)$$

It is, however, difficult to measure an accurate turbine outlet temperature on a hot gas stand, because it is affected by the irregularity of temperature distribution within the exiting gas, as well as by the heat transfer to the walls of the turbine housing and the outlet piping. As a result, the measured turbine outlet temperature is usually lower than it should be, which yields an optimistic apparent turbine efficiency (even above 100%). Therefore, turbine power output is determined based on the power balance with the compressor of known performance as [2, 3, 4, 5]

$$0 = P_T - P_C - P_m - \frac{1}{2} I_{TC} \frac{d\omega_{TC}^2}{dt} \quad (33)$$

where P_m [W] is the bearing loss, I_{TC} [kg·m²] is the rotor inertia, ω_{TC} [rad/s] is the rotor angular velocity. The inertia term can be omitted in steady-state measurements, but the bearing loss power is typically unknown and remains in the equation. As per common industrial practise, mechanical losses are lumped together with the turbine power, which produces a so-called turbine thermo-mechanical efficiency [2, 3, 5]

$$\eta_{Tm} = \frac{P_C}{P_{T_is}} \quad (34)$$

Examples of turbine mass flow rate and efficiency maps for a common turbocharger are shown in Figure 9 and Figure 10 respectively.

1.1.7 Corrected and reduced parameters

Turbomachinery performance maps are measured or predicted at certain boundary conditions that can be significantly different during real-life operation. For example, a compressor may be working at high altitude, where the atmospheric pressure and temperature are comparatively lower. A turbocharger turbine, on the other hand, is supplied with pulsating burnt gas, the properties of which oscillate within a large range

(including potentially the chemical composition). To make sure the same measured map can be used to describe the performance at any operating conditions, the theory of turbomachinery similarity must be applied.

Equivalent aerodynamic conditions are achieved, when the rotor inlet velocity triangle is similar in both modes of operation. The criteria of similarity include the flow angles and the Mach number (see Figure 3). These are satisfied if the Mach numbers of both the inlet flow and the wheel circumferential speed are conserved. The flow Mach number at the rotor inlet can be expressed as [4]

$$Ma_c = \frac{c_1}{a_1} \quad (35)$$

where Ma_c [-] is the Mach number of the rotor inlet flow, c_1 [m/s] is the flow speed at the rotor inlet in the stationary reference frame and a_1 [m/s] is the speed of sound at the conditions of the rotor inlet flow. The average flow speed can be determined based on the conservation of mass criterion [2, 3, 4, 5, 9]

$$c_1 = \frac{\dot{m}}{\rho_1 A_1} = \frac{\dot{m} r T_1}{p_1 A_1} \quad (36)$$

where \dot{m} [kg/s] is the mass flow rate, ρ_1 [kg/m³] is the rotor inlet gas density, A_1 [m²] is the effective cross section area in the rotor inlet, r [J/(kg·K)] is the specific gas constant, T_1 [K] is the static gas temperature at the rotor inlet and p_1 [Pa] is the static gas pressure at the rotor inlet. The definition of the speed of sound is [2, 3, 4, 5, 9]

$$a_1 = \sqrt{\gamma r T_1} \quad (37)$$

With the above mentioned, the Mach number of the rotor inlet flow in the stationary reference frame can be rewritten as [2, 3, 4, 5]

$$Ma_c = \frac{\dot{m}}{p_1 A_1} \sqrt{\frac{r T_1}{\gamma}} \quad (38)$$

Measurement of flow conditions at the rotor inlet is, however, difficult, so it is usually done in the inducer. It can be shown that if the Mach number in the inducer is conserved, the Mach number at the rotor inlet is conserved too (under the assumption of isentropic flow). Nevertheless, the industry standard procedure uses total gas properties in the inlet, which, as per the definition, are representative of a standing flow condition. Because the corresponding Mach number would equal zero, the so-called reduced mass flow rate is used as a replacement criterion of similarity [2, 3, 4, 5]

$$\dot{m}_{red} = \frac{\dot{m}}{p_{1,tot}} \sqrt{\frac{r T_{1,tot}}{\gamma}} \quad (39)$$

where \dot{m}_{red} [(kg/s)·(K^{0.5}/Pa)] is the reduced mass flow rate, $T_{1,tot}$ [K] is the total temperature in the stage inlet and $p_{1,tot}$ [Pa] is the total pressure in the stage inlet. It

can be shown that the conservation of the reduced mass flow rate results in the conservation of the rotor inlet Mach number (under the assumption of isentropic flow). Furthermore, the final formula is independent of the flow area (see Equation 39). Nevertheless, one drawback is that the reduced mass flow rate has a different unit from the original physical mass flow rate. Therefore, it is commonly referred to the standard atmospheric conditions, so that the comparison of a measured mass flow capacity with the intended application requirement is easier. This way, the corrected mass flow rate is established [2, 3, 4, 5]

$$\dot{m}_{cor} = \dot{m} \frac{p_{ref}}{p_{1,tot}} \sqrt{\frac{T_{1,tot}}{T_{ref}} \frac{r}{r_{ref}} \frac{\gamma_{ref}}{\gamma}} \quad (40)$$

where \dot{m}_{cor} [kg/s] is the corrected mass flow rate, $p_{1,ref}$ [Pa] is the reference pressure (usually 100 kPa for the compressor and 101.325 kPa for the turbine), T_{ref} [K] is the reference temperature (usually 298 K for the compressor and 288 K for the turbine), r_{ref} [J/(kg·K)] is the reference gas constant (usually 287 J/(kg·K) for the air and 289 J/(kg·K) for the burnt gas) and γ_{ref} [-] is the reference specific heat ratio (usually 1.4 for the air and 1.35 for the burnt gas).

The other criterion of similarity, that must be conserved, is the Mach number related to the wheel circumferential speed. It is defined as [4]

$$Ma_u = \frac{u_1}{a_1} \quad (41)$$

where Ma_u [-] is the Mach number of rotor circumferential speed, u_1 [m/s] is the wheel circumferential speed at the inlet mean-flow radius. As it is more practical to measure the frequency of rotation and the temperature, the formula can be rewritten [2, 3, 4, 5]

$$Ma_u = \frac{\pi D_{m1} \frac{n_{TC}}{60}}{\sqrt{\gamma r T_1}} \quad (42)$$

where D_{m1} [m] is the mean-flow diameter at the wheel inlet and n_{TC} [1/min] is the rotor speed. In line with the principles mentioned earlier, the inlet flow temperature is usually measured in the inducer. It can be shown that the conservation of the Mach number related to the rotor circumferential velocity calculated using the speed of sound in the inducer leads to the conservation of the same at the rotor inlet conditions (assuming an isentropic flow). Like in the case of the mass flow rate, the industry standard procedure uses the total inlet temperature, while the constants are omitted (including the wheel diameter, see Equation 42). By that, the so-called reduced speed is established as a replacement criterion of turbomachinery similarity [2, 3, 4, 5]

$$n_{red} = \frac{n_{TC}}{\sqrt{\gamma r T_{1,tot}}} \quad (43)$$

where n_{red} [1/(min·K^{0.5})] is the reduced rotor speed. It can be shown that the conservation of the reduced speed results in the conservation of the Mach number of

wheel circumferential velocity (under the assumption of an isentropic flow). Reference to the standard atmospheric conditions gives the corrected rotor speed [2, 3, 4, 5]

$$n_{cor} = n_{TC} \sqrt{\frac{T_{ref} \gamma_{ref} r_{ref}}{T_{1_tot} \gamma r}} \quad (44)$$

where n_{cor} [1/min] is the corrected rotor speed. For the sake of universal applicability, the standard turbomachinery performance maps present either the reduced or the corrected mass flow rate and rotor speed (see Figures 8, 9, 10 & 12).

1.1.8 Blade speed ratio

Blade Speed Ratio (BSR) is defined as the proportion between the circumferential velocity of a turbine wheel and the isentropic spouting velocity that would be obtained by an ideal expansion of the working gas between the entry and the exit pressures of the stage. It is a non-dimensional parameter that can be interpreted as a factor of turbine load. The lower the BSR, the higher the turbine load and vice versa [2, 3, 4, 5]

$$BSR = \frac{u}{c_0} = \frac{\pi D_T \frac{n_{TC}}{60}}{\sqrt{2c_{p_exh} T_{1T_tot} \left[1 - \left(\frac{p_{2T}}{p_{1T_tot}} \right)^{\frac{\gamma_{exh}-1}{\gamma_{exh}}} \right]}} \quad (45)$$

where BSR [-] is the blade speed ratio, u [m/s] is the turbine wheel inlet circumferential velocity, c_0 [m/s] is the isentropic spouting velocity and D_T [m] is the mean-flow diameter at the wheel inlet. From the above equation follows that the turbine load depends on three operating parameters, namely the angular velocity, the expansion ratio and the inlet total temperature (usually controlled to remain constant on a hot gas stand). Radial turbines work with the highest efficiency typically at $BSR \sim 0.7$, which can be interpreted as the optimum load. It means that for the best efficiency to be reached, the angular velocity must increase together with the expansion ratio. This is well recognizable in Figure 10, which shows an extrapolated turbine efficiency map. [2, 4]

It is important to note that the same value of blade speed ratio is obtained using both the actual and corrected operating conditions (as measured or simulated). This can be proved by substituting the physical turbine speed with the corrected one and the turbine inlet temperature with its reference value in Equation 45

$$BSR_{cor} = \frac{\pi D_T \frac{NT}{60}}{\sqrt{2c_{p_exh} T_{1T_ref} \left[1 - \left(\frac{p_{2T}}{p_{1T_tot}} \right)^{\frac{\gamma_{exh}-1}{\gamma_{exh}}} \right]}} \quad (46)$$

where BSR_{cor} [-] is the blade speed ratio obtained using the corrected speed and the reference inlet total temperature. By inserting the expression for corrected speed (see Equation 44) the following formula is obtained

$$BSR_{cor} = \frac{\pi D_T \frac{n_{TC}}{60} \sqrt{T_{1T_{ref}}}}{\sqrt{2c_{p_{exh}} T_{1T_{ref}} \left[1 - \left(\frac{p_{2T}}{p_{1T_{tot}}} \right)^{\frac{\gamma_{exh}-1}{\gamma_{exh}}} \right]}}} \quad (47)$$

Further simplification leads back to Equation 45, which confirms the equality

$$BSR_{cor} = BSR \quad (48)$$

1.1.9 Engine-turbocharger interaction

Turbochargers are propelled by exhaust gases produced by the attached combustion engine (unless installed on a test stand). Piston engines, however, operate with an intermittent working cycle, which is followed by strong pulsations in the exhaust system upstream of the turbine (see Figure 16). With the opening of the exhaust valves, instantaneous pressure and temperature increase rapidly in the ports and propagate further in the form of a pressure wave. The subsequent expansion through a turbine causes the pressure in the exhaust manifold to fall again until the next event begins. The entire process repeats with a frequency corresponding to the engine speed and the number of the attached cylinders. Furthermore, the longer the period, the more time is available for the gas to exit through the turbine, which results in a higher pressure amplitude. Such a situation is typical for the turbocharging of engines with a low number of cylinders (three or less). On the contrary, a higher number of cylinders (four or more) results in steadier turbine operation during one engine working cycle. [2, 3]

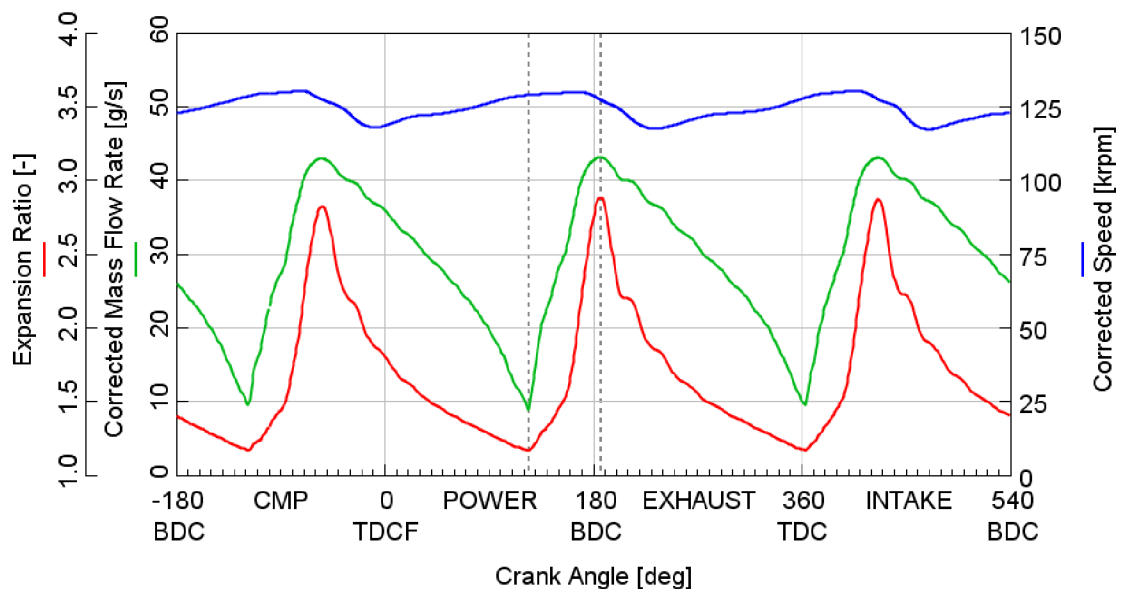


Figure 16: Expansion ratio, corrected mass flow rate and corrected turbine speed traces obtained as part of a small three-cylinder engine cycle simulation in GT-SUITE™ (TDCF – top dead centre firing, TDC – top dead centre, BDC – bottom dead centre)

While the expansion ratio follows the pulsating inlet pressure, the rotor speed changes only a little due to inertia (see Figures 16 & 17). It means that for a turbocharged engine

gas dynamics simulation to be enabled, turbine performance must be defined in a wide range of expansion ratios at each speed line. This is, however, in a large contrast to the outputs of a hot gas stand measurement (see Figures 9, 10 & 17). Therefore, a way to substantially extrapolate the measured turbine performance is needed.

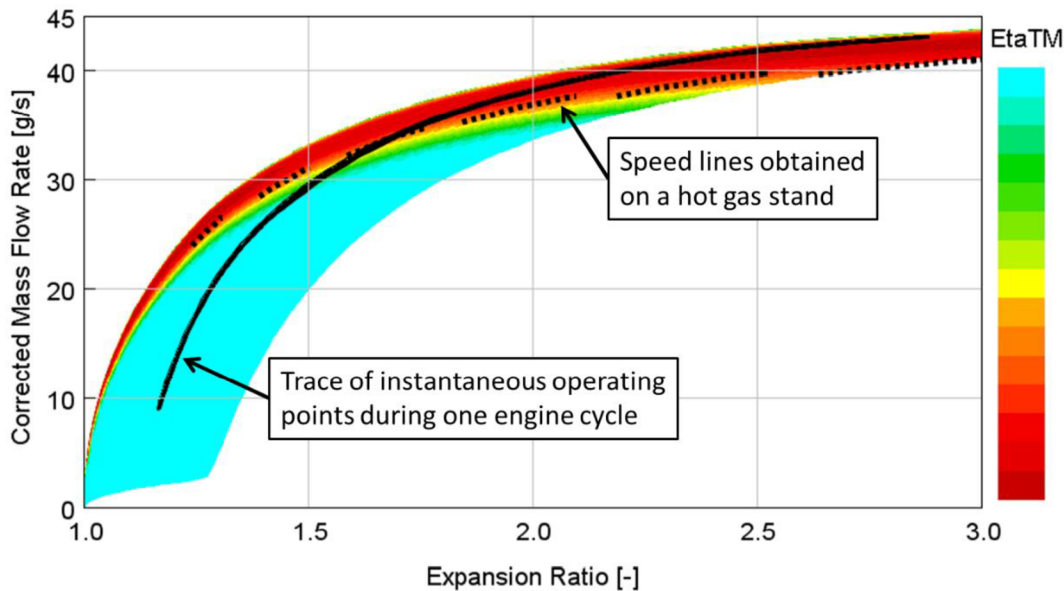


Figure 17: Turbine mass flow rate map with a trace of instantaneous operating points during one engine cycle simulated in GT-SUITE

The situation described above is typical for *pulse turbocharging*, where the system is intentionally designed to maximize the pressure amplitude (by making the exhaust manifold as compact as possible). This way, the turbine can use a certain portion of the potential energy of compressed gases remaining in the cylinders at the time of opening of the exhaust valves (see Figure 18).

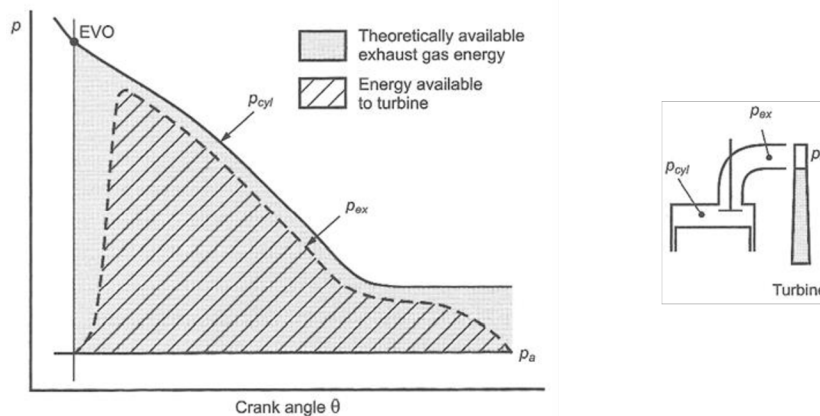


Figure 18: Pulse turbocharging [3]

Constant pressure turbocharging, on the contrary, uses exhaust manifolds of substantial volume as a buffer, so the amplitude of pressure oscillation in the turbine inlet is minimized (see Figure 19). On the one hand, the potential energy of the compressed gases remaining in the cylinders at the end of combustion is largely lost due to the expansion on the exhaust valves, but on the other hand, turbine operation is much

steadier. This is beneficial for certain engines, because the cycle-average turbine efficiency may be higher.

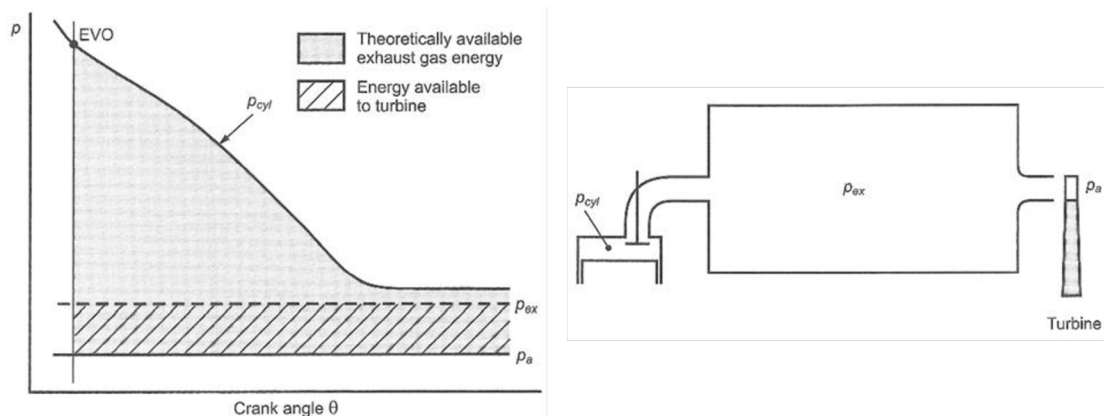


Figure 19: Constant pressure turbocharging [3]

1.1.10 State-of-the-art turbine fitting process

As mentioned in Chapter 1.1.9, extrapolated turbine performance maps are needed for engineering simulations of turbocharged combustion engine working cycles. Therefore, state-of-the-art commercial software is equipped with fitting methods designed for this purpose. To the established products in this group belong the GT-SIUTE™, the Ricardo WAVE™ or the AVL BOOST™.

As the main goal of this work is to make the selection of suitable matching candidates easier, it would be of an advantage to treat turbocharger maps in a way that is compatible with the target program solution. Not only would it enable a transparent performance prediction at extrapolated operating points but facilitate data import too.

Because the GT-SUITE is available to the author of this work, its turbine performance map fitting algorithm is taken as the baseline and described in the following text. Based on the available information sources, the properties of five characteristic functions are determined in a process consisting of seven main steps. [10, 20]

Pre-processing of turbine performance data

Input data is loaded and blade speed ratio (BSR) calculated at every operating point (see Chapter 1.1.8). Depending on the measurement/simulation procedure, operating points are grouped either by corrected speed (speed lines) or by expansion ratio (expansion ratio lines). A maximum-efficiency point is identified within each group. [10, 20]

Fitting the optimum blade speed ratio

The BSR's at operating points of maximum efficiency per group are considered the optimum ones. The fitting function is linear with respect to the expansion ratio. [10, 20]

Fitting the maximum efficiency

Operating points of maximum efficiency, which were identified in the first step of the process, are fitted with respect to corrected speed (in the case of a grouping to speed lines) or expansion ratio (a grouping to constant PRT lines). Then, normalized efficiency

is calculated at every operating point of the original map using the maximum efficiency interpolated at the same levels of expansion ratio. [10, 20]

Fitting the normalized efficiency

All turbine operating points are supposed to lie on a single curve, when plotted in a diagram of normalized efficiency versus normalized blade speed ratio. The optimum BSR needed to normalize the BSR at each operating point is determined using the first fitting function. [10, 20]

Fitting the optimum corrected mass flow rate

Corrected mass flow rate at the operating points of maximum efficiency within each speed line or constant expansion ratio line is fitted with respect to corrected speed or expansion ratio, respectively. Thereafter, a normalized mass flow rate is calculated at every operating point of the original map using the optimum mass flow rate values interpolated at the same levels of expansion ratio. [10, 20]

Fitting the normalized mass flow rate

All operating points are supposed to lie on a single curve, when plotted in a diagram of normalized mass flow rate versus normalized blade speed ratio. The optimum BSR needed to normalize the BSR at each operating point is determined using the first fitting function. [10, 20]

Saving of turbine performance model

A complete turbine performance model consists of five fitting functions describing the optimum BSR, the maximum efficiency, the normalized efficiency, the optimum corrected mass flow rate and the normalized mass flow rate. [10, 20]

1.2 Interpolation

Interpolation is the name for a group of methods that are used to estimate functional relationships described by sets of discrete points. An interpolant is a function that passes through the original data points. The evaluation of it enables the creation of new points at intermediate values of the independent variable(s). The main distinguishing feature is the type of an interpolant used. A few common methods are selected and described further in the following chapters.

1.2.1 Polynomial interpolation

Polynomials are a very popular type of interpolants, because they are easy to construct and evaluate (in terms of computational demands). Furthermore, it is easy to obtain their derivatives and integrals too. On the other hand, higher-order polynomials tend to be oscillatory, which makes them unsuitable for fitting of bigger numbers of points. A general expression for a polynomial interpolant is [7]

$$P_{n-1}(x) = \sum_{i=1}^n C_i x^{n-i} \quad (49)$$

where x [-] is the independent variable, n [-] is the number of known points (also called knots) and C_i [-] is the coefficient of an i -th polynomial term ($i = 1, 2, \dots, n$). In this case, the polynomial order is marked with $n - 1$, which corresponds to the fact that it is determined by the number of knots. For example, two points are enough to fully define a line in space, which can be described by a first-order polynomial (i.e. a linear function). A common approach to the construction of a polynomial interpolant is the Lagrange method. It can be described mathematically by a formula [7]

$$L_{n-1}(x) = \sum_{i=1}^n y_i l_i(x) \quad (50)$$

where y_i [-] is the function value at an i -th knot and l_i [-] is the so-called fundamental polynomial. The definition of a fundamental polynomial is [7]

$$l_i(x) = \frac{(x - x_1)(x - x_2) \dots (x - x_{i-1})(x - x_{i+1}) \dots (x - x_n)}{(x_i - x_1)(x_i - x_2) \dots (x_i - x_{i-1})(x_i - x_{i+1}) \dots (x_i - x_n)} \quad (51)$$

where x_i [-] is the independent coordinate of an i -th knot.

From the other methods of polynomial interpolation, the Newton's can be mentioned for its benefit in simpler addition of new knots. The Hermit's approach, on the other hand, introduces derivatives at each knot that the interpolant must accommodate to.

1.2.2 Linear spline interpolation

The idea behind splines is that the independent variable domain, which contains a finite set of knots, is divided into sub-intervals that the interpolant is defined on. This way a piecewise polynomial is created. Linear spline is the simplest example, where each pair of neighbouring knots is interpolated by a line [7]

$$S_i(x) = y_i + \frac{(y_{i+1} - y_i)}{(x_{i+1} - x_i)}(x - x_i) \quad (52)$$

where $S_i(x)$ [-] is the polynomial piece defined on an i -th interval ($i = 1, 2, \dots, n - 1$). To the features of linear splines belong a zeroth order continuity (i.e. continuity in value), but the derivatives are generally discontinuous. To cope with that, higher-order splines must be used. The order of a spline is determined by the highest order of its polynomial pieces, but the order of continuity can only be as high as the spline order minus one (or smaller) [7]

$$S(x) \in C^{k-1}\langle a, b \rangle \quad (53)$$

where k [-] is the spline order, a [-] and b [-] are the end-points of the complete interval the spline is defined on. The interpretation of Equation 53 is that a spline $S(x)$ belongs to a set of functions defined on an interval $\langle a, b \rangle$, which are continuous together with the derivatives up to the order of $k - 1$.

1.2.3 Cubic spline interpolation

The advantage of a cubic spline over the linear is that it can have continuous derivatives up to the second order.

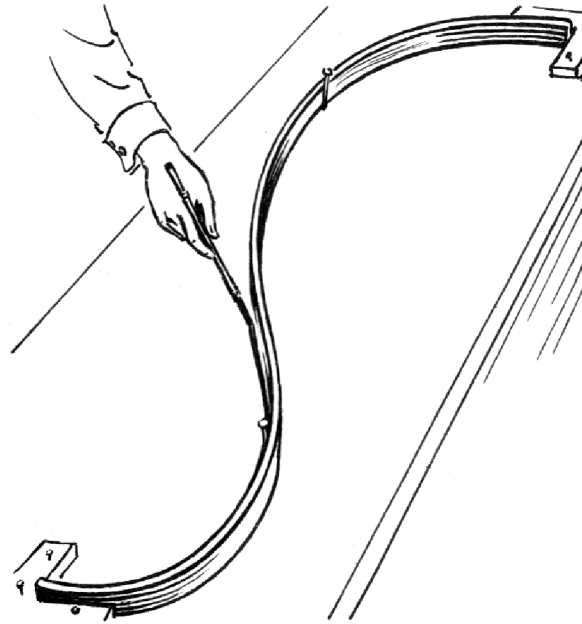


Figure 20: Drawing of a spline using an elastic ruler [22]

Particularly popular is a form, in which the continuity of the second derivative is enforced. In such a case, the shape of the spline is equivalent to that of a homogeneous elastic beam with a constant cross section, which is bent to pass through several predefined points (see Figure 20). It can be shown that this shape yields the lowest potential bending energy, which is the naturally stable state every elastic object converges to when subjected to external forces.

Generally, a cubic spline with prescribed first derivatives (also called the Hermit's cubic spline) can be formulated as [7]

$$\begin{aligned}
 S_i(x) = & y_i + (x - x_i)d_i + (x - x_i)^2 \frac{3 \frac{y_{i+1} - y_i}{x_{i+1} - x_i} - 2d_i - d_{i+1}}{(x_{i+1} - x_i)} \\
 & + (x - x_i)^3 \frac{d_i - 2 \frac{y_{i+1} - y_i}{x_{i+1} - x_i} + d_{i+1}}{(x_{i+1} - x_i)^2}
 \end{aligned} \quad (54)$$

where d_i [-] is the first derivative of a spline at the i -th knot ($i = 1, 2, \dots, n - 1$).

To make sure even the second derivative is continuous, another condition must be added [7]

$$\begin{aligned}
 (x_{i+2} - x_{i+1})d_i + 2(x_{i+2} - x_i)d_{i+1} + (x_{i+1} - x_i)d_{i+2} \\
 = 3 \left[(x_{i+2} - x_{i+1}) \frac{y_{i+1} - y_i}{x_{i+1} - x_i} + (x_{i+1} - x_i) \frac{y_{i+2} - y_{i+1}}{x_{i+2} - x_{i+1}} \right]
 \end{aligned} \quad (55)$$

where $i = 1, 2, \dots, n - 2$. With the above expression a system of $n - 2$ equations containing n unknown variables (derivatives d_i) is created. It means that two more equations are needed to obtain a unique solution. These are the end-point first derivatives, which can be interpreted as geometric constraints (see Figure 20).

In many cases, however, it is desired to construct a spline that corresponds to the shape of a bent elastic beam with rotating supports at each end. This is the situation of the so-called *natural cubic spline*, the second derivatives of which equal zero at each endpoint (i.e. there is zero curvature). The formula for the second derivative of a cubic spline can be obtained by derivation of Equation 54 [7]

$$S''_i(x) = \frac{[6(x_{i+1} - x_i) - 12(x - x_i)] \frac{y_{i+1} - y_i}{x_{i+1} - x_i}}{(x_{i+1} - x_i)^2} + \frac{[6(x - x_i) - 4(x_{i+1} - x_i)]d_i}{(x_{i+1} - x_i)^2} + \frac{[6(x - x_i) - 2(x_{i+1} - x_i)]d_{i+1}}{(x_{i+1} - x_i)^2} \quad (56)$$

By setting the second derivative to zero for indices $i = 1$ and $i = n - 1$, which correspond to the end-points x_1 and x_n respectively, an extended system of equations is obtained. It has a single unique solution (see Equations 55 and 56).

1.3 Curve Fitting

The main difference between interpolation and curve fitting is that a fitted function does not necessarily pass through the input data points. Instead, the goal is to capture the overall trend using a typically rather simple function.

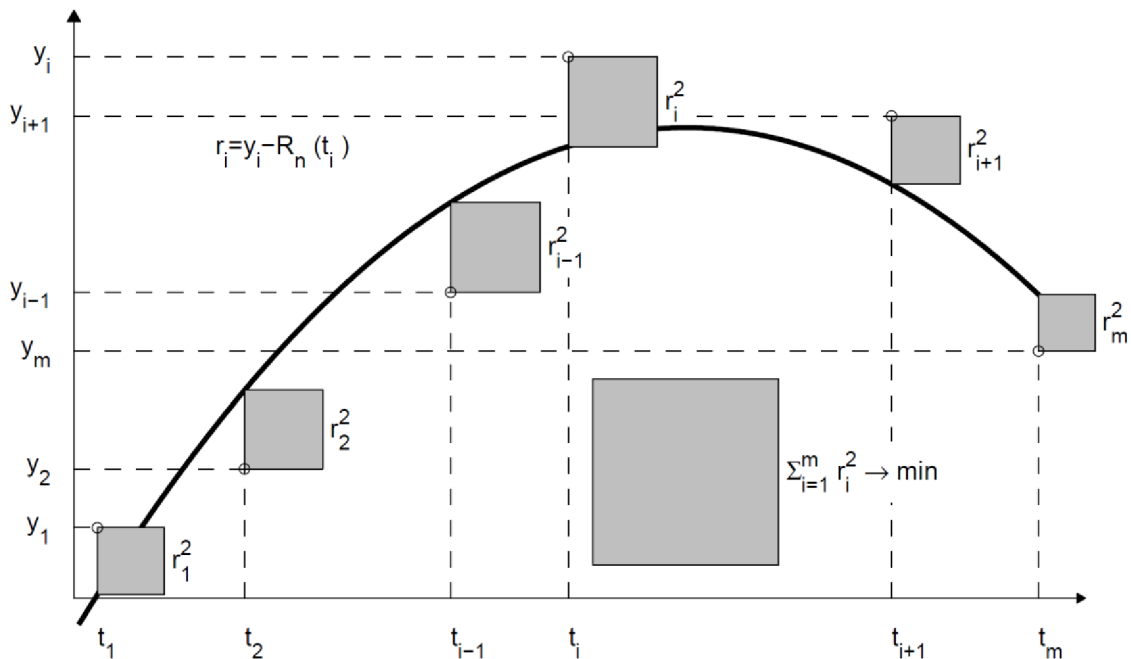


Figure 21: Illustration of the least squares method [7]

In statistics, this process is called a regression and the fitted model is supposed to approximate the mean value of the experimental data, which has been obtained with random errors. The same is true for the technical measurements, where the size of deviations is related to the accuracy of applied sensors. A common goal of regression algorithms is to find such a set of fitted function parameters that minimizes the overall quadratic error between the model and the input data. This approach is also referred to as the *least squares method* (see Figure 21).

The reason for modelling of empirical relationships is to enable an unbiased estimation of the target quantity at any point of its domain of definition, potentially including areas outside of the input data range. Depending on the model complexity, there can be one or multiple parameters to identify. Two common methods applied for this purpose are described in the following chapters.

1.3.1 Linear least squares fitting

The method of least squares is based on the principle that the sum of squared deviations of data points from the fitted function is minimized [7]

$$\sum_{i=1}^n r_{di}^2 \rightarrow \min. \quad (57)$$

where r_{di} [-] is the deviation of the i -th data point from the fitted function (a residual) and n [-] is the number of all data points. In the case of the linear least squares method, the model can be described by a linear combination of the so-called basis functions [7]

$$R(x) = \sum_{j=1}^m \beta_j \varphi_j(x) \quad (58)$$

where $R(x)$ [-] is the fitted function (also called regression function), x [-] is the independent variable, β [-] is the linear coefficient and $\varphi(x)$ [-] is the basis function. The number of basis functions (m) must be smaller than or equal to the number of data points (n). The deviation at each data point is defined as [7]

$$r_{di} = y_i - R(x_i) \quad (59)$$

where y_i [-] is the dependent coordinate of the data point x_i [-] identified by the index i [-]. For the overall squared deviation applies [7]

$$\|r_d\|^2 = \sum_{i=1}^n r_{di}^2 = \sum_{i=1}^n \left(y_i - \sum_{j=1}^m \beta_j \varphi_j(x_i) \right)^2 \quad (60)$$

where $\|r_d\|^2$ [-] is the overall squared deviation. At the minimum of the overall squared deviation, the first derivative with respect to each basis function coefficient must equal zero [7]

$$\frac{\partial \|r_d\|^2}{\partial \beta_k} = 2 \sum_{i=1}^n \left[y_i - \sum_{j=1}^m \beta_j \varphi_j(x_i) \right] [-\varphi_k(x_i)] = 0 \quad (61)$$

where k [-] is the index of a basis function coefficient ($k = 1, 2, \dots, m$). By reorganizing Equation 61 is obtained [7]

$$\sum_{j=1}^m \left[\sum_{i=1}^n \varphi_k(x_i) \varphi_j(x_i) \right] \beta_j = \sum_{i=1}^n \varphi_k(x_i) y_i \quad (62)$$

Equation 62 can be expressed in a matrix form [7]

$$\Phi^T \Phi \beta = \Phi^T \mathbf{y} \quad (63)$$

where Φ [-] is the system of basis functions, β [-] is the vector of unknown coefficients and \mathbf{y} [-] is the vector of dependent coordinates of the known data points. For completeness, the matrix Φ is defined as [7]

$$\Phi = \begin{bmatrix} \varphi_1(x_1) & \varphi_2(x_1) & \cdots & \varphi_m(x_1) \\ \varphi_1(x_2) & \varphi_2(x_2) & \cdots & \varphi_m(x_2) \\ \vdots & \vdots & \cdots & \vdots \\ \varphi_1(x_n) & \varphi_2(x_n) & \cdots & \varphi_m(x_n) \end{bmatrix} \quad (64)$$

If the columns of the matrix Φ are linearly independent, Equation 63 has a unique solution, which is such a vector β that yields the minimum overall squared deviation of known data points from the fitted function.

The most common application of the linear least squares method is the fitting of a polynomial to known data points. In such a case, the regression function has the following form (compare to Equation 58) [7]

$$R_{m-1}(x) = \sum_{j=1}^m \beta_j x^{m-j} \quad (65)$$

where the degree of the polynomial can only be as high as the number of known points minus one (i.e. $m - 1$), which corresponds to the previously mentioned condition $m \leq n$. In the case the polynomial degree is exactly by one smaller than the number of known points (i.e. $m = n$), the function passes through all the data points with zero deviation, which is equivalent to polynomial interpolation. This is, however, counterproductive, if the polynomial least squares fitting was intended to smooth out the input data (e.g. obtained by measurement). Therefore, it is important to select such a polynomial degree that is expected to model the behaviour of the measured system.

1.3.2 Least squares fitting using optimization

It was mentioned in Chapter 1.3.1 that the principle of the least squares method is to find such a set of model properties, which results in the minimum overall squared deviation from the known data points. As such, it is a minimization task that can be

addressed by an optimization algorithm. This is particularly relevant in cases, when the relationship between the fitting function and the unknown parameter(s) is non-linear (also referred to as *non-linear least squares*). A commonly occurring example is the exponential function [8]

$$R(x) = \alpha e^{\beta x} \quad (66)$$

where α [-] and β [-] are the unknown parameters. On the one hand, the expression in Equation 66 can be linearized by logarithmic transformation as

$$\ln(R(x)) = \ln(\alpha) + \beta x \quad (67)$$

On the other hand, the overall quadratic deviation in logarithmic coordinates would differ from the one in linear coordinates

$$\|r_d\|^2 = \sum_{i=1}^n [\ln(y_i) - \ln(\alpha) - \beta x_i]^2 \quad (68)$$

It can be shown that the overall quadratic deviation in Equation 68 attains its minimum for different values of α and β than the original function (without logarithmic transformation). Therefore, applying an optimization method to find the non-linear coefficients is a better solution.

There are many algorithms that can be used to find the optimum fit (see Chapter 1.4). The top-level process, which is common to most optimization methods, starts from a set of initial values of the unknown parameters. Subsequent iteration steps involve incremental changes to the unknown parameters such that the objective function (the overall squared deviation) decreases in value. Finally, the optimization process is finished after termination criteria are met (these usually include the minimum iteration step size and/or the minimum change in the objective function value).

1.3.3 Descriptive statistics

In the context of data fitting, the initial step of any statistical analysis is to determine the error between each source data point and the model. This process is described mathematically by Equation 59.

To the basic statistics belong the *maximum*, the *minimum* and the *arithmetic mean error*. The latter can be calculated using a formula [8]

$$r_{mean} = \frac{1}{n} \sum_{i=1}^n r_{di} \quad (69)$$

where r_{mean} [-] is the arithmetic mean of the error and n [-] is the number of samples in the source data set. The *arithmetic mean error* can be interpreted as a factor describing how well the fit is centred with the source data. A positive value suggests that, on average, the data is located above the fitted function and vice versa.

Another quantity with a similar meaning is the *median error*. It is the middle value of an ordered data set, where a half of the data has a bigger value and the other a smaller one. In the case the number of samples is even, the *median error* is calculated as the mean of the middle two values [8]

$$r_{median} = \frac{1}{2} \left(r_{d_ordered_floor(\frac{n+1}{2})} + r_{d_ordered_ceiling(\frac{n+1}{2})} \right) \quad (70)$$

where r_{median} [-] is the median of the error and $r_{d_ordered_i}$ [-] is the error at the i -th data point (ordered from the smallest to the largest). In contrast to the *arithmetic mean error*, the *median error* is not affected by the presence of a few points with very big error in the source data set.

In mathematical regression, the most used measure of fit quality is the *mean squared error* (MSE). It can be calculated as [8]

$$r_{MSE} = \frac{1}{n} \sum_{i=1}^n (r_{di})^2 \quad (71)$$

The advantage of the MSE over the arithmetic mean is that it yields non-negative values. In other words, the task of a fitting algorithm is to minimize it. On the other hand, errors of big magnitude are more pronounced in it compared to the arithmetic mean. Also, the unit of the MSE is different from the source data variable, which is commonly solved by calculating its square root. By that, the root-mean-square error (RMSE) is obtained [8]

$$r_{RMSE} = \sqrt{r_{MSE}} \quad (72)$$

where r_{RMSE} [-] is the root-mean-square error. The above described relationship is analogical to the one between the variance and the standard deviation.

Another convenient way to visualize the distribution of error size is the histogram. It can be described as a discrete function that counts the number of observations falling into each of several pre-defined finite intervals (see Figure 22). These intervals are called bins and they are distributed over the range of the observed variable. Mathematically is a histogram usually formulated indirectly using the summation operator [8]

$$n = \sum_{i=1}^k n_i \quad (73)$$

where k [-] is the number of bins and n_i [-] is the number of samples falling into the i -th bin. Although multiple methods can be found in the literature for the definition of bin size, they are often distributed evenly in engineering applications. Also, their number is usually determined iteratively based on the assessment of the resulting chart usefulness.

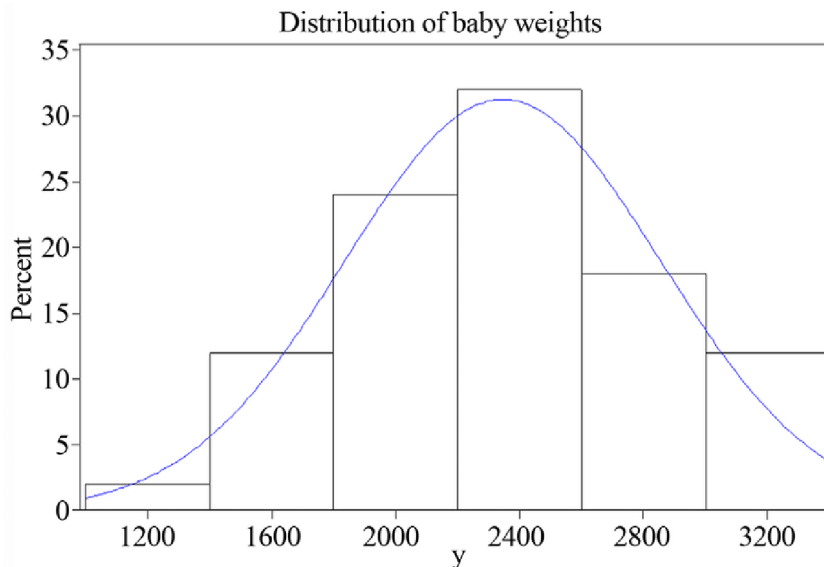


Figure 22: Histogram of child birth weight with normalized y-axis [18]

1.4 Optimization

The goal of optimization methods is to find the minimum of the so-called objective function, which is a mathematical operation on a set of independent variables. In the case of curve fitting (see Chapter 1.3.2), the objective is to calibrate the fit properties, such that the overall quadratic deviation from known data points is minimized.

Any function can have one global and multiple local minima. A global minimum is the lowest achievable value of a function. It can be isolated or represented by an n -dimensional area in the domain of definition. Local minima, on the other hand, may be of any amount, while their function value is bigger than the global minimum.

A specific example is the convex function, which only has one minimum. In the case of a strictly convex function, the minimum is isolated to a single point in the domain of definition. The opposite is a strictly concave function that has exactly one maximum. As per the definition, a convex function (generally n -dimensional) always lies below a line segment constructed between any two points of the graph (see Figure 23).

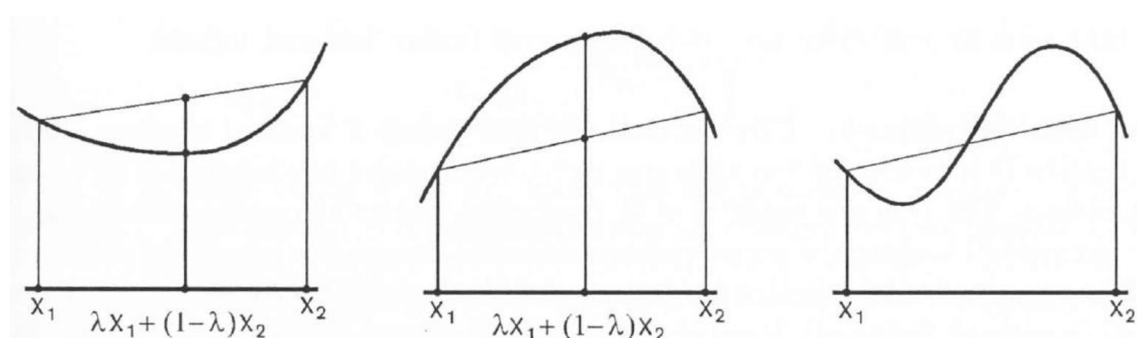


Figure 23: One-dimensional example of a convex function (left), a concave function (middle) and a general case (right) [6]

The advantage of convex functions is that the applied optimization method does not need to distinguish between global and local minima. Furthermore, it is common in

many application fields that the objective function is convex at least in certain vicinity of the optimum. Therefore, the convergence towards the true global minimum depends on the convenient selection of the starting point. That is, why in some algorithms one or more starting points are identified before the main optimization begins. One way to do that is by mapping of the objective function using a discrete grid of points covering the domain of definition. Then, local minima are located using standard optimization methods (e.g. gradient-based); the lowest is suspected of being the global minimum.

One-dimensional optimization methods are applied to one independent variable only. The solution is sought on an interval (a, b) , which is also called the uncertainty interval. The process is finished after the termination criteria are met. These usually involve the minimum iteration step and/or the minimum change in the objective function value.

The purpose of multi-dimensional optimization methods is the same, just with multiple independent variables. The extremum of the objective function is sought in an n -dimensional space ($x \in \mathbb{R}^n$). A handful of common one- and multi-dimensional methods is described in the following chapters.

1.4.1 Golden-section search

As part of the golden-section search one-dimensional objective function is evaluated at four points covering the entire initial interval of uncertainty. In each iteration step one of the boundary points is removed, so the interval is narrowed down. A new point is constructed in such a way that it is possible to reduce the new interval of uncertainty by the same factor of size in the subsequent process (see Figure 24).

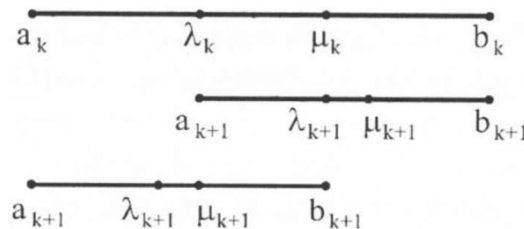


Figure 24: Possible reductions of the interval of uncertainty as part of golden-section search [6]

To make sure the factor of reduction of the uncertainty interval is constant in all iterations, the internal points must be distributed according to the golden-section ratio. It means that in a set of subintervals constructed from either of the boundary points, dividing each ordered pair of nearest size yields the golden-section ratio. The same can be described mathematically by the following system of equations [6]

$$\frac{\lambda_{dk} - a_k}{\mu_{dk} - a_k} = \frac{\mu_{dk} - a_k}{b_k - a_k} = \frac{\mu_{dk} - b_k}{\lambda_{dk} - b_k} = \frac{\lambda_{dk} - b_k}{a_k - b_k} = \alpha \quad (74)$$

where a_k [-] and b_k [-] are the boundary points, λ_{dk} [-] and μ_{dk} [-] are the internal points, k [-] is the index of the iteration step and α [-] is the golden-section ratio (see Figure 24). Assuming the initial boundaries are known, locations of the internal points can be derived from Equation 74 as

$$\lambda_{dk} = b_k + \alpha(a_k - b_k) \quad (75)$$

and

$$\mu_{dk} = a_k + \alpha(b_k - a_k) \quad (76)$$

The value of the golden-section ratio α can either be found in the literature, or obtained by adding a simple identity

$$b_k - \mu_k + \mu_k - a_k = b_k - a_k \quad (77)$$

A suitable treatment of Equations 74 and 77 produces an expression

$$\alpha^2 + \alpha - 1 = 0 \quad (78)$$

the solution of which is

$$\alpha \doteq 0.618 \quad (79)$$

Reduction of the interval of uncertainty in each iteration step is performed based on the comparison of the function values at the internal points. If the lower value is obtained at the point λ_k , it suggests that the objective function decreases in the direction towards the point a_k , so the other boundary b_k can be removed and vice versa (see Figure 24). A new internal point is determined using Equations 75 or 76. The algorithm is terminated once the size of the uncertainty interval is smaller than a predefined threshold.

For the sake of robustness, it is convenient to consider an eventuality that the initial boundaries of the uncertainty interval were selected too narrow, so it did not allow for the true optimum to be found. If the minimum objective function value is obtained at a boundary point (a_k or b_k), the algorithm needs to be capable of widening the uncertainty interval. Following the golden-section rule, the new boundary can be determined as either

$$b_{k+1} = a_k + \frac{1}{\alpha}(b_k - a_k) \quad (80)$$

or

$$a_{k+1} = b_k + \frac{1}{\alpha}(a_k - b_k) \quad (81)$$

Golden-section search is applicable on strictly quasi-convex functions only.

1.4.2 Quadratic fit method

The idea behind quadratic fit optimization is to approximate the unknown objective function by a parabola, the peak of which is the estimated location of the optimum. To construct a parabola, three distinct points of known function values are needed. The corresponding polynomial interpolation can be obtained using the Lagrange method (see Chapter 1.2.1) [6]

$$L(x) = f(x_1) \frac{(x - x_2)(x - x_3)}{(x_1 - x_2)(x_1 - x_3)} + f(x_2) \frac{(x - x_1)(x - x_3)}{(x_2 - x_1)(x_2 - x_3)} + f(x_3) \frac{(x - x_1)(x - x_2)}{(x_3 - x_1)(x_3 - x_2)} \quad (82)$$

where $L(x)$ [-] is the value of the Lagrange polynomial at point x [-]; $f(x_1)$ [-], $f(x_2)$ [-], $f(x_3)$ [-] are the three known function values at the points x_1 [-], x_2 [-] and x_3 [-].

The minimum of the interpolant is located at such an x -coordinate, where the first derivative of $L(x)$ equals zero. It can be calculated as [6]

$$L'(x) = f(x_1) \frac{2x - (x_2 + x_3)}{(x_1 - x_2)(x_1 - x_3)} + f(x_2) \frac{2x - (x_1 + x_3)}{(x_2 - x_1)(x_2 - x_3)} + f(x_3) \frac{2x - (x_1 + x_2)}{(x_3 - x_1)(x_3 - x_2)} = 0 \quad (83)$$

where $L'(x)$ [-] is the first derivative of the interpolant. The x in the above equation can be extracted as [6]

$$x = \frac{1}{2} \frac{f(x_1)(x_2^2 - x_3^2) + f(x_2)(x_3^2 - x_1^2) + f(x_3)(x_1^2 - x_2^2)}{f(x_1)(x_2 - x_3) + f(x_2)(x_3 - x_1) + f(x_3)(x_1 - x_2)} \quad (84)$$

The goal of the next optimization step is to refine the approximation of the objective function near its optimum. If the triplet of points was ordered, such that $x_1 < x_2 < x_3$, the newly obtained candidate for the optimum can fit either in the first, or in the second subinterval.

If $x_1 < x < x_2$ and $f(x_1) > f(x) < f(x_2)$, the point x_3 is omitted and the new triplet is fitted as part of the next iteration step. In the case $f(x) > f(x_2)$, the points x , x_2 and x_3 become the new triplet.

The other option is $x_2 < x < x_3$. If $f(x_2) > f(x) < f(x_3)$, the point x_1 is omitted and the new triplet is fitted as part of the next iteration step. In the case $f(x) > f(x_2)$, the points x_1 , x_2 and x become the new triplet.

Optimization is finished after the convergence criteria are met. This is typically the size of the interval of uncertainty, but another condition limiting the maximum allowable objective function difference within the triplet can be added too. The quadratic fit method is applicable on strictly quasi-convex functions only.

1.4.3 Simplex method

Simplex method, also called the Nelder-Mead method, belongs to a group of derivative-free algorithms. The direction of search is determined by the comparison of the objective function value within a group of selected points. It is designed for searching for a local minimum of a multi-dimensional objective function, so a starting point is needed ($\mathbf{x}_0 \in \mathbb{R}^n$). The main idea is that in each iteration step the objective function is evaluated in vertices of the so-called simplex, which is an n -dimensional object constructed from the starting point by adding the initial discretization distance δ to each

of its coordinates (one at a time). Therefore, it has exactly $n + 1$ vertices, which makes it a triangle in 2D, a tetrahedron in 3D etc. [7]

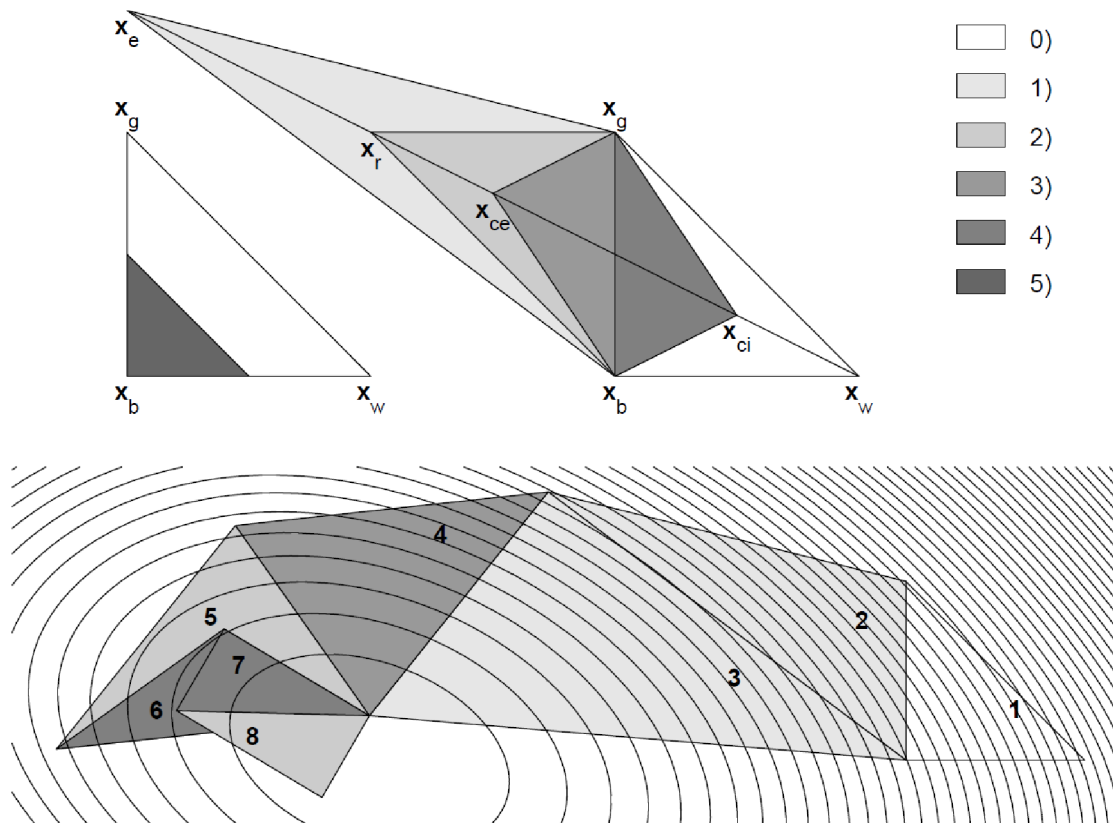


Figure 25: The simplex method (Nelder-Mead) in 2D, where 0) is the original triangle, 1) is expansion, 2) is reflection, 3) is external contraction, 4) is internal contraction, 5) stands for reduction [7]

The vertex with the highest objective function value is labelled x_w (worst) and the one with the lowest x_b (best). A new point of search \hat{x} is constructed on the line connecting the x_w with the centre of mass (\bar{x}) of all remaining points belonging to the simplex. In 2D, for example, it is the line connecting the “worst” vertex and the centre of the opposite side of the simplex triangle (see Figure 25). Then, the location of \hat{x} is determined in a few steps.

First, the objective function is evaluated at a point obtained by mirroring x_w with the centre of symmetry in point \bar{x} . This process is called reflection and it can be described mathematically as $x_r = \bar{x} + (\bar{x} - x_w)$. If $f(x_r) < f(x_b)$, it means that this is a direction of significant objective function value reduction. Therefore, one more point is constructed further away from \bar{x} . This is called expansion, which can be described mathematically as $x_e = \bar{x} + 2(\bar{x} - x_w)$. If $f(x_e) < f(x_b)$, then x_e is selected as the new vertex $\hat{x} = x_e$. Otherwise, $\hat{x} = x_r$ under the condition that $f(x_r) < f(x_g)$, where x_g (good) is any existing vertex other than x_w . [7]

In the case neither x_e nor x_r satisfy the criteria for becoming the new vertex, the new simplex is contracted in one of the following ways. If $f(x_r) < f(x_w)$, the objective function is evaluated at point $x_{ce} = \frac{1}{2}(\bar{x} + x_r)$. If $f(x_{ce}) < f(x_r)$, then $\hat{x} = x_{ce}$

(external contraction). The other possibility is that $f(\mathbf{x}_r) \geq f(\mathbf{x}_w)$ and the objective function is evaluated at $\mathbf{x}_{ci} = \frac{1}{2}(\mathbf{x}_w + \bar{\mathbf{x}})$. If $f(\mathbf{x}_{ci}) < f(\mathbf{x}_w)$, then $\hat{\mathbf{x}} = \mathbf{x}_{ci}$ (internal contraction).

In the event none of the preceding candidates for the new vertex were successful, it suggests that point \mathbf{x}_b is reasonably close to the optimum. Therefore, the simplex is reduced in such a way that point \mathbf{x}_b remains in its location, while all other vertices are moved closer to it by a half of the original distance. That is $\mathbf{x}_i = \frac{1}{2}(\mathbf{x}_b + \mathbf{x}_i)$, where i is the index spanning all vertices. All the five possible transformations of the simplex are summarized in Table 1. [7]

Table 1: Modes of transformation of the simplex [7]

	Mode	Conditions	New vertex
1	Expansion	$[f(\mathbf{x}_r) < f(\mathbf{x}_b)] \ \& \ [f(\mathbf{x}_e) < f(\mathbf{x}_b)]$	$\mathbf{x}_e = \bar{\mathbf{x}} + 2(\bar{\mathbf{x}} - \mathbf{x}_w)$
2	Reflection	$[f(\mathbf{x}_r) < f(\mathbf{x}_g)] \ \& \ (\mathbf{x}_g \neq \mathbf{x}_w)$	$\mathbf{x}_r = \bar{\mathbf{x}} + (\bar{\mathbf{x}} - \mathbf{x}_w)$
3	External contraction	$[f(\mathbf{x}_r) < f(\mathbf{x}_w)] \ \& \ [f(\mathbf{x}_{ce}) < f(\mathbf{x}_r)]$	$\mathbf{x}_{ce} = \frac{1}{2}(\bar{\mathbf{x}} + \mathbf{x}_r)$
4	Internal contraction	$[f(\mathbf{x}_r) \geq f(\mathbf{x}_w)] \ \& \ [f(\mathbf{x}_{ci}) < f(\mathbf{x}_w)]$	$\mathbf{x}_{ci} = \frac{1}{2}(\bar{\mathbf{x}} + \mathbf{x}_w)$
5	Reduction	None of the preceding conditions is met	$\mathbf{x}_i = \frac{1}{2}(\mathbf{x}_b + \mathbf{x}_i)$ $\mathbf{x}_i \neq \mathbf{x}_b$

1.4.4 Gradient descent method

The gradient descent method is suitable for the optimization of strictly convex multi-dimensional functions. The initial step is to calculate the gradient of the objective function at the starting point. Then, a new point is determined by searching for the minimum in the direction of the steepest descent (one-dimensional optimization). The process repeats until the termination criteria are met. The gradient of a function is the vector of its first partial derivatives defined as [7]

$$\nabla f(\mathbf{x}) = \left(\frac{\partial f(\mathbf{x})}{\partial x_1}, \frac{\partial f(\mathbf{x})}{\partial x_2}, \dots, \frac{\partial f(\mathbf{x})}{\partial x_n} \right) \quad (85)$$

where $f(\mathbf{x})$ [-] is the function of \mathbf{x} , \mathbf{x} [-] is the vector of coordinates in an n -dimensional space (the domain) and x_i [-] is the i -th component of the vector \mathbf{x} ($i = 1, 2, \dots, n$).

If the objective function cannot be expressed explicitly, each partial derivative in Equation 85 must be computed numerically using finite differences. The most common ones are the forward, the central and the backward. Using the forward difference, the partial derivative in an n -dimensional space can be approximated as [7]

$$\frac{\partial f(\mathbf{x})}{\partial x_i} \approx \frac{f(\mathbf{x} + h_d \mathbf{u}_i) - f(\mathbf{x})}{h_d} \quad (86)$$

where h_d [-] is the size of the discrete step and \mathbf{u}_i [-] is the standard unit vector in the direction of the i -th cartesian coordinate. The formula using the backward difference is obtained analogically as [7]

$$\frac{\partial f(\mathbf{x})}{\partial x_i} \approx \frac{f(\mathbf{x}) - f(\mathbf{x} - h_d \mathbf{u}_i)}{h_d} \quad (87)$$

Finally, the derivative approximated by the central difference is [7]

$$\frac{\partial f(\mathbf{x})}{\partial x_i} \approx \frac{f\left(\mathbf{x} + \frac{h_d}{2} \mathbf{u}_i\right) - f\left(\mathbf{x} - \frac{h_d}{2} \mathbf{u}_i\right)}{h_d} \quad (88)$$

Each evaluation of the objective function is linked to certain processing time. Therefore, it is desirable to keep their number at the minimum. Calculation of the gradient using the forward and the backward difference requires $n + 1$ evaluations in an n -dimensional space. The central difference method, on the other hand, involves $2n$ evaluations, so it is less convenient (see Figure 26).

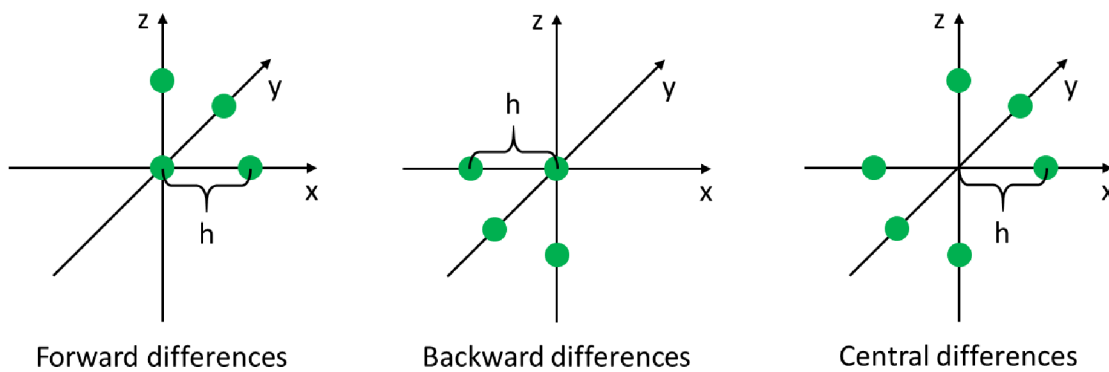


Figure 26: Visualization of the finite differences in 3-dimensional space

For completeness, the ratio of the computational effort linked to the forward/backward and the central difference depends on the number of dimensions in the following way

$$\kappa = \frac{n + 1}{2n} = \frac{1}{2} + \frac{1}{2n} \quad (89)$$

where κ [-] is the ratio of the numbers of evaluations between the forward/backward and the central difference methods. It can be noted that all methods are equally demanding in a one-dimensional space.

The next step involves minimization of the objective function in the direction of the gradient. The new coordinates of \mathbf{x} are obtained as [6]

$$\mathbf{x}_{k+1} = \mathbf{x}_k - \lambda_d \frac{\nabla f(\mathbf{x})}{\|\nabla f(\mathbf{x})\|} \quad (90)$$

where λ_d [-] is the distance in the direction of negative gradient (to be optimized) and k [-] is the index of the iteration step. A range of methods can be employed to find the

value of the parameter λ_d . The quadratic fit can be recommended for its fast convergence, especially when the objective function has near parabolic shape in certain vicinity of the optimum (see Chapter 1.4.2). The whole process is repeated until the required resolution is achieved (usually defined as the maximum size of the gradient).

To the drawbacks of the gradient descent method belongs its tendency to zigzagging, which significantly impacts the required number of iterations and the overall speed of convergence (see Figure 27). It occurs in cases, when the objective function has the shape of a long narrow valley. Since the gradient contains the information about the slope in an isolated point only, the algorithm cannot react to its change along the way to the local minimum. Among the methods addressing this issue, the Newton's can be named (see Chapter 1.4.5).

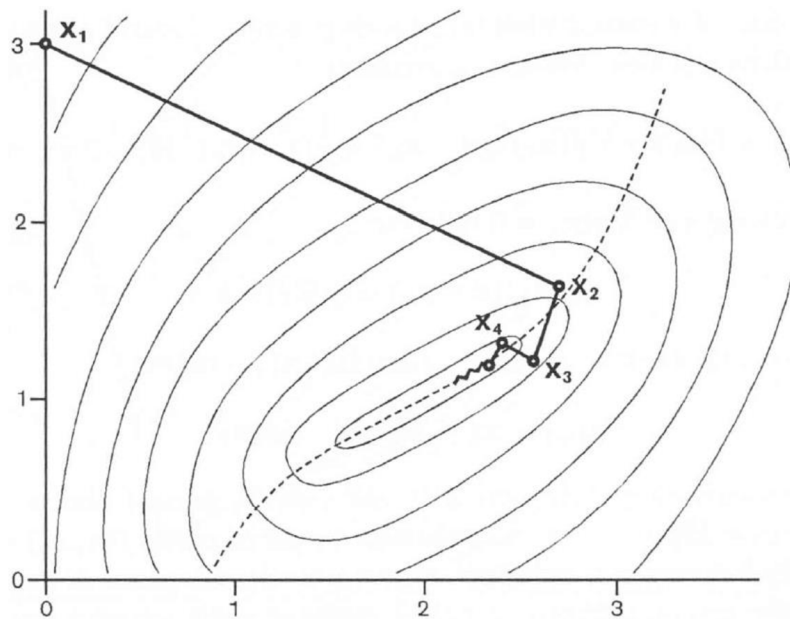


Figure 27: Zigzagging of the gradient descent method [6]

1.4.5 Newton's multi-dimensional method

The Newton's method is suitable for the optimization of strictly convex multi-dimensional functions. In contrast to the gradient descent, the Newton's algorithm uses the quadratic approximation (the first two members of the Taylor series) of the objective function to determine the next iteration point [6]

$$q(\mathbf{x}) = f(\mathbf{x}_k) + \nabla f(\mathbf{x}_k)^T (\mathbf{x} - \mathbf{x}_k) + \frac{1}{2} (\mathbf{x} - \mathbf{x}_k)^T \mathbf{H}(\mathbf{x}_k) (\mathbf{x} - \mathbf{x}_k) \quad (91)$$

where $q(\mathbf{x})$ [-] is the quadratic local approximation of the objective function, $\mathbf{H}(\mathbf{x}_k)$ [-] is the Hessian of the objective function at coordinates defined by the vector \mathbf{x}_k . At the optimum, the gradient of the quadratic function must equal zero ($\nabla q(\mathbf{x}) = 0$; see Equation 91). Therefore, the following condition must be fulfilled [6]

$$\mathbf{H}(\mathbf{x}_k) (\mathbf{x} - \mathbf{x}_k) = -\nabla f(\mathbf{x}_k) \quad (92)$$

In the next iteration step, the new coordinate of \mathbf{x} can be derived from Equation 92 as

$$\mathbf{x}_{k+1} = \mathbf{x}_k - \mathbf{H}(\mathbf{x}_k)^{-1} \nabla f(\mathbf{x}_k) \quad (93)$$

The Newton's algorithm terminates as soon as the size of the Hessian is smaller than a pre-defined threshold. While the process to determine the gradient has been explained in the previous chapter (see Equation 85), the Hessian of $f(\mathbf{x})$ is defined below [6]

$$H(\mathbf{x}) = \begin{bmatrix} \frac{\partial^2 f(\mathbf{x})}{\partial x_1^2} & \frac{\partial^2 f(\mathbf{x})}{\partial x_1 \partial x_2} & \dots & \frac{\partial^2 f(\mathbf{x})}{\partial x_1 \partial x_n} \\ \frac{\partial^2 f(\mathbf{x})}{\partial x_2 \partial x_1} & \frac{\partial^2 f(\mathbf{x})}{\partial x_2^2} & \dots & \frac{\partial^2 f(\mathbf{x})}{\partial x_2 \partial x_n} \\ \vdots & \vdots & \ddots & \vdots \\ \frac{\partial^2 f(\mathbf{x})}{\partial x_n \partial x_1} & \frac{\partial^2 f(\mathbf{x})}{\partial x_n \partial x_2} & \dots & \frac{\partial^2 f(\mathbf{x})}{\partial x_n^2} \end{bmatrix} \quad (94)$$

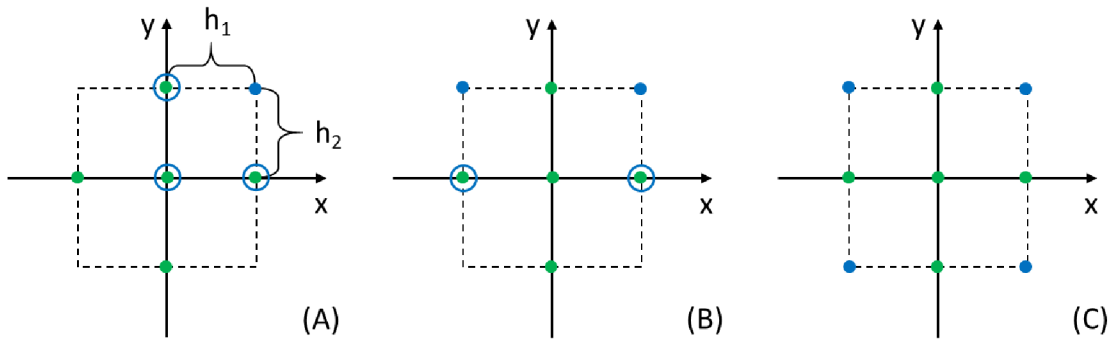
The Hessian is a matrix of the second-order partial derivatives. Unidirectional derivatives are present on the main diagonal, mixed derivatives can be found in the remaining positions. In the case the evaluation must be done numerically, finite differences can be employed (see Chapter 1.4.4 for the definition of the first partial derivatives). To calculate a second-order derivative with respect to one variable numerically, a three-point discretization of the function is needed. The formula using the central difference can be recommended for its concentricity with respect to \mathbf{x} . It can be expressed as [7]

$$\frac{\partial^2 f(\mathbf{x})}{\partial x_i^2} \approx \frac{f(\mathbf{x} + h_d \mathbf{u}_i) - 2f(\mathbf{x}) + f(\mathbf{x} - h_d \mathbf{u}_i)}{h_d^2} \quad (95)$$

The mixed second-order derivative can be interpreted as two subsequent derivations with respect to two different variables. Therefore, four points with known function values are needed to calculate it numerically. The forward, the backward and the central difference are applicable again. However, to keep the necessary number of the objective function evaluations at the minimum, the central difference method should be avoided. The formula for the mixed second-order derivative using the forward difference can be obtained by repeating the process described in Equation 86 twice in a row. The resulting equation is

$$\begin{aligned} & \frac{\partial^2 f(\mathbf{x})}{\partial x_i \partial x_j} \\ & \approx \frac{f(\mathbf{x} + h_{di} \mathbf{u}_i + h_{dj} \mathbf{u}_j) - f(\mathbf{x} + h_{dj} \mathbf{u}_j) - f(\mathbf{x} + h_{di} \mathbf{u}_i) + f(\mathbf{x})}{h_{di} h_{dj}} \end{aligned} \quad (96)$$

where i [-] and j [-] are the indices of the space dimensions, while $i \neq j$.



● Second-order derivative ● Second-order mixed derivative

Figure 28: Discretization of the Hessian in 2D, A) is the forward difference in both directions of the x- and y-axes, B) is the central difference in the direction of the x-axis and the forward difference in the direction of the y-axis, C) is the central difference in both directions of the x- and y-axes)

To calculate the Hessian per the modification (A), $2n + 1 + \binom{n}{2}$ evaluations of the objective function are needed. If the central differences were used to calculate the mixed derivatives, $2n + 1 + 2 \binom{n}{2}$ evaluations would be needed for the modification (B) and $2n + 1 + 4 \binom{n}{2}$ for the modification (C) (see Figure 28).

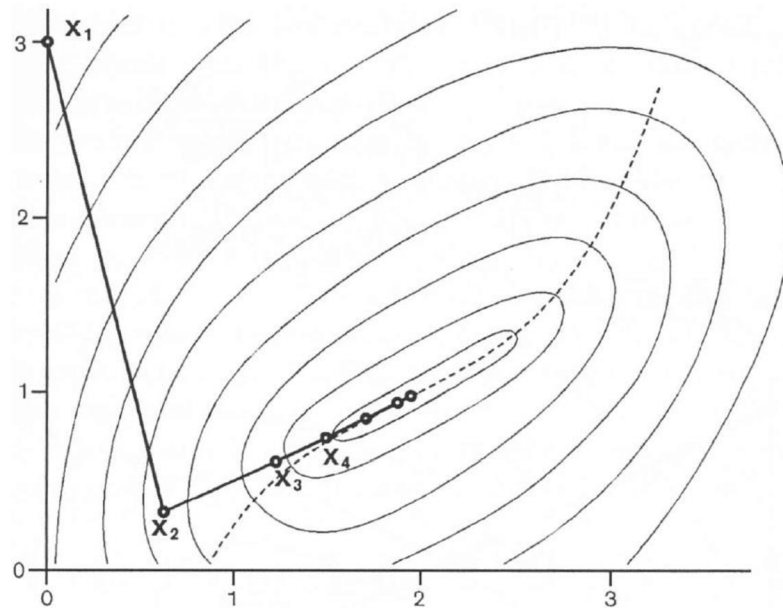


Figure 29: Illustration of the Newton's method [6]

2 BASIC TURBINE FITTING METHOD

The top-level process of the turbine performance map fitting has been described in Chapter 1.1.10. To verify it can be applied to solve real-life engineering tasks, its implementation and testing in an interactive computational environment is needed. MATLAB™ has been selected for this purpose, because it provides the required functionality and it is available to the author of this work. In the first place, a satisfactory agreement between the fitted turbine performance model and the raw data must be confirmed. Also, the algorithm should be robust with respect to varying input data source and quality. After the fully extrapolated performance maps are generated, they will have to be validated in terms of expected thermodynamic behaviour at borderline operating conditions.

2.1 Fitting the Performance Model

The turbine performance model, as described in the literature (see [10, 20]) and in Chapter 1.1.10, consists of five characteristic functions for the key thermodynamic properties of the turbomachine. These are the optimum blade speed ratio, the maximum efficiency, the optimum corrected mass flow rate, the normalized efficiency and the normalized mass flow rate. The process to determine the properties of each function to best fit the source data is described in the following chapters. A sample hot gas stand map produced at the Garrett Motion Inc. is used for this purpose. It must be noted, however, that some aspects of the baseline algorithm are not explicitly described in the available information sources. Therefore, custom solutions are suggested, which proved to be working as part of the demonstrator MATLAB application.

2.1.1 Pre-processing of input data

A typical turbine map has the form of a text file with the operating points organized into rows of data, where each column represents one characteristic variable. These include the corrected or reduced speed, the expansion ratio, the corrected or the reduced mass flow rate and the efficiency. Each operating point describes the turbine stage behaviour at steady state conditions. The environments, in which the data is obtained, can be very different though (see Chapter 1.1.4).

After the map file is loaded, the first step is to calculate the blade speed ratio at every operating point (see Chapter 1.1.8), so it can be used later in the fitting process. Depending on the procedure that was followed to generate the data, operating points might be grouped by either the corrected (or reduced) speed or the expansion ratio. Each is expected to be non-decreasing with the row number, while the other must be non-decreasing within a group.

In the most common case, the turbine map is generated using a hot gas stand rig and the testing procedure is programmed to keep the corrected (or reduced) speed constant within each group of operating points. Thus, speed lines can be recognized in the data.

The implemented fitting algorithm is programmed to read one row of the input map file after another. As soon as the corrected speed increases by a bigger value than the predefined threshold, a new speed line is marked. Once the end of the file has been reached, the operating point with the highest efficiency is identified at each speed line

and its index is saved for a later use. A similar approach would be followed, if the map data was organized into groups of a constant expansion ratio.

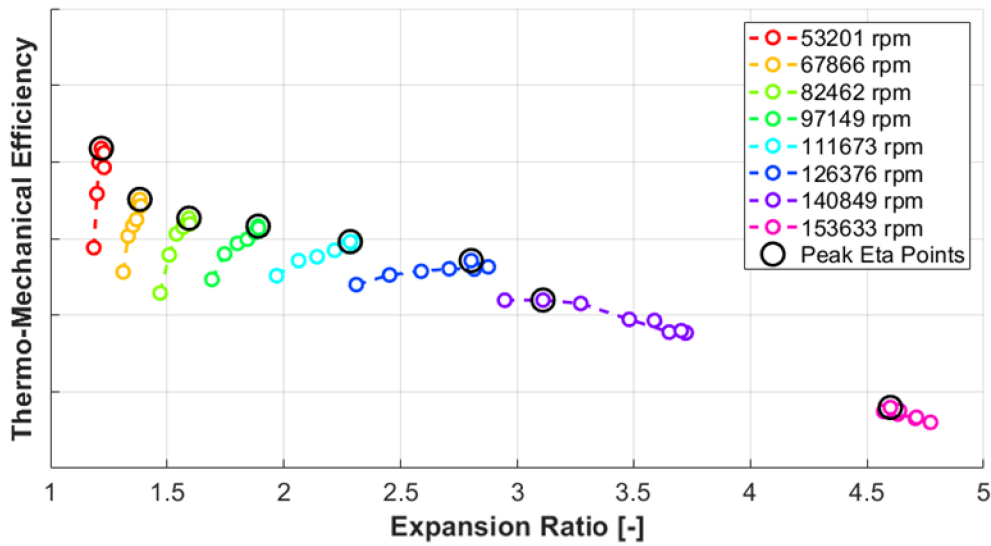


Figure 30: Efficiency vs. PRT with coloured speed lines and highlighted maxima

2.1.2 Fitting the optimum blade speed ratio

The relationship between the optimum blade speed ratio (BSR_{opt}) and the expansion ratio (PRT) is key to the fitting process (see Chapter 1.1.10). A BSR_{opt} is such a value of BSR , at which the maximum turbine efficiency is reached at certain level of PRT (i.e. it corresponds to the points of maximum efficiency identified in Chapter 2.1.1).

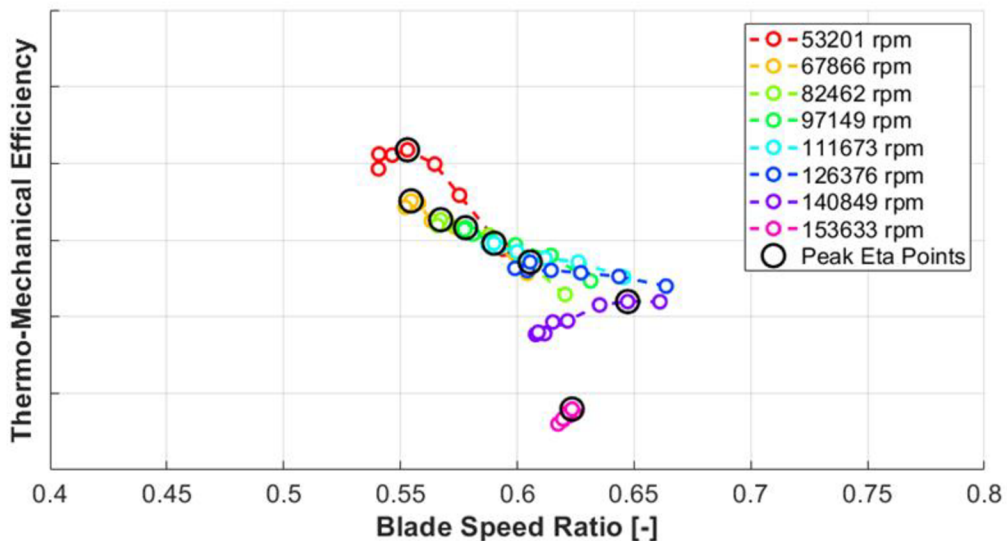


Figure 31: Efficiency vs. BSR with coloured speed lines and highlighted maxima

It is apparent that a different value of BSR_{opt} is obtained at each speed line in Figure 31. According to the literature, the relationship between BSR_{opt} and PRT should be linear [10, 20]

$$BSR_{opt} = kPRT + q \tag{97}$$

where BSR_{opt} [-] is the optimum blade speed ratio, k [-] is the slope and q [-] the elevation of the fitted line. Constants k and q are determined using the least squares method (see Chapter 1.2.1).

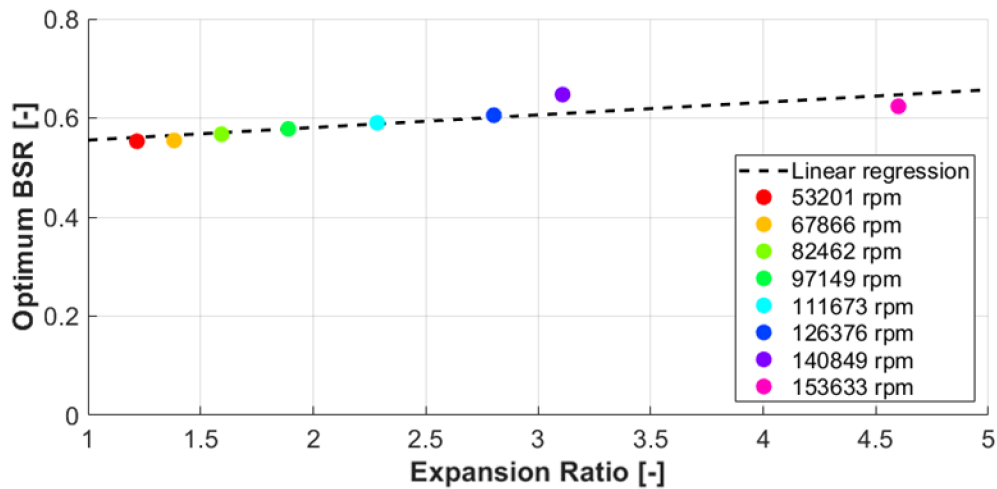


Figure 32: Linear regression of the optimum BSR relative to PRT

As soon as the fitting function for BSR_{opt} is known, the normalized blade speed ratio (BSR_{norm}) can be calculated at each operating point of the turbine map. BSR_{norm} is defined as the ratio between the BSR at given operating point and the optimum BSR at the same level of PRT [10, 20]

$$BSR_{norm} = \frac{BSR}{BSR_{opt}} \quad (98)$$

2.1.3 Fitting the maximum efficiency

The maximum efficiency points identified at each speed line during the pre-processing of the turbine map (see chapter 2.1.1) together form an envelope that all turbine operating points must lie below. This relationship is modelled with respect to the corrected speed, yet the available information sources do not suggest a specific function (except that it should be smooth; see [10, 20]). A polynomial can be named as one of the simplest options. However, with an increasing degree, the polynomial approximation (in the least squares sense) tends to be oscillatory. A spline curve, on the other hand, can be recommended for its stability and an easy definition of extrapolation modes (due to its piece-wise polynomial form). As a conservative strategy, a flat extrapolation can be applied, which is the default option in GT-SUITE too (see Figure 33).

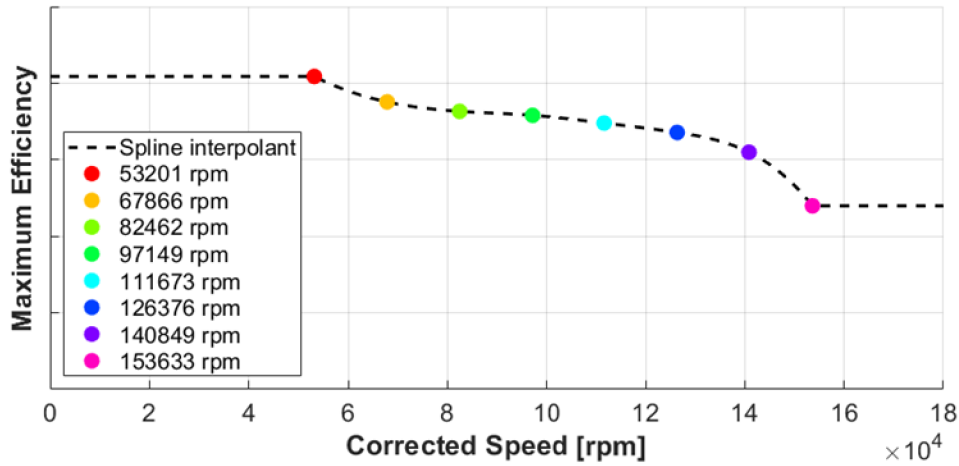


Figure 33: Maximum turbine efficiency as a cubic spline with flat extrapolation

With the fitting function for the peak efficiency available, the normalized efficiency can be calculated at each operating point of the map. Normalized efficiency ($ETATM_{norm}$) is defined as the ratio between the efficiency at the given operating point ($ETATM$) and the maximum efficiency at the same level of expansion ratio ($ETATM_{max}$) [10, 20]

$$ETATM_{norm} = \frac{ETATM}{ETATM_{max}} \quad (99)$$

The maximum efficiency function is, however, defined relative to corrected speed, so the optimum corrected speed at given expansion ratio must be found for each turbine operating point first. To do that, the optimum BSR function (see Equation 97) can be combined with the definition of BSR (see Equation 46). To make sure the corrected speed is obtained, reference gas properties must be used (see Chapter 1.1.8)

$$NT_{opt} = (kPRT + q) \sqrt{\frac{2c_{p_exh} T_{1T_ref} \left[1 - \left(\frac{1}{PRT} \right)^{\frac{\gamma_{exh}-1}{\gamma_{exh}}} \right]}{\frac{\pi D_T}{60}}} \quad (100)$$

2.1.4 Fitting the normalized efficiency

According to the available information sources all turbine operating points should lie on a single curve when plotted in the normalized efficiency versus normalized blade speed ratio diagram. In GT-SUITE, the fitting function has two parts. For $BSR_{norm} < 1$, exponentiation is defined in the form [10, 20]

$$ETATM_{norm} = 1 - (1 - BSR_{norm})^{b_{fit}} \quad (101)$$

where the exponent b_{fit} [-] is the fitted parameter. It needs to be noted that the linear least-squares approach (as explained in Chapter 1.2.1) cannot be used to find the value of b_{fit} , because its relationship to the root-mean-square error is non-linear. The quadratic fit optimization method can be recommended instead.

The other part of the normalized efficiency curve, where $BSR_{norm} \geq 1$, is fitted by a parabola of the form [10, 20]

$$ETATM_{norm} = 1 - c_{fit}(BSR_{norm} - 1)^2 \quad (102)$$

where the coefficient c_{fit} [-] is related to the intercept with the x -axis and can be found using the least-squares method. The value of BSR_{norm} , at which the x -axis is crossed, can be determined using the equation

$$BSR_{norm_ETA_int} = \frac{1}{c_{fit}^2} + 1 \quad (103)$$

The complete curve of normalized efficiency versus normalized blade speed ratio passes through the point with coordinates [1,1]. It can be interpreted as the generalized optimum operating point that the turbine works with the highest efficiency at.

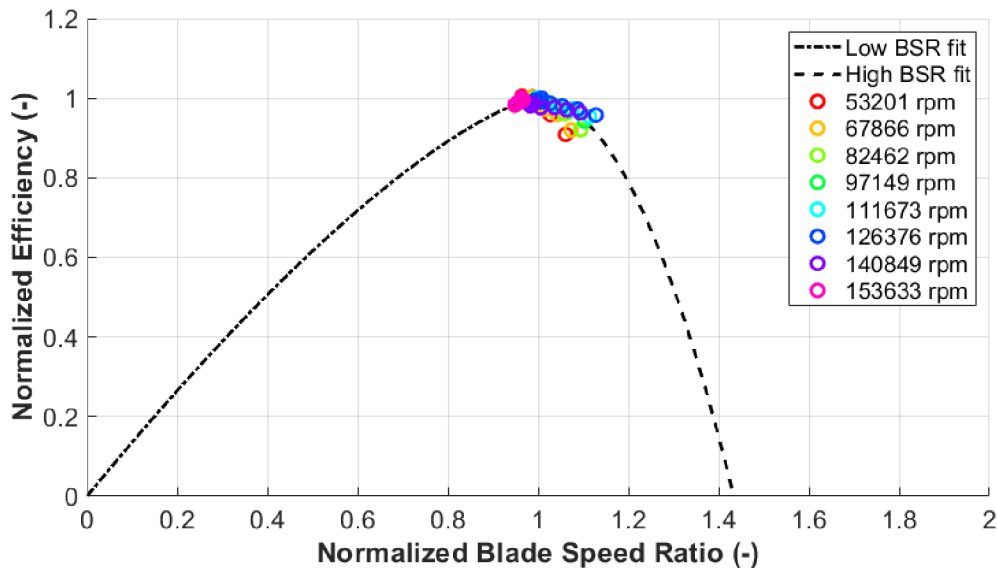


Figure 34: Normalized efficiency fitted with respect to normalized blade speed ratio

2.1.5 Fitting the optimum corrected mass flow rate

An optimum corrected mass flow rate is associated with each operating point of the maximum efficiency at each speed line or constant expansion ratio line (see Chapter 2.1.1). Similarly to the case of the maximum efficiency (see Chapter 2.1.3), these points are fitted with respect to the corrected speed, but the available information sources only suggest the function should be smooth and pass through the origin of the coordinate system (see [10, 20]). Therefore, a spline curve is recommended again. Extrapolation is needed in the direction of high corrected speeds only. In line with the conservative approach applied before ($ETATM_{max}$), the flat extrapolation is used (by default in GT-SUITE).

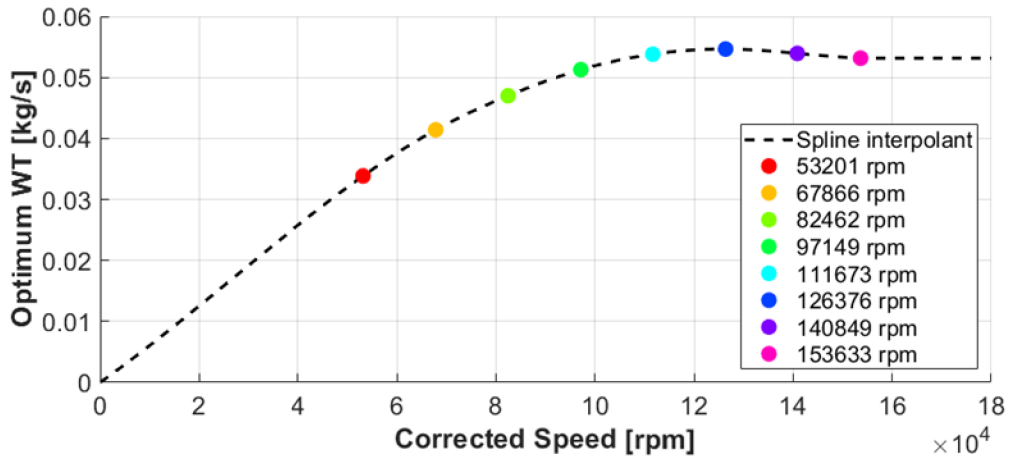


Figure 35: The optimum corrected mass flow rate fitted by a spline passing through the origin of the coordinate system (flat extrapolation to high corrected speeds)

With the fitting function for the optimum corrected mass flow rate (WT_{opt}) available, the normalized mass flow rate (WT_{norm}) can be calculated at each operating point of the map. WT_{norm} is defined as the ratio between the corrected mass flow rate at given operating point (WT) and the optimum corrected mass flow rate at the same level of expansion ratio [10, 20]

$$WT_{norm} = \frac{WT}{WT_{opt}} \quad (104)$$

Similarly to the case of the maximum efficiency (see Chapter 2.1.3), the fitting function for WT_{opt} is defined with respect to the corrected speed, so the optimum corrected speed at each expansion ratio must be found first using Equation 100.

2.1.6 Fitting the normalized mass flow rate

According to the literature all turbine operating points should lie on a single curve when plotted in the normalized mass flow rate versus normalized blade speed ratio diagram. In GT-SUITE, the fitting function is exponentiation in the form [10, 20]

$$WT_{norm} = c_m + BSR_{norm}^{m_{fit}}(1 - c_m) \quad (105)$$

where the constant c_m [-] and the exponent m_{fit} [-] are fitted parameters. Again, an optimization method must be used to determine their values, because the m_{fit} is in the exponent of BSR_{norm} . As it is a curve fitting problem (the minimization of RMSE), gradient based methods can be used (a convex objective function is expected), among which the Newton's can be recommended for its fast convergence and resistance to zigzagging (see Chapter 1.4.5). At the same time, the c_m is the value of WT_{norm} , where the y-axis is crossed. Similarly, the exponent m_{fit} determines the curvature of the fitting function and thus the intercept with the x-axis

$$BSR_{norm_WT_int} = \left(\frac{c_m}{c_m - 1} \right)^{\frac{1}{m_{fit}}} \quad (106)$$

where $BSR_{norm_WT_int}$ [-] is the value of BSR_{norm} , at which zero WT_{norm} is reached. It should be noted that normalized mass flow rate usually reaches zero at a much higher value of BSR_{norm} than normalized efficiency.

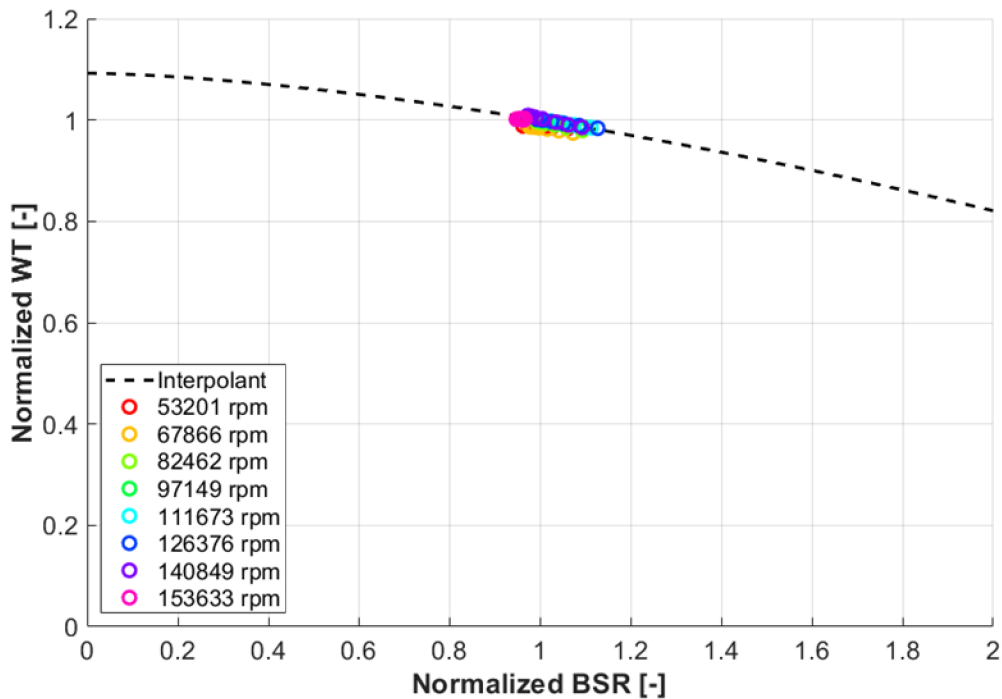


Figure 36: Normalized mass flow rate as a function of normalized blade speed ratio

2.2 Back-Calculation of Turbine Performance

Once the model is fitted, it can be used to generate the turbine performance data at any operating point from the supported range of speed and pressure ratio, which is the main purpose it was developed for. Thanks to this functionality, it is possible to compare the efficiency and the mass flow capacity of different turbine stages at equal operating conditions, or to carry out a working cycle simulation of a turbocharged engine (see Chapters 1.1.9 & 1.1.10). As the first step, however, it is convenient to visualize the fitted model in the form of fully extrapolated efficiency and corrected mass flow rate maps.

The process of generating a fully extrapolated turbine performance map involves evaluation of the fitted functions over a set of pre-defined operating points. A common practice is to group them into speed lines (i.e. points with the same corrected speed). It is convenient to select the same speeds that were identified in the source data, so it is easy to assess their alignment with the fit. In the case the source map consists of lines of a constant expansion ratio, an arbitrary set of corrected speeds covering the useful turbine speed range can be selected.

Turbine efficiency ($ETATM$) is obtained as a product of the normalized efficiency ($ETATM_{norm}$) and the maximum efficiency ($ETATM_{max}$) at certain expansion ratio (see Equation 99). The fitting function for $ETATM_{max}$ is, however, defined with respect to the optimum corrected speed, so it must be calculated using Equation 100 first. $ETATM_{norm}$, on the other hand, depends on the normalized blade speed ratio (BSR_{norm}) according to Equations 101 and 102. Finally, BSR_{norm} is defined by

Equation 98 and depends on the BSR (see Equation 46) and the BSR_{opt} (see Equation 97). The expansion ratio (PRT), therefore, remains the only independent variable and enters the process as a generated set of equidistant values.

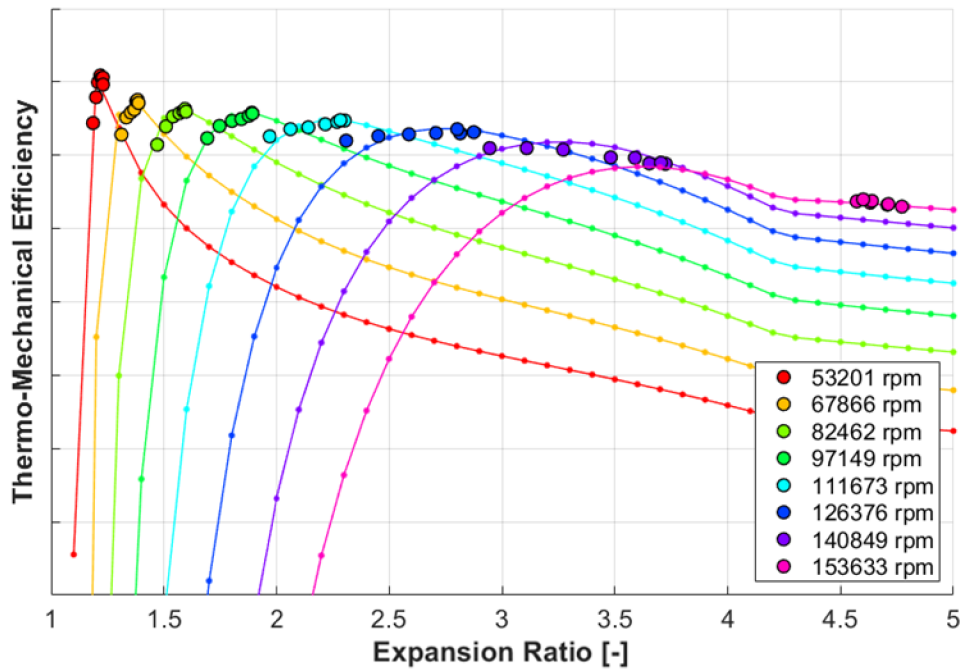


Figure 37: Fully extrapolated turbine efficiency map with equally distributed PRT points

The same procedure can be followed to generate a fully extrapolated map of corrected mass flow rate (WT), only with the difference that it is obtained as a product of the normalized mass flow rate (WT_{norm}) and the optimum corrected mass flow rate (WT_{opt}) at each expansion ratio (see Equation 104).

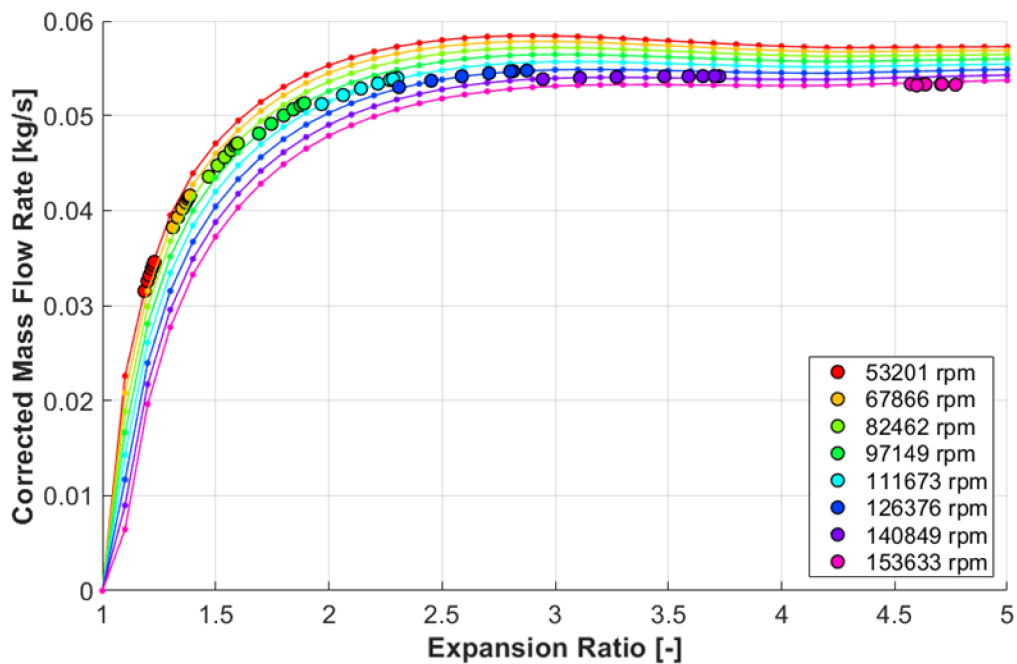


Figure 38: Fully extrapolated mass flow rate map with equally distributed PRT points

The fitting function for WT_{opt} is defined with respect to the optimum corrected speed, which must be calculated using Equation 100 first. WT_{norm} , on the other hand, depends on the normalized blade speed ratio (BSR_{norm}) according to Equations 101 and 102. The remaining steps are the same for both the efficiency and corrected mass flow rate. BSR_{norm} is obtained from Equation 98 and depends on BSR (see Equation 46) and BSR_{opt} (see Equation 97). The expansion ratio (PRT) is the only independent variable and enters the process as a generated set of equidistant values.

The map in Figure 38 was generated with a limitation of the minimum corrected mass flow rate, which is the reason why all speed lines appear to meet at the expansion ratio one and the zero corrected mass flow rate. At the same time it is apparent that the distribution of operating points at low expansion ratios is disadvantageous for a good resolution of both the efficiency and corrected mass flow rate in Figures 37 and 38. An efficient way to improve this is by creating a set of equidistant isentropic spouting velocity values, which are used to determine the corresponding expansion ratio.

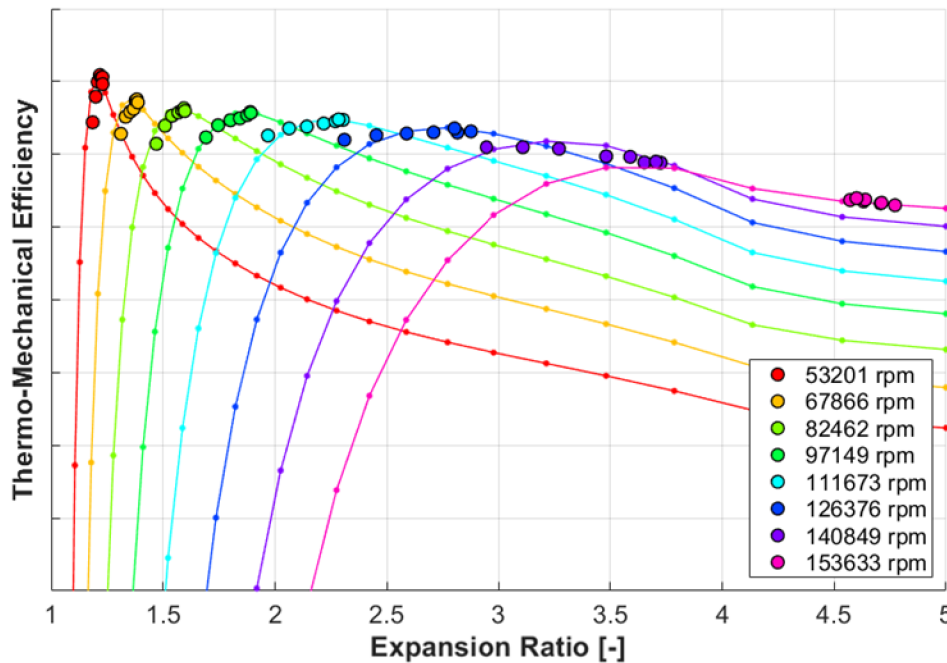


Figure 39: Fully extrapolated turbine efficiency map with PRT points derived from an equally spaced set of isentropic spouting velocity (c_0)

A formula for the isentropic spouting velocity can be derived from Equation 46 as

$$c_0 = \sqrt{2c_{p_exh}T_{1T_ref} \left[1 - \left(\frac{p_{2T}}{p_{1T_tot}} \right)^{\frac{\gamma_{exh}-1}{\gamma_{exh}}} \right]} \quad (107)$$

A simple reorganisation gives the expansion ratio

$$PRT = \left(1 - \frac{c_0^2}{2c_{p_exh}T_{1T_ref}} \right)^{\frac{\gamma_{exh}}{1-\gamma_{exh}}} \quad (108)$$

In Figure 39, the number of points per speed line is the same or lower than in Figure 37. The same approach can be followed to generate the corrected mass flow rate map.

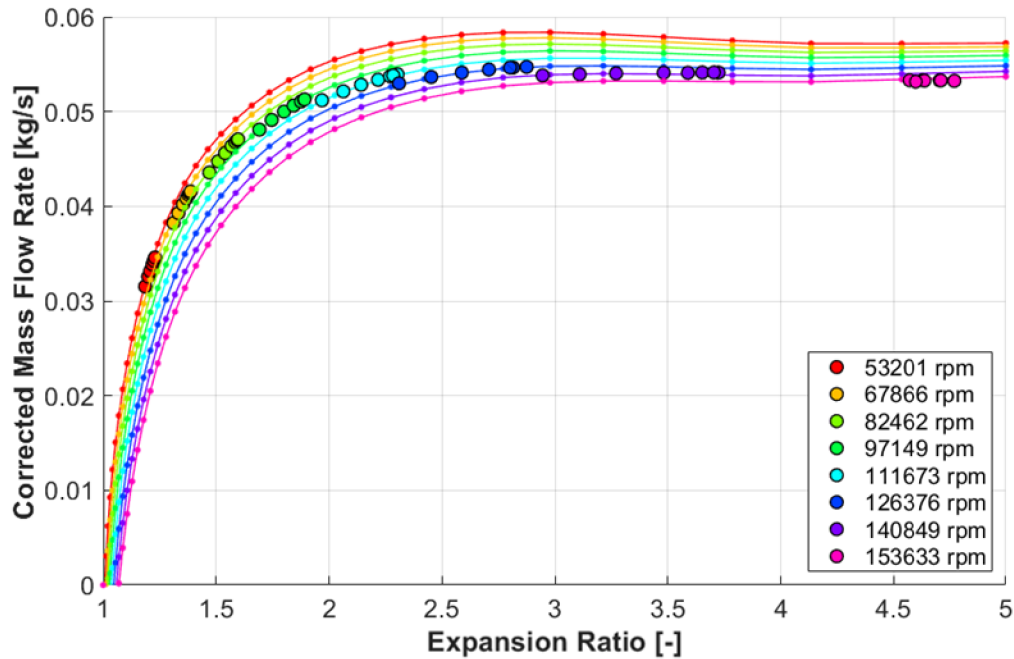


Figure 40: Fully extrapolated turbine mass flow rate map with PRT points derived from an equally spaced set of isentropic spouting velocity (c_0)

2.3 Fit Quality Assessment

The quality of a turbine performance model can be evaluated in terms of the difference between the source data and the fit. The corresponding values must be obtained using the same set of independent variables (the corrected speed and the expansion ratio). A common way to do the assessment is by means of descriptive statistics. Nevertheless, performing a visual analysis of characteristic parts of each extrapolated map is worthwhile too. The fitting algorithm is supposed to be applicable on a large scale of engineering tasks, so it needs to be robust to varying type and quality of source data.

2.3.1 Statistical analysis

The two key turbine performance parameters are the efficiency and the corrected mass flow rate. As the first step of a statistical analysis, the error between the model and the source data must be evaluated at each operating point (see Equation 59 for the definition of error and Chapter 2.2 for the interpretation of the model). Then, it is convenient to quantify the overall fit error using suitable indicators, which are called the *statistics*. To the basic ones belong the minimum, the maximum, the mean, the median, the mean squared error (MSE) and the root-mean-square error (RMSE, see Chapter 1.3.3).

Table 2: Statistics of the sample turbine map fit quality

	Efficiency	Corrected mass flow rate
Minimum error	-5.09%	-1.28%
Maximum error	2.85%	0.50%
Mean error	-0.42%	-0.28%
Median error	-0.27%	-0.07%
Mean absolute error	0.77%	0.43%
MSE	1.48	0.34
RMSE	1.22%	0.58%

The fit is not perfectly centralized as both the mean and the median error are different from zero for both the efficiency and corrected mass flow rate (see Table 2). Nevertheless, the difference is lower than a half of a percentage point, which is one tenth of the biggest efficiency deviation. The distribution of error sizes can also be visualised by means of a histogram. Figure 41 shows that most of the efficiency errors fall in the interval from -1% to 1%, which corresponds to approximately three quarters of the total number of data points. The relative corrected mass flow rate error is even less scattered with zero occurrence below -2% and above 1%.

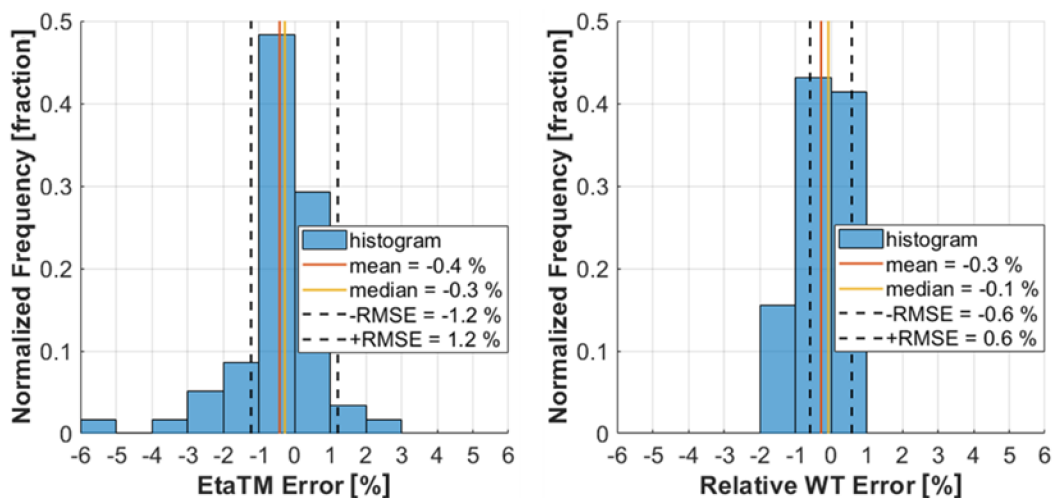


Figure 41: Histograms of fit error size for the efficiency (left) and the corrected mass flow rate (right)

A few data points, on the other hand, fall into the bins of efficiency error bigger than 3%. It is useful to visualize, what speed lines they belong to. This can be done by plotting the error values relative to the index of each operating point (see Figure 42).

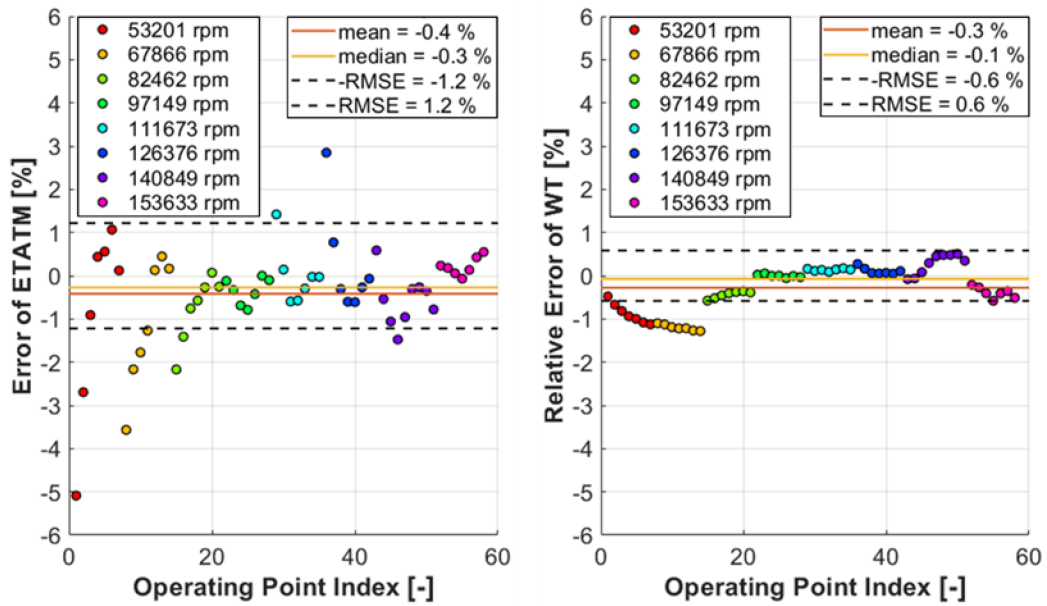


Figure 42: Fit error size as a function of data point index for the efficiency (left) and the corrected mass flow rate (right)

From the assessment of Figure 42 follows that the biggest efficiency errors are mostly connected with the lowest-speed lines. This is partly caused by the fact that the shape of the low-speed lines is sharp in the efficiency map (see Figure 39) and steep in the corrected mass flow rate map (see Figure 38). Therefore, a relatively small error in *PRT* results in a big error of the dependent variable. Mass flow rate can be measured directly on a gas stand, so this data is less noisy.

2.3.2 Analytical approach

Apart from the statistical evaluation, it is useful to visually check the shape of the extrapolated turbine performance maps too. One way to do that is by examining the maximum efficiency curve plotted over the expansion ratio in the fully extrapolated efficiency diagram (see Figure 43).

A discrepancy can be seen between the location of the maximum efficiency points derived from the model and those in the source map. The reason for the shift in the *PRT* coordinates is that the optimum *BSR* function is defined by linear regression (in the least squares sense) of the source-map operating points of the maximum efficiency, so the fit does not necessarily pass through all of them (see Figure 32). The Corresponding *PRT* coordinates at each maximum efficiency point can be determined using Equations 97 and 108

$$PRT = \left[1 - \left((kPRT + q)^{-1} \frac{\pi D_T \frac{NT}{60}}{\sqrt{2c_{p_ehx} T_{1T_ref}}} \right)^2 \right]^{\frac{\gamma_{exh}}{1-\gamma_{exh}}} \quad (109)$$

Further, the areas A and B in Figure 43 mark the points, where the maximum efficiency curve transitions from the main spline part defined by the source map data to the extrapolation regions (see Figure 33). One benefit of the flat extrapolation is that

outlying input map points are still reasonably represented by the turbine performance model (see operating points to the right of the area B in Figure 43). This is possible, since end-point efficiencies of the main spline part were defined using the peak efficiency points of the lowest and the highest speed line in the source map, so the extrapolated curve must pass through them.

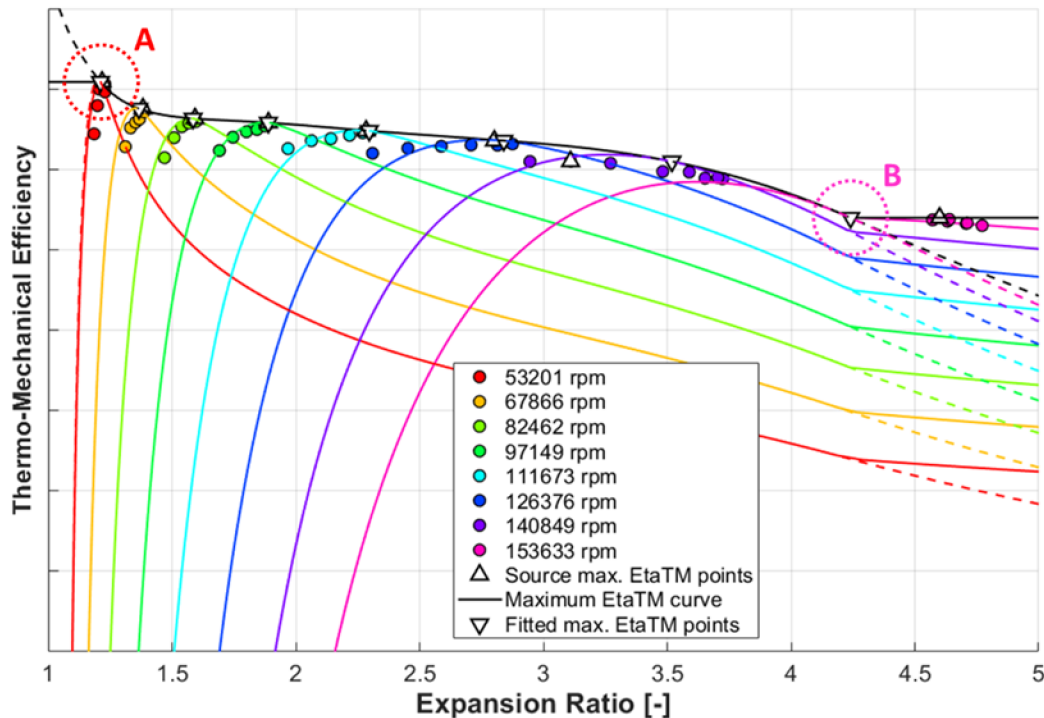


Figure 43: Fully extrapolated efficiency map, showing the highlighted maximum efficiency curve and points. The areas A and B mark the end-points of the main spline part of the maximum efficiency curve; the tangential extrapolation is dashed

The disadvantage of the flat extrapolation is that two sharp break points can be identified on the peak efficiency curve in Figure 43 (marked as the areas A and B), which is unphysical. One way to cope with it would be a tangential linear extrapolation instead of the flat one. The issue is, however, that the maximum efficiency curve may no longer pass through the operating points of the maximum efficiency at the highest and the lowest speed line, which impacts the agreement between the fitted model and the source data (see the dashed lines in Figure 43). Furthermore, the extrapolated efficiency may, in some cases, rise above one or fall below zero (where it is not desired).

The two areas of extrapolation can be identified in the corrected mass flow rate chart too (see Figure 44). The optimum corrected mass flow curve is, however, defined for the corrected speeds starting at zero (corresponds to $PRT = 1$), so the area A does not mark any break point. Although the extrapolation to high corrected speeds is still flat, the slope of the optimum corrected mass flow rate is almost zero there, so the transition is smooth again in the area B in Figure 44.

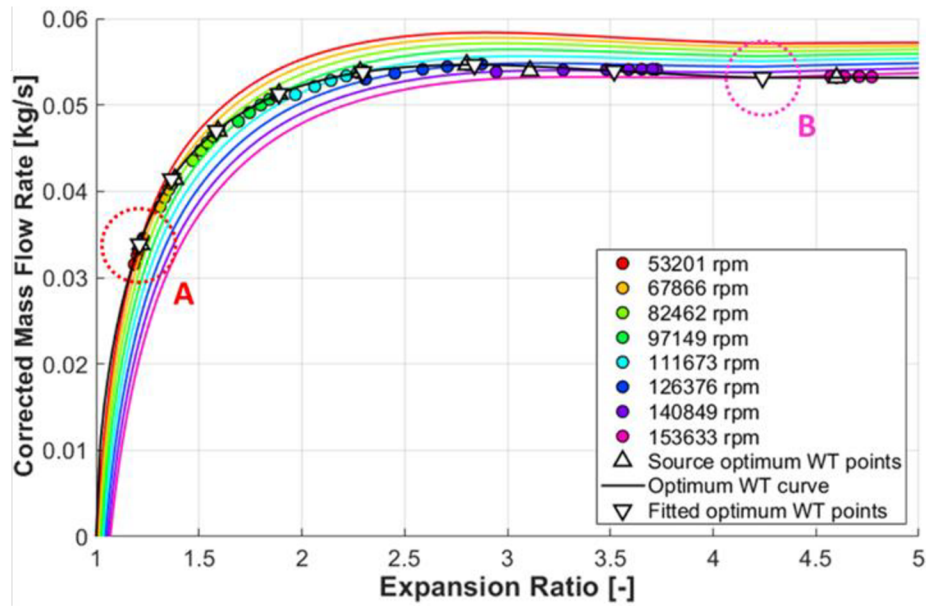


Figure 44: Fully extrapolated corrected mass flow rate map. The areas A and B mark the end-points of the main spline part of the optimum corrected mass flow rate curve

2.3.3 Robustness check

The above described methodology proved to be reasonable for modelling the sample turbine stage performance, the input data of which was acquired on a hot gas stand. Now, it should be checked that the same process can be repeated for a different data source too.

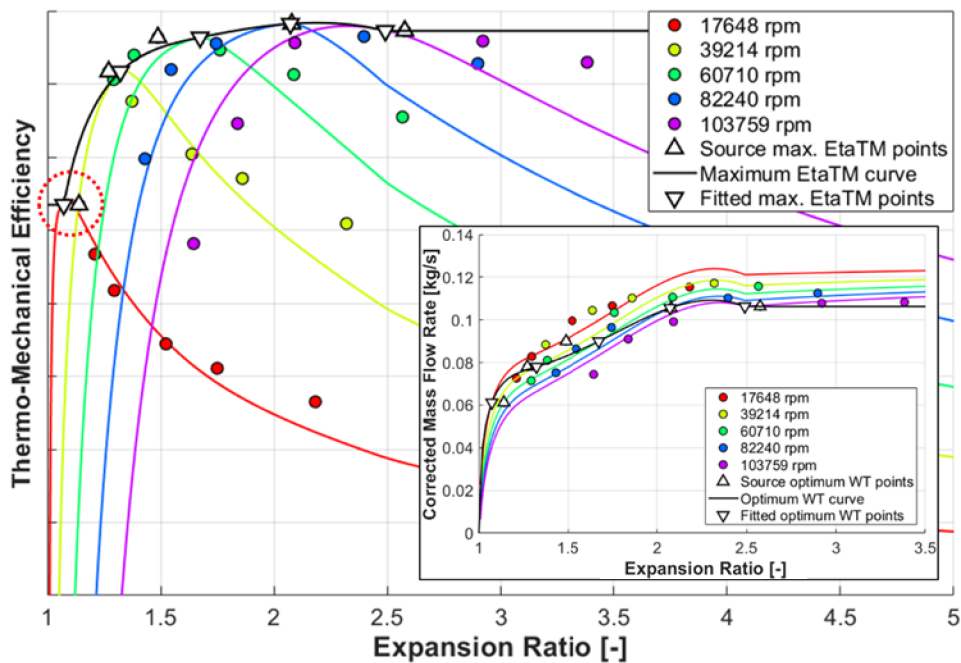


Figure 45: Fully extrapolated efficiency and mass flow rate maps for the turbine data obtained on a dynamometer

Another common way to obtain a turbine performance map is by means of a dynamometer measurement. A turbine stage alone (without the compressor) is

mounted on the rig, while the power output is measured directly on the shaft (see Chapter 1.1.4). A sample fitted turbine dyno map is shown in Figure 45. The fitting method failed in determining the maximum efficiency at low corrected speeds, where the measured data include the sub-optimal operating points only (see Figure 45). As a result, the extrapolated efficiency and mass flow rate maps include areas of significant distortion. This makes the models useless for engine thermodynamics simulations or other modes of use.

2.4 Sensitivity Study

Once the baseline fitting algorithm has been implemented, the relationship between the properties of the turbine performance model and the shape of the corresponding extrapolated maps can be studied. Out of the five fitted functions, two are determined directly by the input map data. These describe the maximum efficiency and the optimum corrected mass flow rate. Their modification would result in a proportional shift of the corresponding maps. The normalized efficiency and the normalized mass flow rate functions are linked to the first two and play the most important role in extrapolation. Finally, the optimum blade speed ratio is central to the turbine performance model and influences the complete shape of it.

The properties of the optimum *BSR* function are determined using the input map data directly (least squares approximation). Nevertheless, only a few operating points are selected for this purpose, which are supposed to capture the maximum efficiency at each speed line (see Figures 31 & 32). However, the standard mapping processes (e.g. on a hot gas stand) are not designed to look for the maximum turbine efficiency, so a significant uncertainty is associated with the resulting fit.

2.4.1 The shape of the optimum *BSR* function

The function of the optimum blade speed ratio over the expansion ratio is key to the turbine performance model. It influences the shape of both the efficiency and corrected mass flow rate maps. The most significant is the relationship to the location of the peak efficiency points at each speed line (see Figures 46 & 47). These can be interpreted as the anchor points for extrapolation, which means that complete speed lines are affected by any modification to the optimum *BSR* function.

It can be noted that the maximum efficiency curve is stretched with respect to expansion ratio for the modified optimum *BSR* function (see Figure 46). Although it is defined the same way in both cases, the independent variable of the maximum efficiency function is the corrected speed, so the link to *PRT* is affected by a change of the optimum *BSR* function. It is a general rule that lowering the *BSR* results in an increase of *PRT* (for a constant speed). The same is true for the optimum corrected mass flow rate.

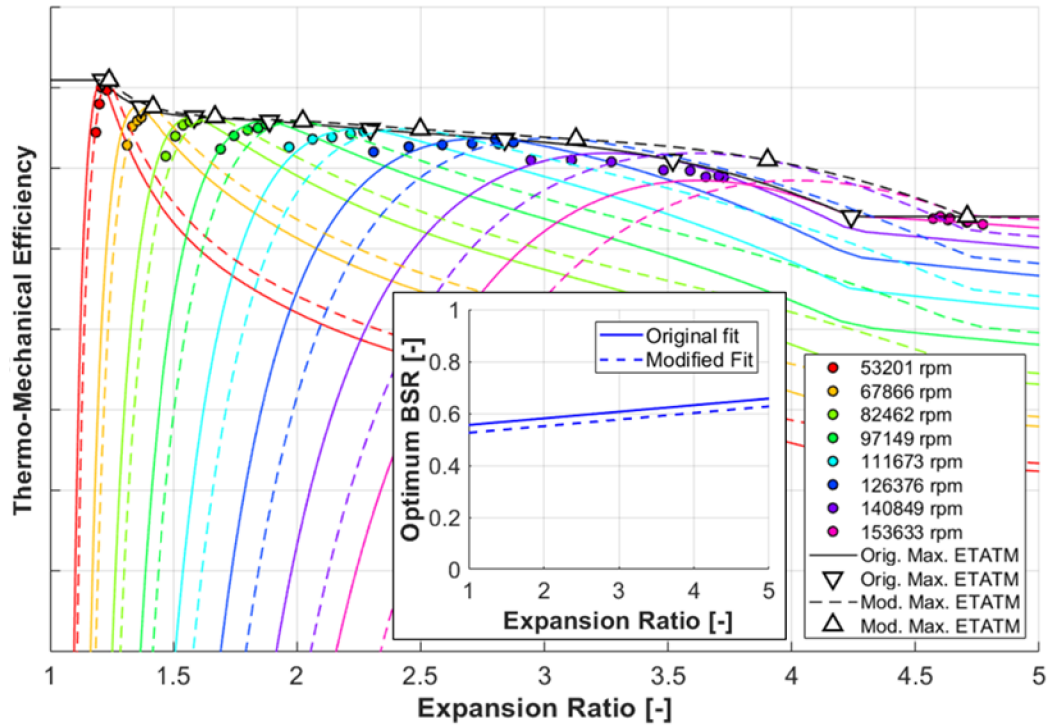


Figure 46: Fully extrapolated efficiency map for the original (full lines) and the modified (dashed lines) optimum BSR function

The shift of the optimum BSR function had a strong impact on the complete efficiency map (see Figure 46). Also, the sensitivity is bigger with an increasing expansion ratio.

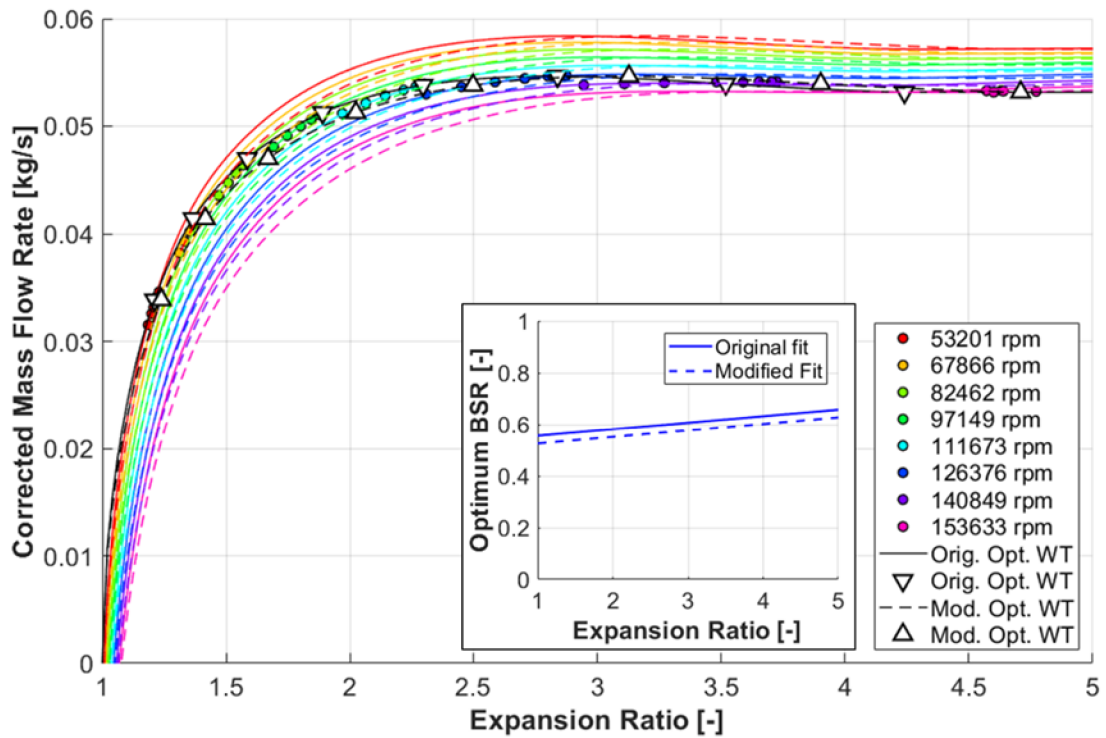


Figure 47: Fully extrapolated corrected mass flow rate map for the original (full lines) and the modified (dashed lines) optimum BSR function

Another important effect the modification of the optimum BSR fit has, is the altered relationship between the normalized efficiency and the normalized blade speed ratio of the map operating points. The maximum efficiency function is unchanged again in Figure 48.

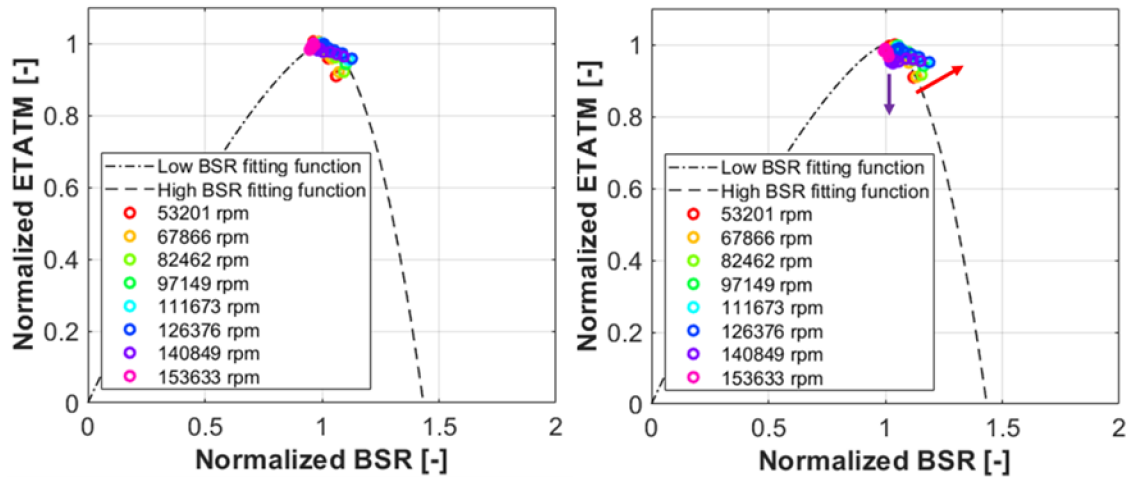


Figure 48: Normalized efficiency diagrams for the original (left) and the modified (right) optimum BSR function

The source map operating points displayed in Figure 48 are shifted towards the higher normalized BSR in reaction to the previously described optimum BSR function modification (corresponds with Equation 98 for the normalized BSR). Normalized $ETATM$, on the other hand, changes because the maximum efficiency function is defined relative to the corrected speed. Similar is the situation with the normalized mass flow rate in Figure 49.

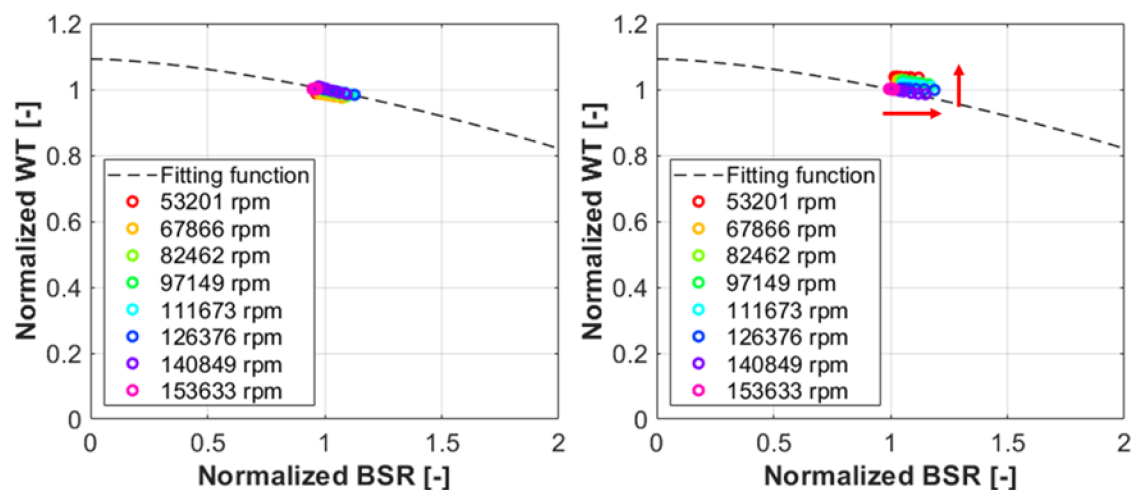


Figure 49: Normalized mass flow rate diagrams for the original (left) and the modified (right) optimum BSR function

From the presented analysis follows that it is possible to adjust a turbine fit by modifying the optimum BSR function. This operation, as described above, had a positive effect on the match between the source map points and the extrapolated efficiency at the lowest speed lines, but negatively impacted the same at the high speed lines (see Figure 46 and

Figure 47). Another issue is that the shape of the maximum efficiency and the optimum corrected mass flow rate can be affected in a potentially unwanted way with respect to the expansion ratio. One option to overcome this would be an appropriate scaling of the corresponding functions to make sure the relationship to PRT remains unchanged. Alternatively, the maximum efficiency and the optimum corrected mass flow rate can be defined directly as functions of PRT .

2.4.2 The shape of the normalized ETATM function

The normalized efficiency fit plays the most important role in extrapolation. It defines the slope of speed lines to the left and to the right from the maximum efficiency points (see Figure 50). As per the definition, the function has two-pieces (see Chapter 2.1.4), both of which can be modified independently.

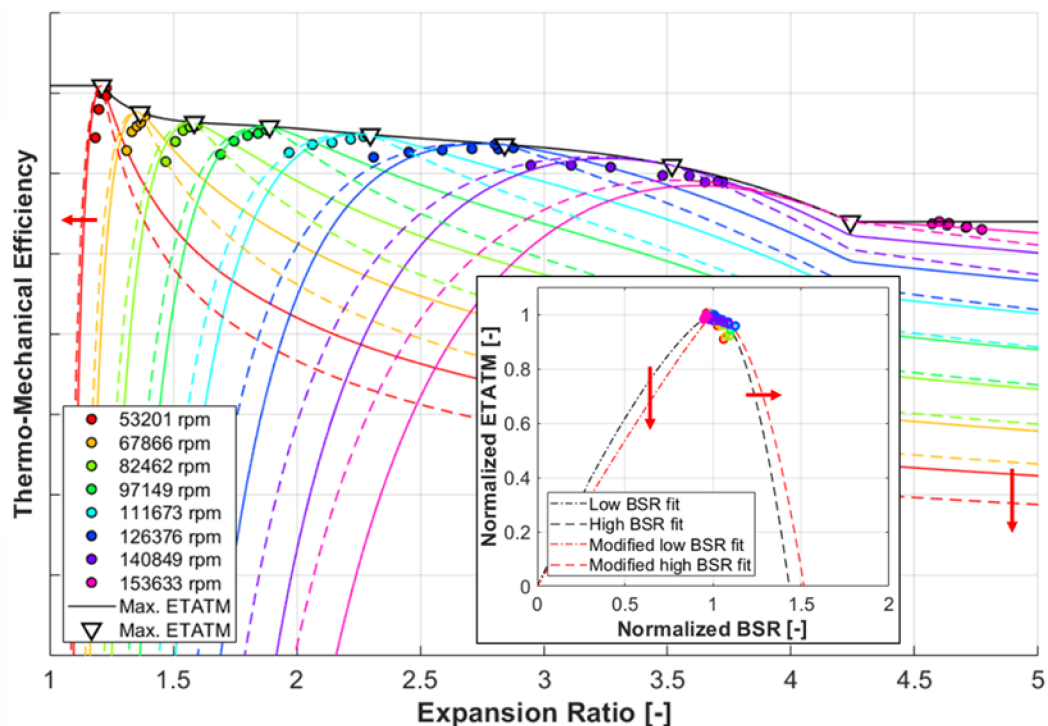


Figure 50: Fully extrapolated efficiency map for the original (full lines) and the modified (dashed lines) normalized efficiency fit

Extrapolation into the low BSR area influences the level of efficiency above the optimum expansion ratio for certain corrected speed and vice versa. Also, the normalized efficiency intercept at high normalized blade speed ratio (see Chapter 2.1.4) denotes the expansion ratio, at which the efficiency reaches zero for certain corrected speed. These are the points, where speed lines cross the x -axis in Figure 50.

By modifying the normalized efficiency function, it is possible to adjust the efficiency fit outside of the optimum point at each speed line (i.e. without affecting its position). Nevertheless, such a change impacts all speed lines at once, so it cannot be used to tweak local deviations.

2.4.3 The shape of the normalized WT function

Analogously to the normalized efficiency, the function of normalized mass flow rate versus normalized blade speed ratio defines the extrapolation outside of the optimum operating point at each speed line. However, the value of expansion ratio, at which the corrected mass flow rate reaches zero, is usually much lower compared to the case of efficiency. That is because the intercept of normalized mass flow rate with the x -axis is located at a much higher value of normalized BSR (see Chapter 2.1.6).

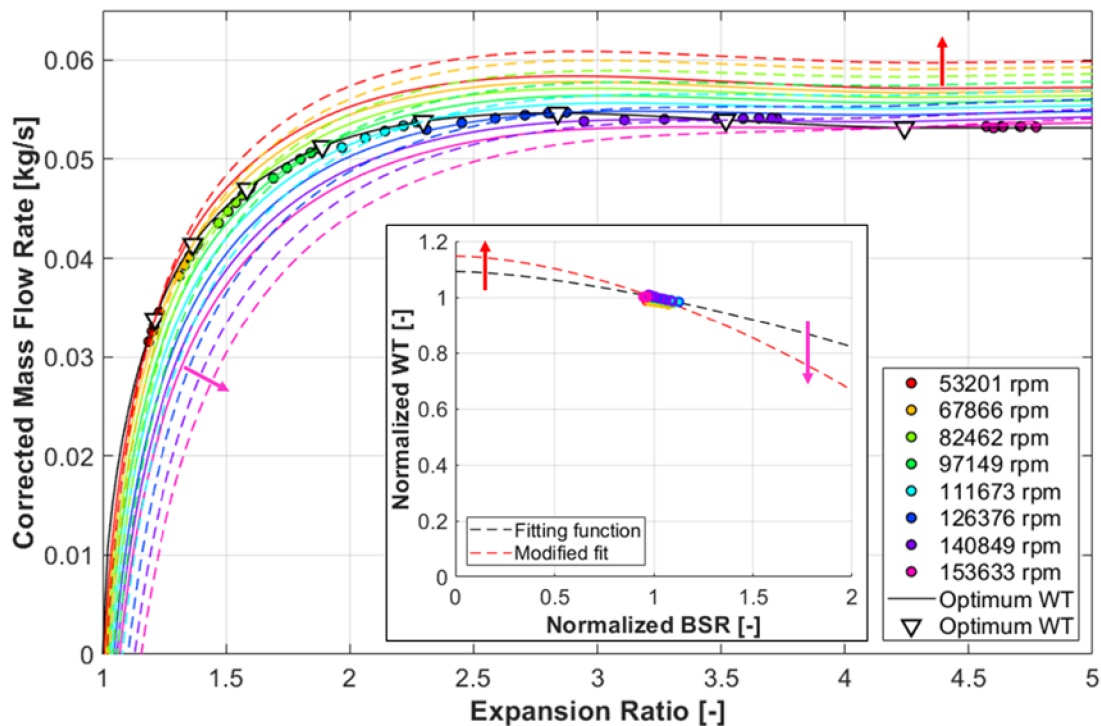


Figure 51: Fully extrapolated corrected mass flow rate map for the original (full lines) and the modified (dashed lines) normalized mass flow rate fit

The fact that mass flow rate can be zero or negative at PRT above one is caused by the centrifugal force acting on the gas against its direction of flow in radial and mixed-flow turbines. The higher the spinning speed, the bigger the force. One important conclusion, which can be drawn from the comparison of Figures 50 and 51, is that for certain turbine operating points with a positive mass flow rate the extrapolation of efficiency yields already negative values (just after the speed lines cross the x -axis in Figure 50). It means that although the flow direction remains unchanged, the turbine performs work on the fluid. This is caused mainly by the friction in the working gas, which is related to the gradient of speed between the wheel and the stator (e.g. in the gap between the wheel back disk and the centre housing). Therefore, the friction power increases with the wheel speed, as well as the pressure ratio, at which zero efficiency is reached (see Figure 50). Similar is the effect of bearing friction in the case of gas stand maps, where thermo-mechanical efficiency is usually evaluated.

3 OPTIMIZATION OF TURBINE MODEL PROPERTIES

A turbine performance model, as described in Chapter 1.1.10, consists of five characteristic functions. Three define the operating properties at peak efficiency, the other two control the extrapolation to sub-optimal conditions. It is, therefore, critical to the fitting process that the location of the maximum-efficiency operating points with respect to the independent variables (the expansion ratio and the corrected/reduced speed) is identified correctly. The issue is that the input map data, typically obtained on a hot gas stand, consist of scattered operating points that the peak efficiency is generally not included in. For this reason, the corresponding functions of the performance model must be estimated.

In the baseline fitting algorithm (see Chapter 2.1), the most efficient operating point is identified at each speed line or constant-expansion-ratio line. The functions for the maximum efficiency and the optimum corrected mass flow rate are defined by these points directly (see Chapters 2.1.3 and 2.1.5). On the contrary, the optimum BSR, the normalized efficiency and the normalized mass flow rate fits are determined using the least-squares method (see Chapters 2.1.2, 2.1.4 and 2.1.6). There is, however, no mechanism to check or fine-tune the quality of the resulting turbine performance model. The application of optimization methods can bring an additional value.

3.1 Optimum BSR Function

The optimum BSR function is key to the fitting process (see Chapter 2.4.1). The highest-efficiency operating points from the input map are approximated by a line in the least-squares sense in the baseline algorithm (see Chapter 2.1.2). An optimization method can be applied with the goal to minimize the root-mean-square error between the map operating points and the model (see Chapters 1.3.2 and 2.3.1).

Since the optimum BSR function is linear (see Equation 97), there are two independent parameters to be identified, so a multi-dimensional optimization method is needed. Also, the relationship between the root-mean-square error and the independent variables is strongly non-linear (five fitting functions must be evaluated), so the linear least-squares method cannot be applied. Therefore, the simplex, the gradient descent and the Newton's method will be considered (see Chapter 1.4). The best algorithm should not only find the solution but require the lowest number of the objective function evaluations too (to minimize the computing time).

To get a better idea about the features of the optimization problem, it is convenient to map and visualize the objective function in certain vicinity of the optimum. The corresponding intervals of the independent variables can be defined relative to the initial solution identified using the least-squares fit (see Chapter 2.1.2). The visualization is further simplified by the fact that the fitting function has only two independent parameters, so the response surface can easily be plotted in a 3D chart.

In the case of a data fitting, there is usually only one optimum that yields the lowest root-mean-square error of the model, unless a complex fitting function is selected, which can lead to the ambiguity of the solution. Furthermore, a monotonic increase in the objective function is expected together with the increasing distance from the optimum.

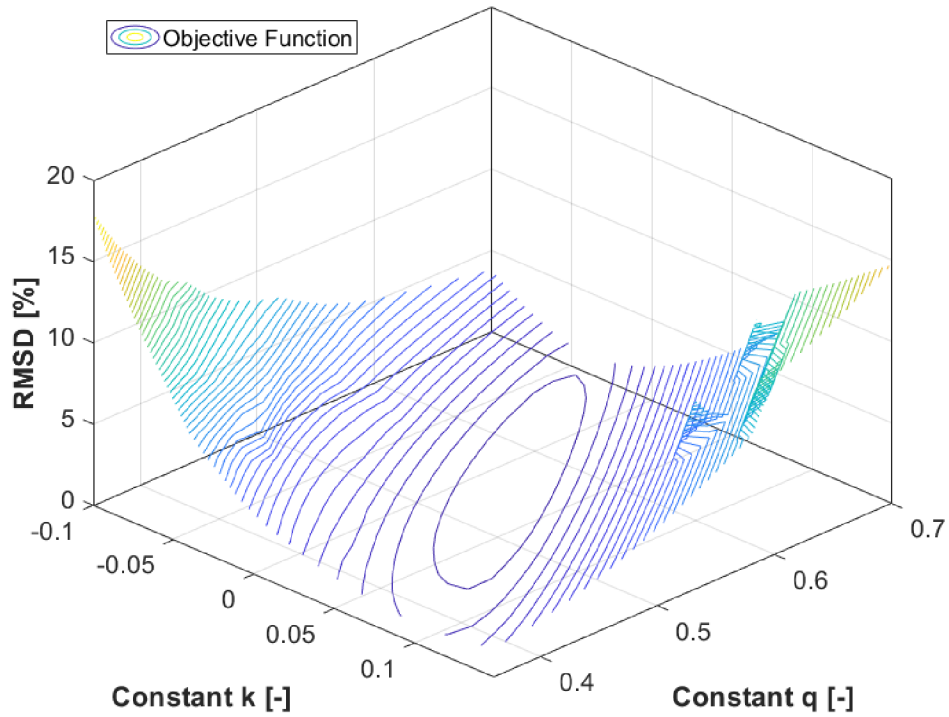


Figure 52: Mapping of the objective function relative to the optimum BSR fit properties

In Figure 52, the objective function appears to be convex near the optimum. At the same time, however, it seems to have the shape of a long narrow valley, which may lead to zigzagging when the gradient descent method is applied.

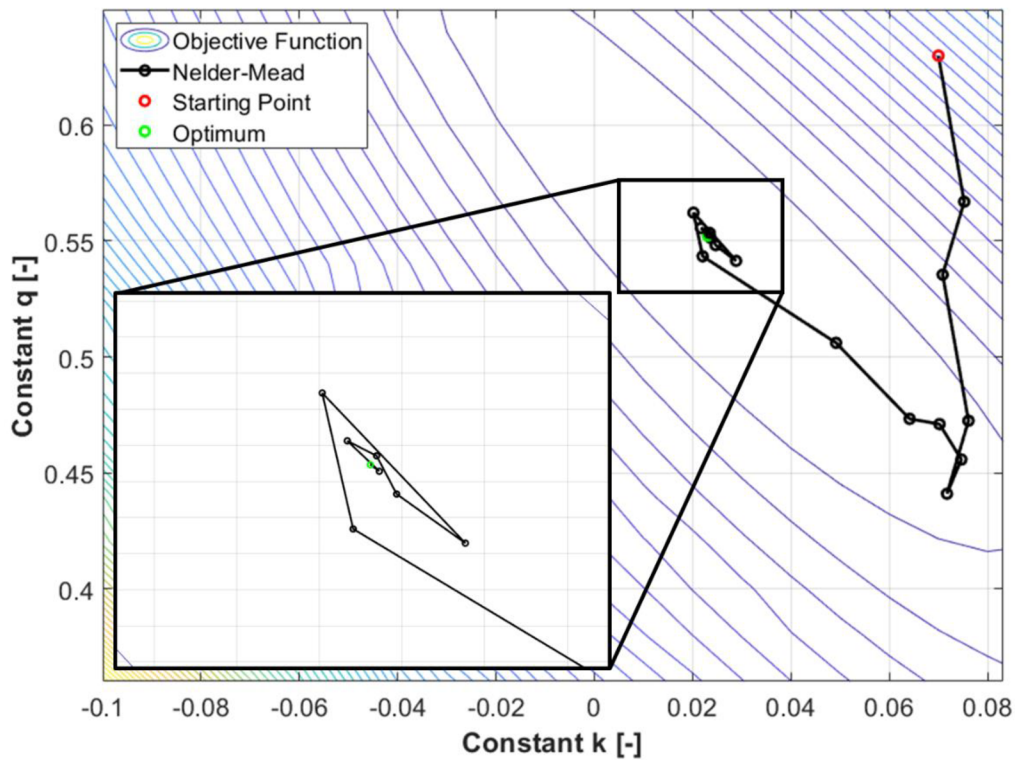


Figure 53: Performance of the simplex method (Nelder-Mead)

The simplex method can find the optimum, but it does not follow the shortest route from the starting point, which might suggest an unnecessarily high computing effort is needed (see Figure 53). In the case of a convex objective function, the shortest way to the optimum should follow the direction of the steepest descent. Therefore, the gradient descent method might be a good candidate.

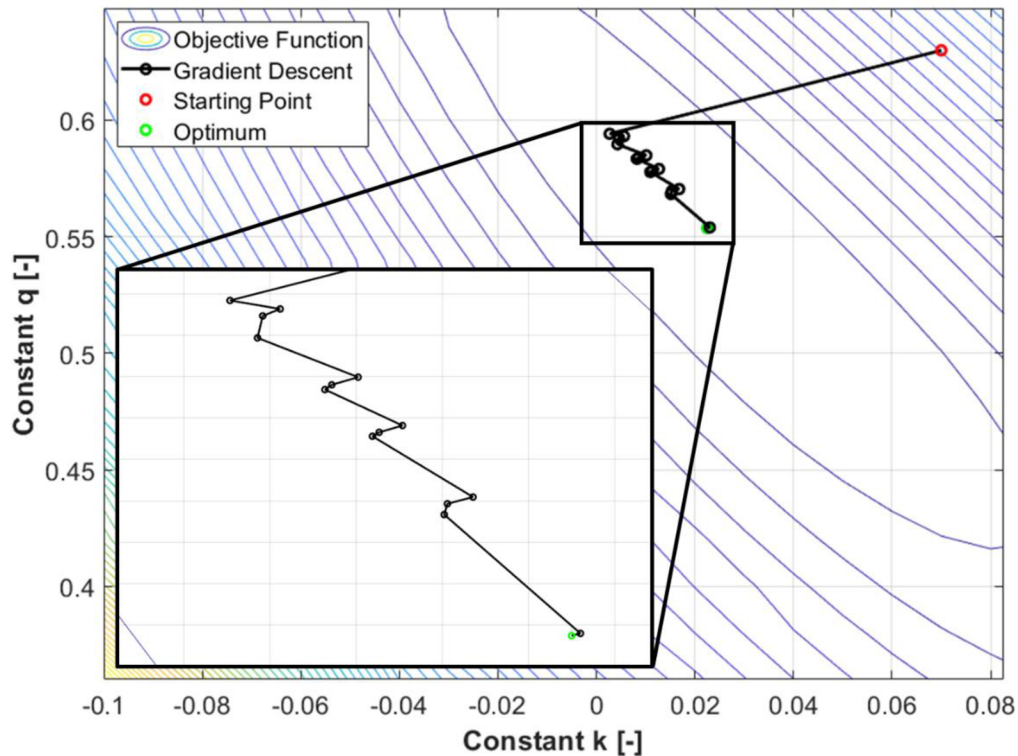


Figure 54: Performance of the gradient descent method

The test case confirmed that the gradient descent method was successful in selecting a convenient initial direction of search (see Figure 54). The subsequent iteration steps were, however, impacted by the so-called zigzagging, which makes the process significantly inefficient in terms of the speed of convergence and the computational demands. It is expected that this drawback would be eliminated using the Newton's multi-dimensional method. By approximating the local curvature of the objective function, it is possible to estimate, how the direction of the steepest descent changes with an increasing distance from the last discretization point, and to adapt the direction of search accordingly (see Chapter 1.4.5).

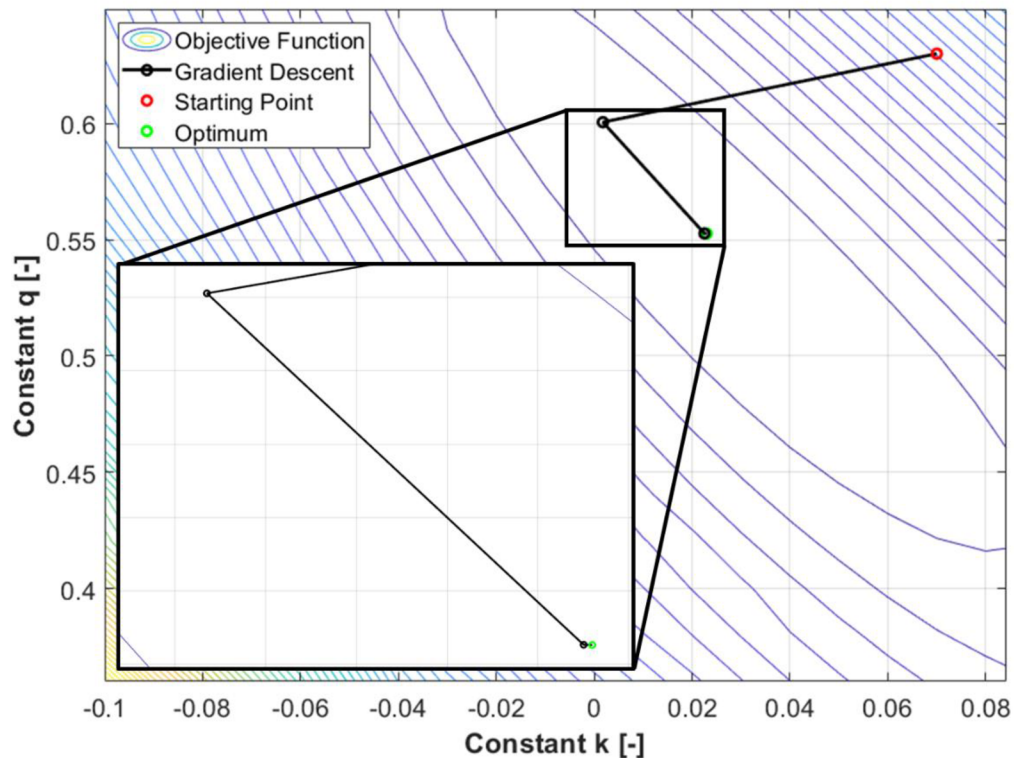


Figure 55: Performance of the Newton's multi-dimensional method

Based on the visualization of the Newton's multi-dimensional optimization, it can be concluded that the zigzagging is successfully mitigated (see Figure 55). Also, out of the tested options, this is the most efficient method in terms of the required number of iterations. The amount of overall objective function evaluations is comparable to the simplex method, nonetheless (see Table 3).

Table 3: Computational demands of each optimization method

Method	Number of iterations	Total objective function evaluations	Final objective function value	Final k	Final q
Simplex	26	51	0.783621%	0.02308	0.55234
Gradient descent + golden-section sr.	20	241	0.783626%	0.02250	0.55371
Gradient descent + quadratic fit	11	178	0.783610%	0.02284	0.55317
Newton's method + golden-section sr.	4	63	0.783612%	0.02299	0.55266
Newton's method + quadratic fit	4	50	0.783610%	0.02298	0.55285

The best overall performance is delivered by the Newton's method combined with the quadratic fit search, which is used to find local minima in the directions identified by the higher-level algorithm in each iteration step. The impact of the optimum BSR fit optimization on the overall map fit quality is summarized in Table 4.

Table 4: Fit quality statistics for the cases with and without optimization of the optimum BSR function (simplex method)

	With optimization		Without optimization	
	Efficiency	Mass flow	Efficiency	Mass flow
Minimum error	-2.37%	-0.64%	-5.09%	-1.25%
Maximum error	2.15%	0.60%	2.85%	0.49%
Mean absolute error	0.62%	0.36%	0.77%	0.42%
Mean (raw) error	0.15%	0.03%	-0.42%	-0.27%
Median (raw) error	0.24%	0.13%	-0.27%	-0.07%
RMSE	0.78%	0.40%	1.22%	0.57%

It can be concluded that the optimization of the optimum BSR fit enables a significant improvement of the overall fit quality with the sample measured turbine map. In the case of the thermo-mechanical efficiency, the standard deviation from the input data is lower by 0.44%. Comparison of extrapolated efficiency maps is included in Figure 56.

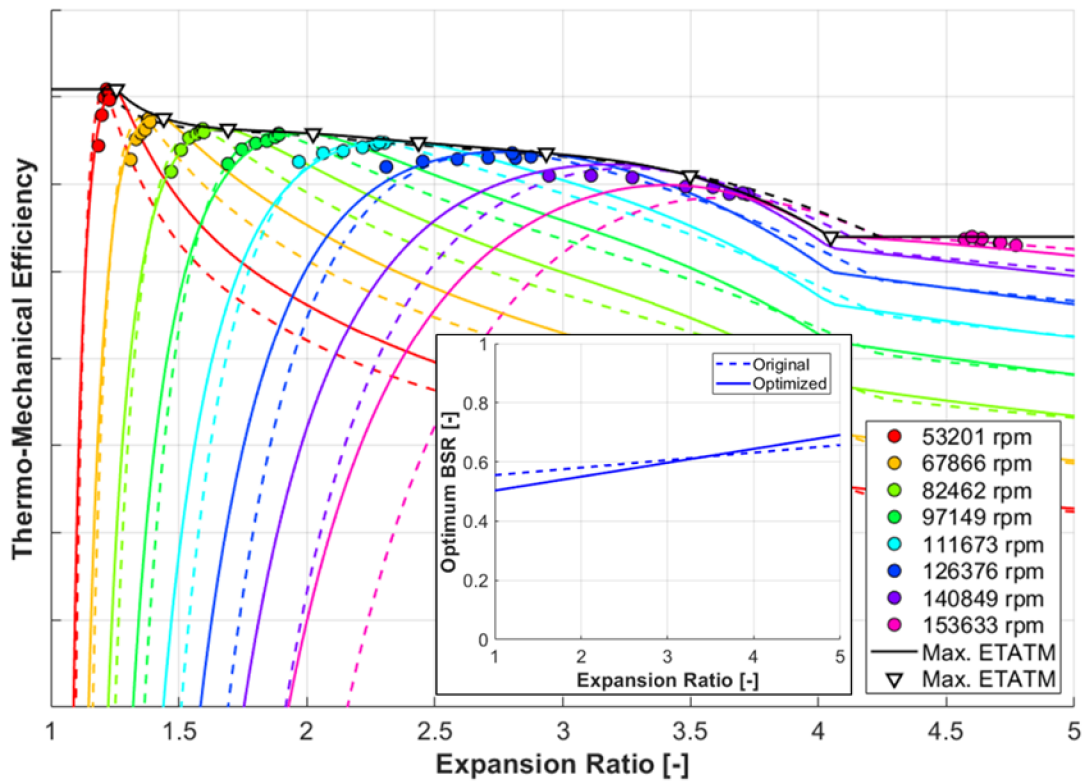


Figure 56: Fully extrapolated efficiency maps for the baseline (dashed) and the optimized (full lines) optimum BSR functions

The standard deviation of the corrected mass flow rate from the input data is lower by 0.17% with the optimized optimum BSR fit, however the overall appearance of the extrapolated mass flow map changed rather significantly as shown in Figure 57. This behaviour indicates low correlation between the standard deviation from the input data

and the shape of the corrected mass flow rate extrapolation to sub-optimal operating conditions. That is an important conclusion, which is discussed further in Chapter 4.

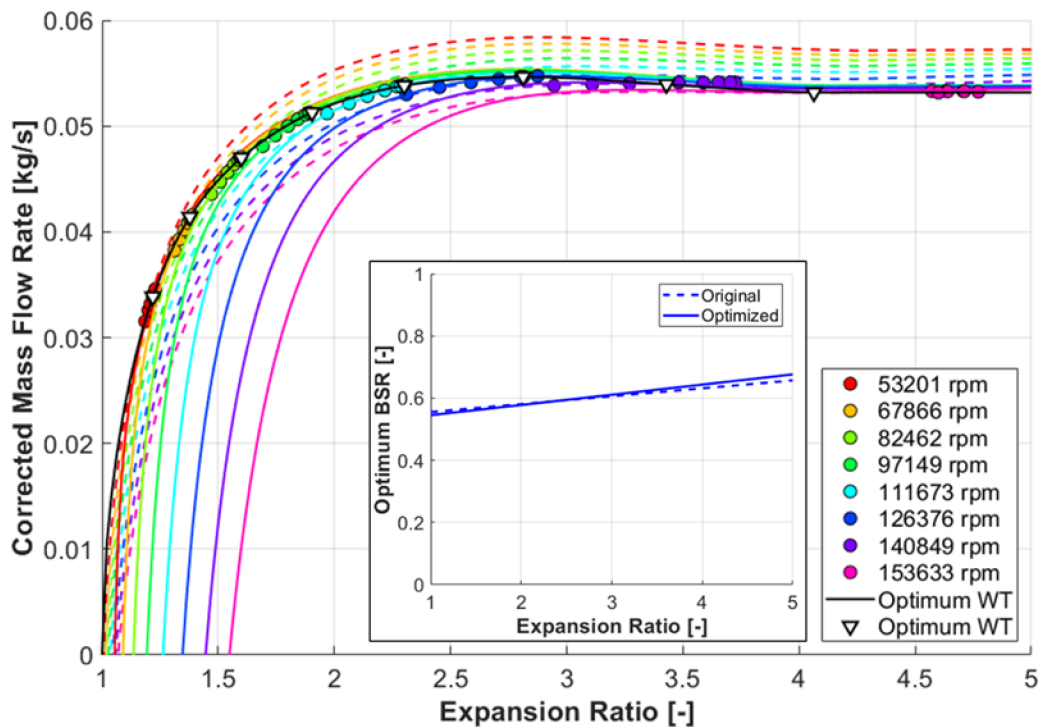


Figure 57: Fully extrapolated mass flow rate maps for the baseline (dashed) and the optimized (full lines) optimum BSR functions

3.2 Maximum Efficiency Function

Once the optimum BSR function has been identified, it can be checked, whether the maximum efficiency curve enables the best overall fit quality. It has been shown in Chapter 2.1.3 that a spline is a convenient interpolant, while the number of its nodes corresponds to the number of speed lines identified in the source map data. An optimization algorithm can be employed to minimize the root-mean-square error between the map operating points and the model by shifting the node efficiencies. To do that, a multi-dimensional method is needed. Therefore, the simplex, the gradient descent and the Newton's method will be tested.

Before the optimization begins, it is necessary to deal with the unphysical sharp bend of the maximum efficiency curve at the point of extrapolation to high corrected speeds (see Figures 56 & 43). On the one hand, the flat extrapolation approach is conservative, which is useful at low pressure ratios, where there is a risk of running above 100% with gas stand maps (see the area A in Figure 43). On the other hand, a linear extrapolation of the maximum efficiency at high pressure ratios is of low risk as long as a reasonable range is considered. A synergy with the maximum efficiency curve optimization should eliminate the large fitting error at the highest speed line, which was identified in Chapter 2.3.2 (see the area B in Figure 43).

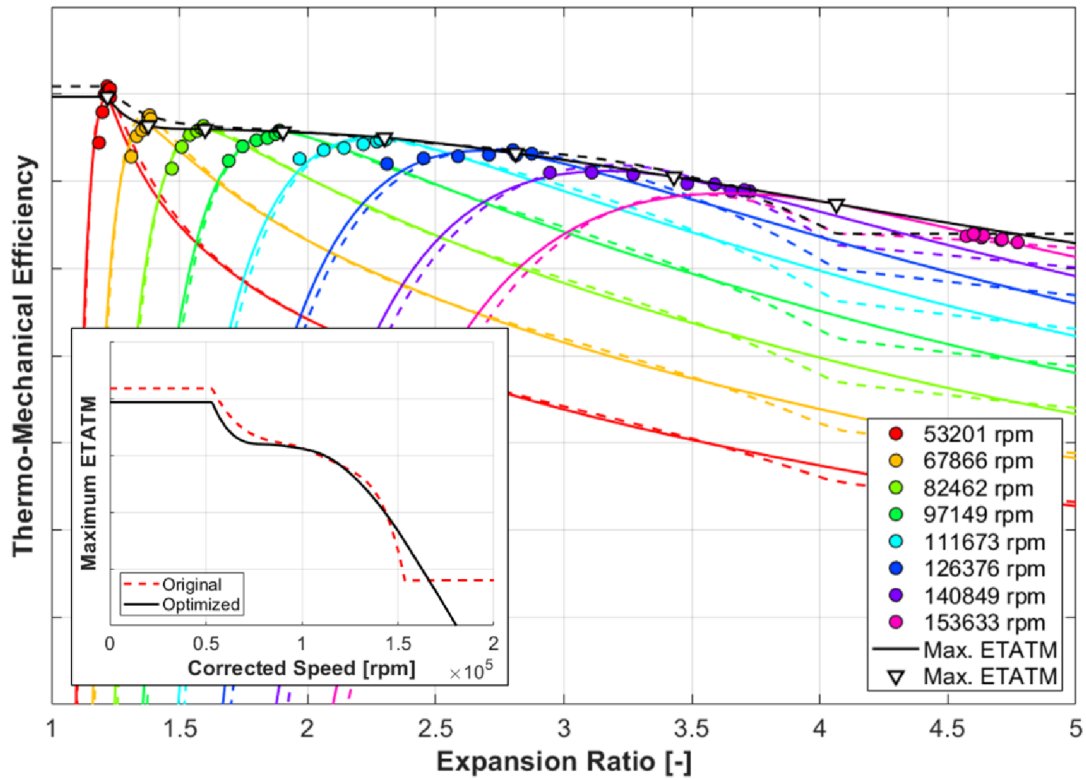


Figure 58: Fully extrapolated efficiency map after the optimization of the maximum efficiency spline (full lines) versus the initial fit (dashed lines)

In Figure 58, it can be seen that the optimization targeting the lowest RMS error caused lowering of the maximum efficiency curve at certain points. This may be undesired especially in the cases, where the efficiency at the actual measured points rises above the maximum efficiency curve (see the low-speed lines in Figure 58). Therefore, it is convenient to define an additional penalty function to make sure no measured point shows a higher efficiency than the maximum efficiency function at the same expansion ratio. To do that a sum of squared positive efficiency differences can be added to the overall mean square error as shown in the following equation

$$\begin{aligned}
 MSE = & \sum_i (ETATM_{data_i} - ETATM_{model_i})^2 \\
 & + \sum_{ETATM_{data_i} > ETATM_{max_i}} (ETATM_{data_i} - ETATM_{max_i})^2 \quad (110)
 \end{aligned}$$

where $ETATM_{data}$ [-] is the efficiency at a map data point, $ETATM_{model}$ [-] is the modelled efficiency at the same operating conditions (corrected speed and expansion ratio), $ETATM_{max}$ [-] is the maximum efficiency at the expansion ratio of the corresponding map data point. Following this approach, a compromise between the lowest overall fit error and the smallest maximum efficiency underestimation is targeted by the applied optimization algorithm. The result can be assessed in Figure 59.

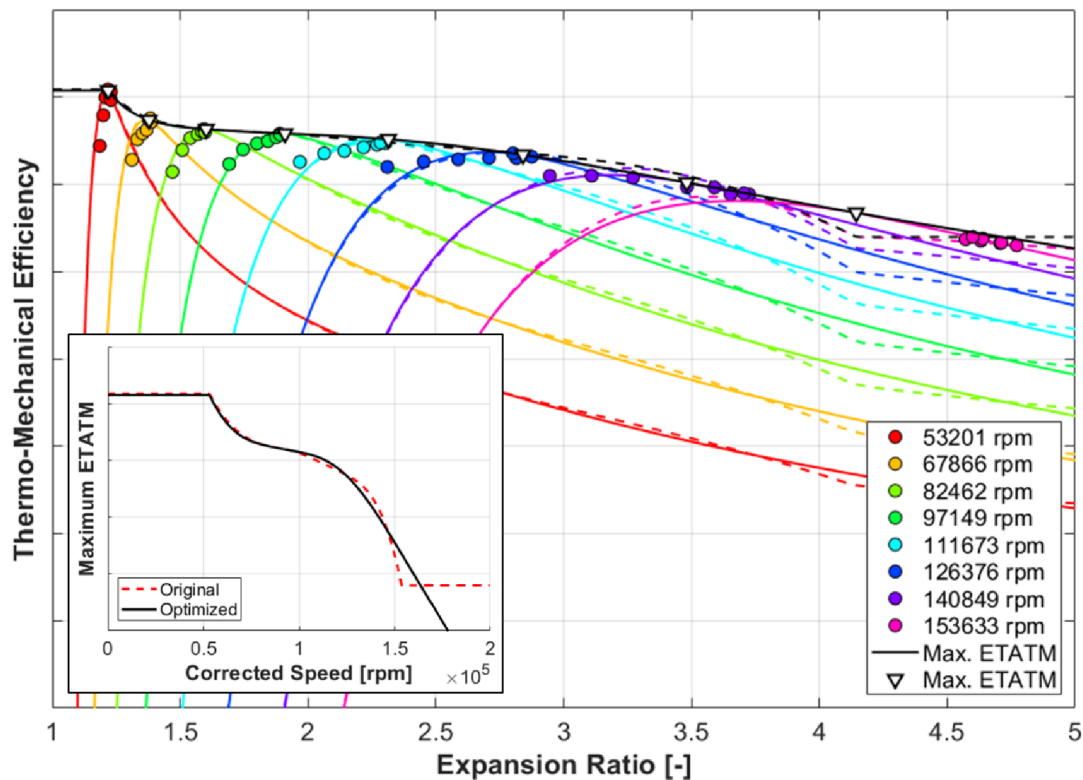


Figure 59: Fully extrapolated efficiency map after the improved maximum efficiency spline optimization (full lines) versus the initial fit (dashed lines)

The refined maximum efficiency optimization provides satisfactory results in terms of both the overall extrapolated map shape and individual data point deviations (see Figure 59). Further, the numerical performance of all the three tested optimization algorithms can be compared in Table 5.

Table 5: Computational demands of each optimization method

Method	Number of iterations	Total objective function evaluations	Final objective function value (efficiency/overall)
Simplex	136	215	0.7198% / 1.1198%
Gradient descent + golden-section sr.	24	446	0.7244% / 1.1244%
Gradient descent + quadratic fit	21	337	0.7241% / 1.1241%
Newton's + golden-section sr.	11	609	0.7214% / 1.1214%
Newton's + quadratic fit	11	579	0.7219% / 1.1219%

From the outcomes of the numerical methods assessment follows that although the simplex method required the highest number of iterations to converge to the optimum, it needed the least objective function evaluations. A detailed view at each method's speed of convergence is provided in Figure 60.

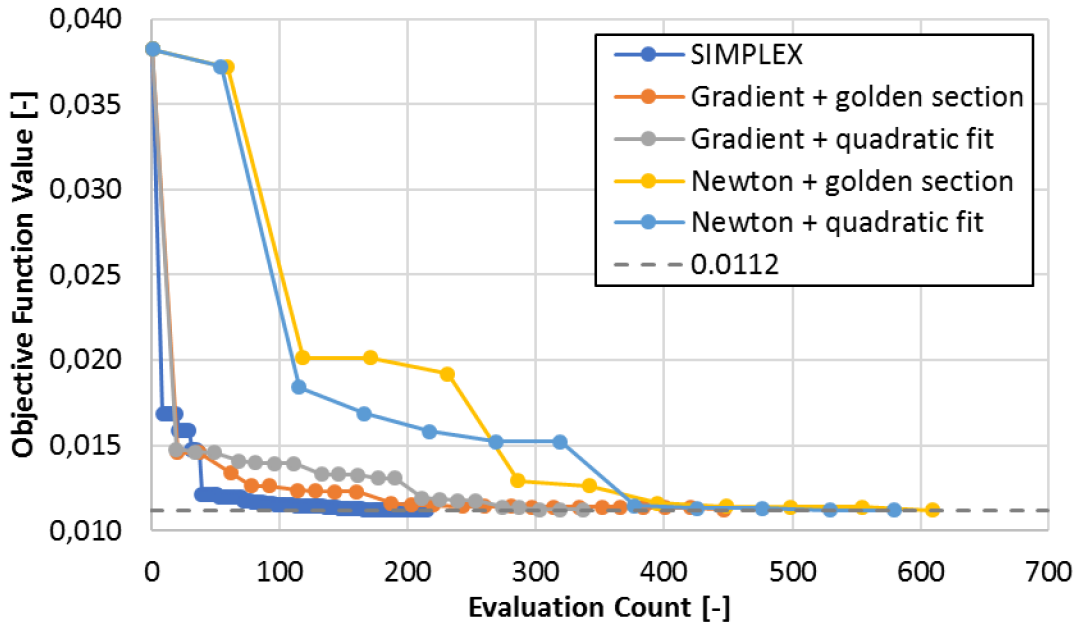


Figure 60: Convergence of the maximum efficiency spline optimization (the objective function is a sum of the efficiency and corrected mass flow rate RMS deviations)

3.3 Optimum Corrected Mass Flow Rate Function

The optimum corrected mass flow rate fit can be optimized in a similar fashion as the maximum efficiency function.

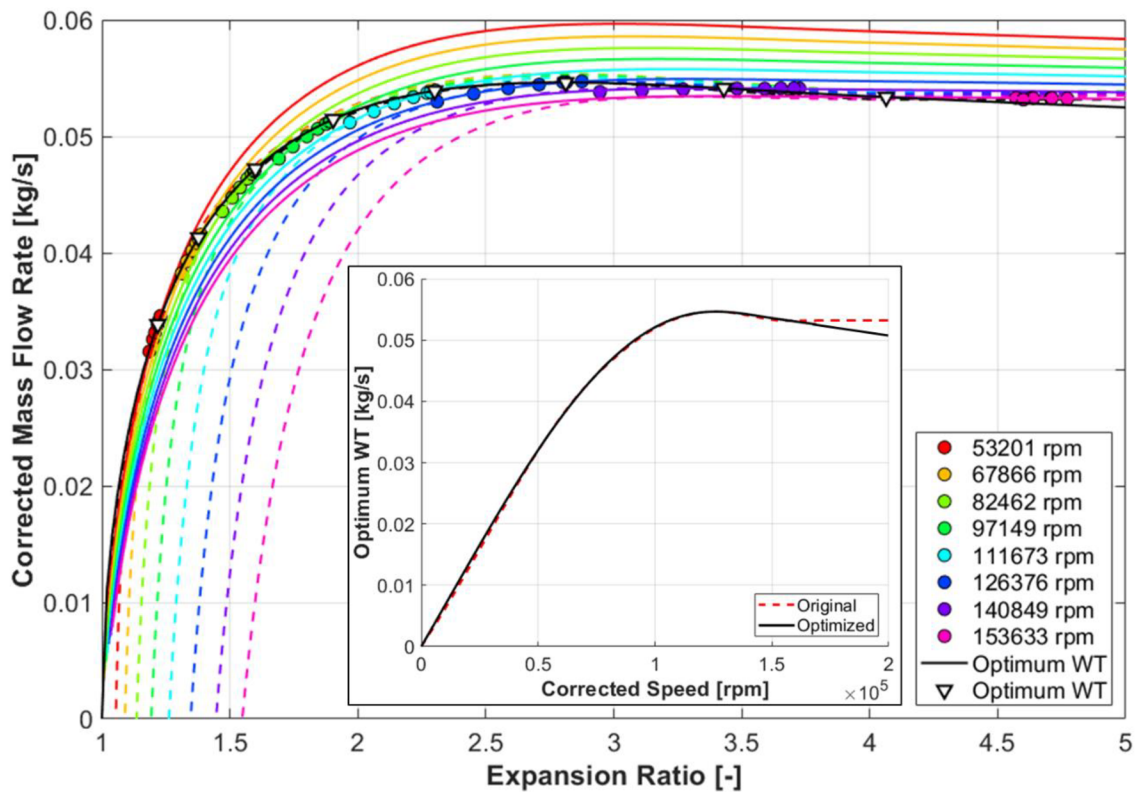


Figure 61: Fully extrapolated corrected mass flow rate map after the optimization of the optimum corrected mass flow rate spline (full lines) vs. the initial fit (dashed lines)

A multi-dimensional algorithm is employed to find such a corrected mass flow rate at each node of the corresponding spline that minimizes the overall root-mean-square-error between the map operating points and the model. At the same time, a linear extrapolation to high corrected speeds is applied to reduce the fit error of high-pressure-ratio data points. Despite the agreement with all the input data points is good, a big change in the overall corrected mass flow rate map appearance can be observed (see Figure 61). This re-confirms the low sensitivity of the standard deviation from the input data to the shape of the corrected mass flow rate extrapolation to sub-optimal operating conditions mentioned in Chapter 3.1 and further developed in Chapter 4.

Table 6: Computational demands of each optimization method

Method	Number of iterations	Total objective function evaluations	Final objective function value (mass fl./overall)
Simplex	89	163	0.3609% / 1.1409%
Gradient descent + golden-section sr.	20	384	0.3623% / 1.1423%
Gradient descent + quadratic fit	31	604	0.3624% / 1.1424%
Newton's + golden-section sr.	7	386	0.3610% / 1.1410%
Newton's + quadratic fit	18	950	0.3610% / 1.1410%

The comparison of the different optimization algorithms leads to a conclusion that the simplex method features the biggest robustness against variations in the task definition. It required less than a half of the objective function evaluations of the next best alternative among the tested algorithms (see Table 6). A detailed view at each method's speed of convergence is provided in Figure 62.

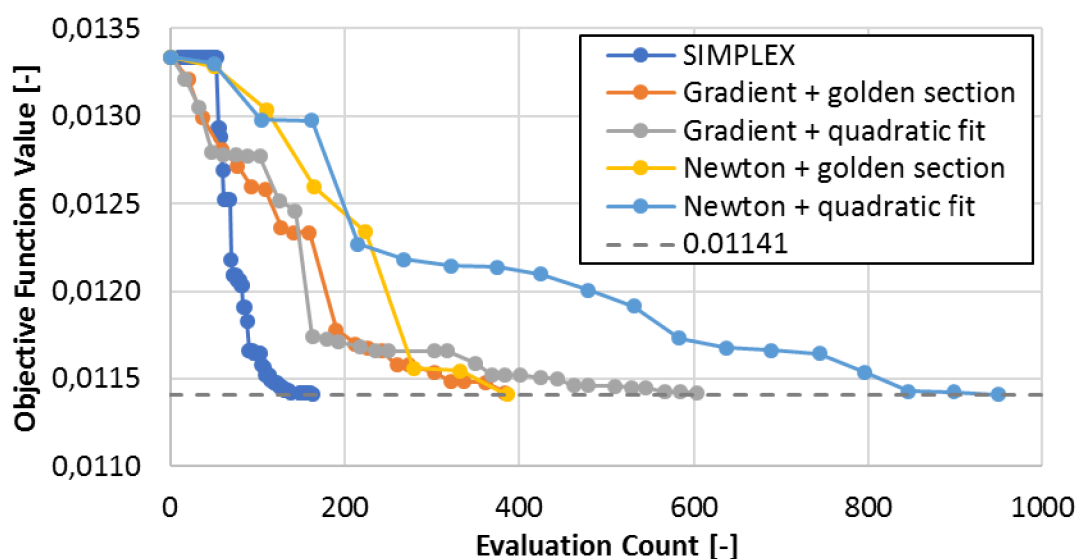


Figure 62: Convergence of the optimum corr. mass flow rate spline optimization (the objective function is a sum of the efficiency and corr. mass flow rate RMS deviations)

3.4 Complete Turbine Fitting Algorithm

As the three main sources of uncertainty related to the turbine map fit quality have been addressed one-by-one using optimization techniques, it is convenient to take a more global look at the overall process. In the first place, all optimization steps cannot be performed simultaneously, because they would influence each other and the algorithm would diverge. On the other hand, as the subsequent optimization steps backward-influence the earlier ones (in terms of the location of the optimum), higher fit quality can be achieved by repeating the process multiple times. Therefore, the complete turbine map fitting algorithm consists of three optimization tasks repeated in a loop, in which the best properties of the functions describing the optimum BSR, the maximum efficiency and the optimum mass flow rate are sought. This procedure finishes after the change of the RMS deviations of both the efficiency and corrected mass flow rate between two subsequent loops is lower than 0.001% (see Figure 63).

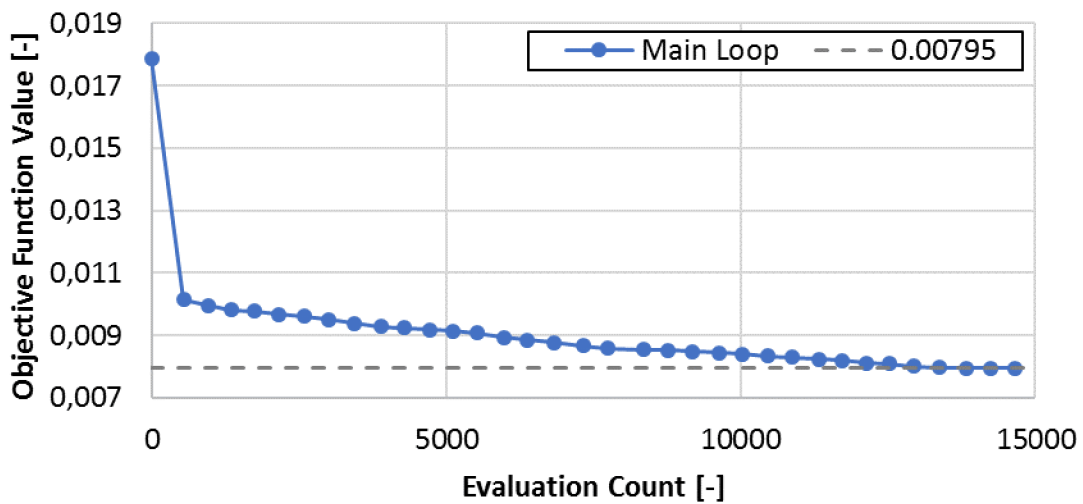


Figure 63: Convergence of the complete turbine map fitting algorithm (the objective function is a sum of the efficiency and corrected mass flow rate RMS deviations)

Plotting of the objective function value at the end of each main loop confirms that repeated optimization enables gradual reduction of the overall model error (see Figure 63). An evaluation of the final map fit quality is provided in Table 7.

Table 7: Statistics of the map fit quality with the complete algorithm

	With optimization		Without optimization	
	Efficiency	Mass flow	Efficiency	Mass flow
Minimum error	-2.65%	-0.208%	-5.09%	-1.25%
Maximum error	1.86%	0.146%	2.85%	0.49%
Mean absolute error	0.50%	0.067%	0.77%	0.42%
Mean (raw) error	-0.19%	0.005%	-0.42%	-0.27%
Median (raw) error	-0.10%	0.010%	-0.27%	-0.07%
RMSE	0.710%	0.085%	1.22%	0.57%

Based on the comparison with the initial map fit optimization (see Chapters 3.1, 3.2 and 3.3), it can be concluded that the repeated process helped to improve mainly the corrected mass flow rate fit quality. Its RMS deviation lowered from 0.361% to 0.085%, while the overall efficiency error reduced from 0.720% to 0.710% (see Chapters 3.3 and 3.2). The final and the original optimum BSR functions are compared in Figure 64.

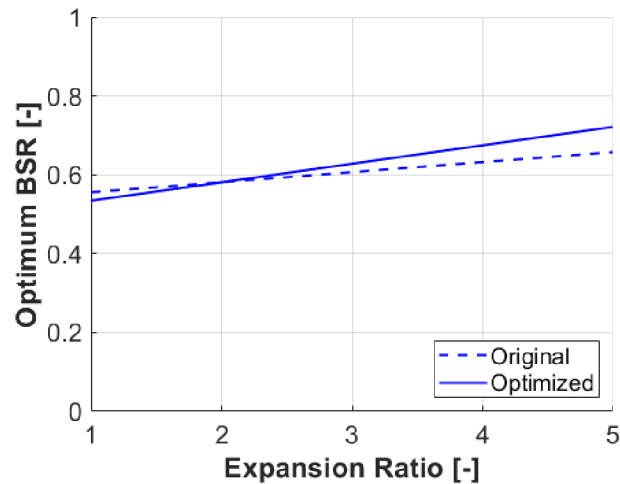


Figure 64: Comparison of the optimum BSR function at the end of the complete turbine fitting process (full line) with the initial non-optimized one (dashed)

The corresponding fully extrapolated efficiency map is shown in Figure 65. It can be noted that now the maximum efficiency curve is located further away from the data points of the highest speed line (compare to Figure 59).

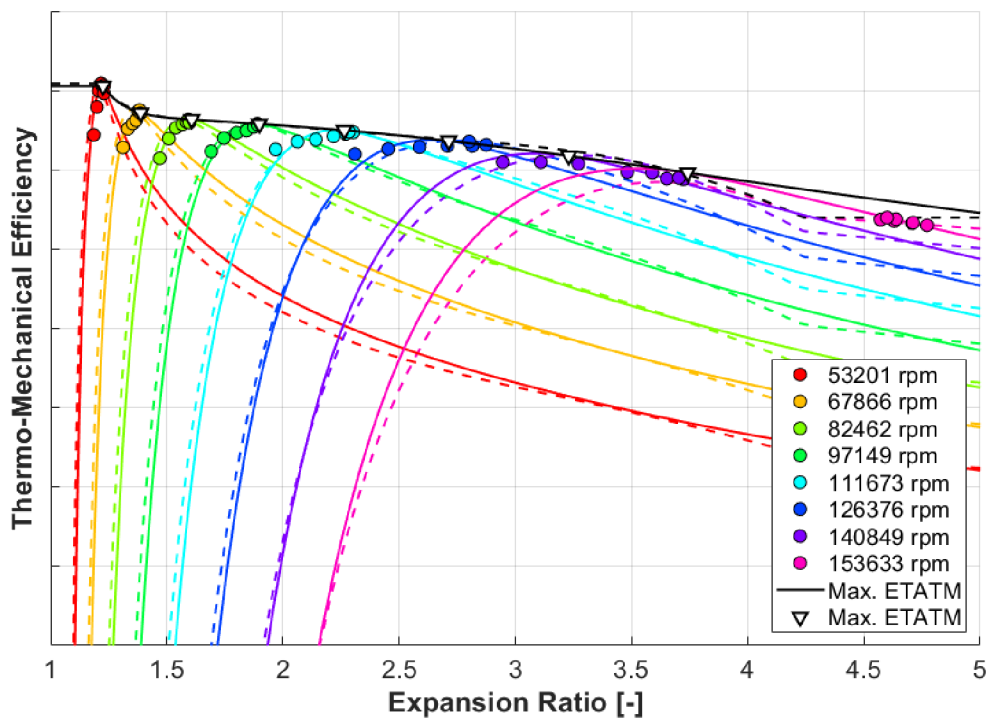


Figure 65: Fully extrapolated efficiency map at the end of the complete turbine fitting process (full lines) and the initial non-optimized one (dashed)

The fully extrapolated corrected mass flow rate map is included in Figure 66. Compared to the initial optimization (see Figure 61) the speed lines are even more condensed at low expansion ratios. Also, the distance of the optimum corrected mass flow rate curve from the data points of the highest speed line is increased again (like in the case of efficiency).

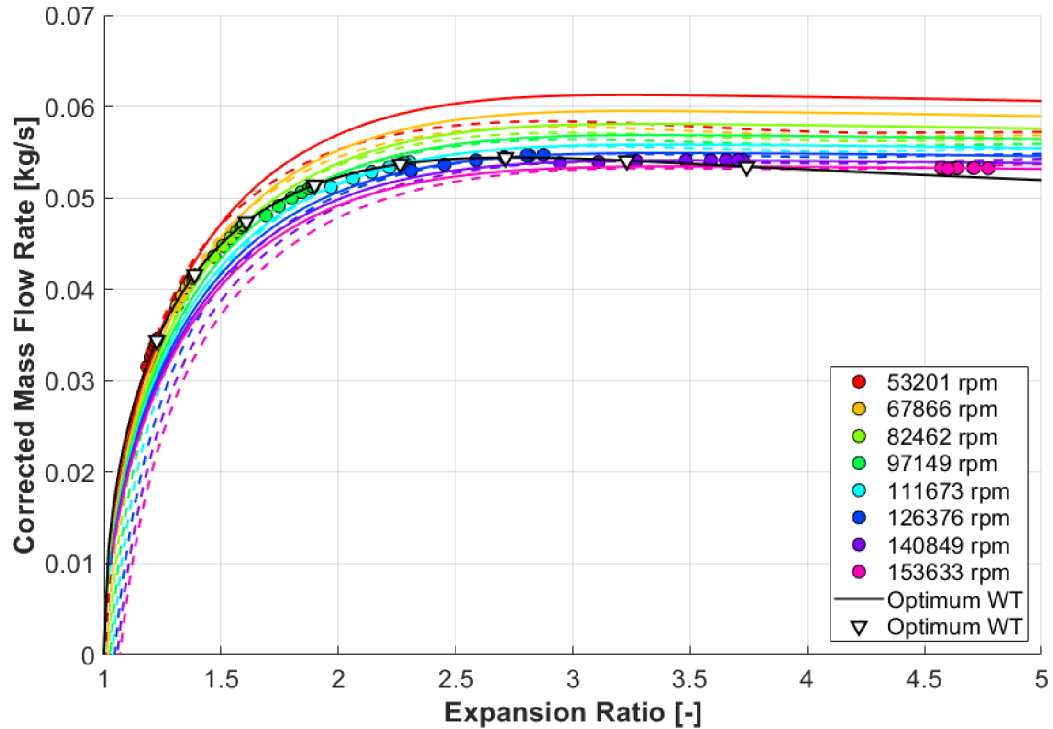


Figure 66: Fully extrapolated mass flow rate map at the end of the complete turbine fitting process (full lines) and the initial non-optimized one (dashed)

3.5 Evaluation

After the complete turbine performance fitting algorithm has been implemented, it can be concluded that optimization is a useful tool to improve the overall map fit quality. Further, it has been demonstrated that among the tested options the simplex method provides the biggest robustness, although the trajectory of search for the optimum is not necessarily the shortest. Overall, the computing time needed to fit the sample gas stand map using the above described procedure is less than half a minute on a moderately powerful contemporary PC.

In terms of fit quality, the standard procedure (as inspired by the existing commercial solution – see Chapter 1.1.10) shows a good performance with respect to capturing of both the overall trend of efficiency and the corrected mass flow rate near the optimum points. However, the shape of the corrected mass flow rate map in the extrapolated regions is not always satisfactory, which is discussed further in the following chapter.

4 NEW TURBINE FITTING ALGORITHM

Fitting a turbine map obtained by hot gas stand measurement is a particularly difficult task mainly for the low range of measurable operating conditions (see Chapter 1.1.4). It is, therefore, highly desirable to find ways to improve the accuracy of extrapolation based on physics principles. In Figure 61, for example, the speed lines are highly condensed at high expansion ratios, which is unexpected for a radial turbine. At the same time, Chapter 2.4.3 shows a strong correlation between the shape of the normalized mass flow rate function and the spread of speed lines in the corrected mass flow rate map, so it would be convenient to refine it. One possibility is to focus on the intercept of the normalized mass flow rate function with the normalized BSR -axis, which is linked to the points where speed lines cross the PRT -axis in a corrected mass flow rate map. In other words, it links the expansion ratio at zero mass flow rate to the spinning speed. Since most automotive turbochargers use radial turbines, the expansion ratio at zero mass flow rate increases with spinning speed due to the centrifugal force. The theory of radial equilibrium can be used to describe this relationship (see [11]).

4.1 Radial Equilibrium

The main idea of the radial equilibrium theory is that the pressure at the inlet of a turbine wheel is increased due to the centrifugal force acting on the mass of fluid enclosed in blade channels (see Figure 67).

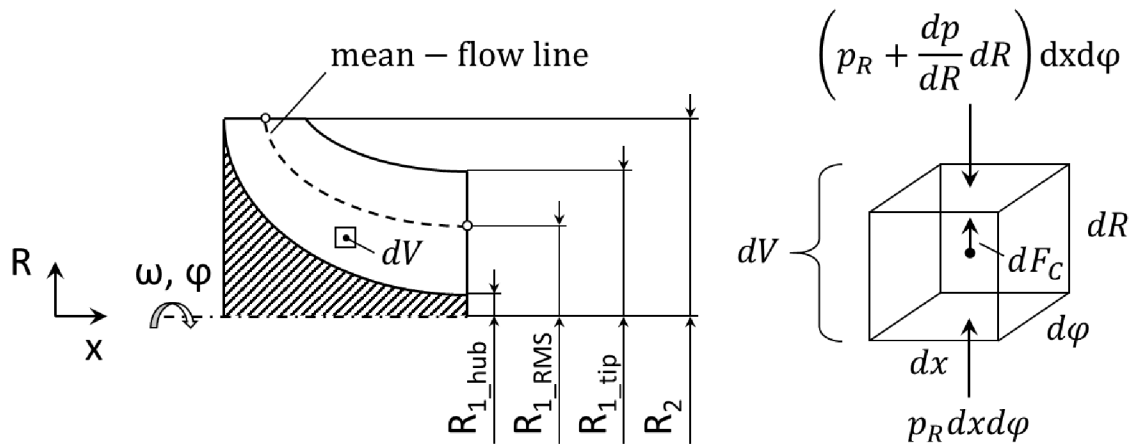


Figure 67: Radial equilibrium of a fluid element in the turbine blade channel

As there is zero mass flow rate, the system is assumed to be in equilibrium state. This simplifies the determination of the pressure distribution across the fluid, because the only force to balance is the centrifugal. It acts on every fluid element only in the radial direction (see Figure 67), so the equation of equilibrium can be written as [11]

$$\left(p_R + \frac{dp}{dR} dR\right) dx d\varphi - p_R dx d\varphi = dF_C \quad (111)$$

where p [Pa] is the pressure, p_R [Pa] is the pressure at the radius R [m], x [m] is the axial coordinate, φ [rad] is the polar coordinate and dF_C [N] is the centrifugal force acting on the fluid element. The latter can be calculated based on the second law of motion

$$dF_c = \rho dx d\varphi dR \omega^2 R \quad (112)$$

where ρ [kg/m³] is the local fluid density and ω [rad/s] is the angular velocity. At this point, it is good to emphasize that the objective of the centrifugal effect evaluation is to improve the fidelity of extrapolation of corrected mass flow rate. Therefore, the reference fluid properties are used in line with the theory of turbomachinery similarity. Any differences from the actual working fluid properties are accounted for by the correction of the mass flow rate and the wheel spinning speed (see Chapter 1.1.7).

By the combination of Equations 111 and 112 is obtained

$$\frac{dp}{dR} dx d\varphi dR = \rho dx d\varphi dR \omega^2 R \quad (113)$$

Further simplification leads to an expression for the pressure difference in a fluid element

$$dp = \rho \omega^2 R dR \quad (114)$$

Local fluid density in Equation 114 can be approximated by the adiabatic compression process [11]

$$\frac{\rho_2}{\rho_1} = \left(\frac{p_2}{p_1} \right)^{\frac{1}{\gamma_{exh}}} \quad (115)$$

where ρ_1 [kg/m³] and p_1 [Pa] are the density and the pressure (respectively) at the beginning of compression, ρ_2 [kg/m³] and p_2 [Pa] denote the corresponding quantities at the end of compression. Introduction of the adiabatic process in Equation 114 gives

$$dp = \rho_1 \left(\frac{p}{p_1} \right)^{\frac{1}{\gamma_{exh}}} \omega^2 R dR \quad (116)$$

The complete pressure difference between the wheel inlet and outlet points can be obtained by integration after the separation of variables

$$p^{-\frac{1}{\gamma_{exh}}} dp = \rho_1 p_1^{-\frac{1}{\gamma_{exh}}} \omega^2 R dR \quad (117)$$

It needs to be emphasized that the fluids in the volumes adjacent to the turbine wheel are assumed to be stationary, which means that there are no pressure gradients. This is particularly important at the turbine wheel outlet, where the radius of the blade channel spans from the hub to the blade tip (see Figure 67). To obtain the correct pressure difference, mean-flow radii (both inlet and outlet) must be used as integration limits. The mean-flow radius is defined as the root-mean-square of the minimum and the maximum radii [11]

$$R_{RMS} = \sqrt{R_{min}^2 + R_{max}^2} \quad (118)$$

where R_{min} [m] is the radius of the blade channel at the hub and R_{max} [m] is the blade tip radius (see Figure 67). Integration of Equation 117 gives

$$\frac{\gamma_{exh}}{\gamma_{exh} - 1} \left(p_2 \frac{\gamma_{exh}^{-1}}{\gamma_{exh}} - p_1 \frac{\gamma_{exh}^{-1}}{\gamma_{exh}} \right) = \frac{1}{2} \rho_1 p_1^{-\frac{1}{\gamma_{exh}}} \omega^2 (R_{2_RMS}^2 - R_{1_RMS}^2) \quad (119)$$

where R_{2_RMS} [m] is the bigger mean-flow radius and R_{1_RMS} [m] is the smaller mean-flow radius. Reorganization of Equation 120 enables the isolation of the expression for the overall pressure ratio induced by the centrifugal force as follows

$$\frac{\gamma_{exh}}{\gamma_{exh} - 1} \left[\left(\frac{p_2}{p_1} \right)^{\frac{\gamma_{exh}-1}{\gamma_{exh}}} - \left(\frac{p_1}{p_1} \right)^{\frac{\gamma_{exh}-1}{\gamma_{exh}}} \right] = \frac{1}{2} \rho_1 p_1^{-1} \omega^2 (R_{2_RMS}^2 - R_{1_RMS}^2) \quad (120)$$

Further simplification produces the final formula [11]

$$\frac{p_2}{p_1} = \left[1 + \frac{\gamma_{exh} - 1}{2\gamma_{exh}} \frac{1}{r_{exh} T_1} \omega^2 (R_{2_RMS}^2 - R_{1_RMS}^2) \right]^{\frac{\gamma_{exh}}{\gamma_{exh}-1}} \quad (121)$$

where T_1 [K] is the temperature at the turbine wheel outlet. It can be shown that the same pressure ratio is obtained using the corrected turbine speed and the reference outlet temperature, which are available in the standard turbine map. The modified equation is

$$\frac{p_2}{p_1} = \left[1 + \frac{\gamma_{exh} - 1}{2\gamma_{exh}} \frac{1}{r_{exh} T_{1T_ref}} \left(\frac{\pi N T}{30} \right)^2 (R_{2_RMS}^2 - R_{1_RMS}^2) \right]^{\frac{\gamma_{exh}}{\gamma_{exh}-1}} \quad (122)$$

The blade speed ratio at zero mass flow rate can be derived from Equations 46 and 122. On top of that, a significant simplification of the resulting formula is possible as

$$BSR_{WT_int} = \frac{R_{1_RMS}}{\sqrt{R_{1_RMS}^2 - R_{2_RMS}^2}} \quad (123)$$

where BSR_{WT_int} [-] is the blade speed ratio related to the intercepts of speed lines with the x-axis in the corrected mass flow rate map. To implement the theory of radial equilibrium in the turbine performance model, the normalized mass flow rate must reach zero at the appropriate normalized blade speed ratio (see Figure 68). The latter is obtained from Equation 98, while the optimum blade speed ratio is defined by Equation 97 and the expansion ratio at zero mass flow rate for the highest corrected speed in the map data (see Equation 122). The properties of the affected fitting function are given by Equation 106.

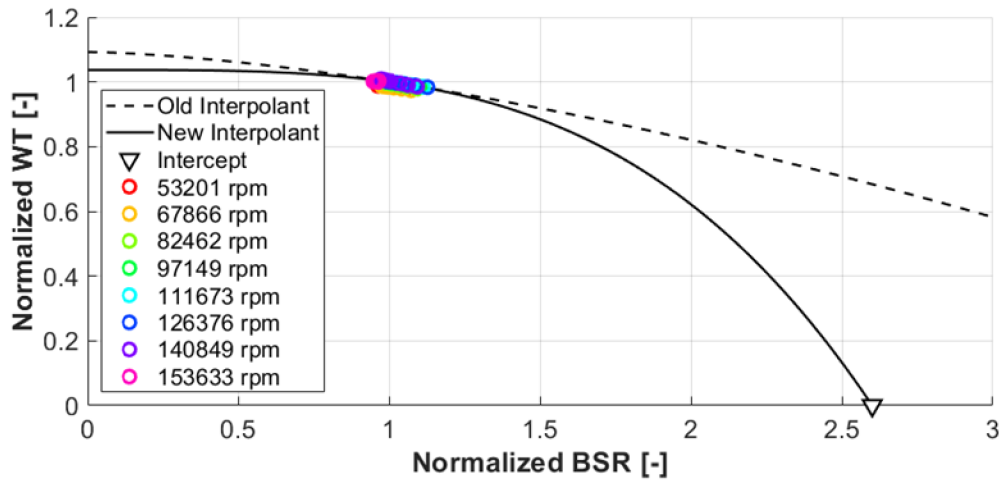


Figure 68: Normalized mass flow rate function with the intercept at zero mass flow rate determined using the theory of radial equilibrium (full line) and the baseline fit (dashed)

Figure 68 shows that the shape of the normalized mass flow rate function changed significantly after the introduction of the equilibrium point. The resulting fully extrapolated corrected mass flow rate map is displayed in Figure 69.

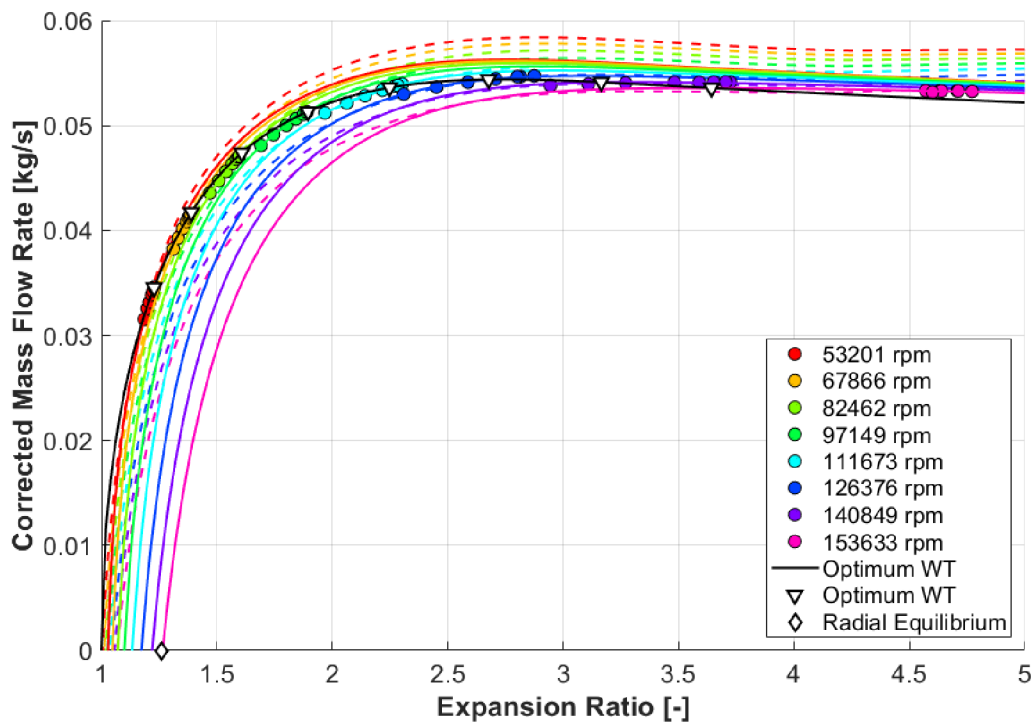


Figure 69: Fully extrapolated corrected mass flow rate map generated using the updated algorithm constrained by the radial equilibrium point (full lines) versus the baseline fit (dashed)

The newly extrapolated speed lines are condensed at high PRTs, which is not the desired state (see Figure 69). Therefore, further research is needed to investigate the context of the high-end corrected mass flow rate extrapolation. A convenient way is to compare the actual turbine behaviour with that of an ideal nozzle.

4.2 Ideal Nozzle Analogy

In the concept of ideal nozzle, the isentropic expansion of an ideal gas through an orifice of a fixed cross section is assumed. The ratio of the inlet and outlet pressures is constant and determines the spouting velocity (see Equation 106). The mass flow rate is obtained as a product of flow velocity, orifice area and gas density (all referred to the critical cross section). The latter can be derived from the isentropic expansion process (see Equation 115)

$$\dot{m}_0 = c_0 A_n \rho_1 \left(\frac{p_2}{p_{1,tot}} \right)^{\frac{1}{\gamma}} \quad (124)$$

where \dot{m}_0 [kg/s] is the mass flow rate and A_n [m²] is the orifice cross section. Corrected mass flow rate is obtained according to Equation 40

$$\dot{m}_{0_corr} = c_0 A_n \rho_1 \left(\frac{p_2}{p_{1,tot}} \right)^{\frac{1}{\gamma}} \frac{\sqrt{T_{1,tot}}}{p_{1,tot}} \frac{p_{ref}}{\sqrt{T_{ref}}} \quad (125)$$

It must be emphasized that the actual spouting velocity cannot rise above the speed of sound in the orifice, which is commonly referred to as choke. Under the conditions of choke, further increase of the expansion ratio does not lead to any increase of the flow velocity in the orifice, unless the gas temperature increases too. This effectively limits the minimum static pressure in the orifice, which is commonly referred to as the critical pressure. It can be determined using the formula for the critical pressure ratio [9]

$$\beta_{crit} = \frac{2}{\gamma + 1} \frac{\gamma}{\gamma - 1} \quad (126)$$

where β_{crit} [-] is the ratio of the static pressure inside the orifice and the inlet total pressure. Although the maximum effective expansion ratio at choke is limited, the mass flow rate still increases together with the inlet pressure due to the increasing gas density (see Equation 124). The corrected mass flow rate, on the other hand, cannot increase further, because the effects of the inlet gas pressure and temperature are eliminated in it. This is shown by the following rearrangement of Equation 125

$$\dot{m}_{0_corr_crit} = \sqrt{2c_p \left[1 - \beta_{crit}^{\frac{\gamma-1}{\gamma}} \right]} A_n \frac{1}{r} \beta_{crit}^{\frac{1}{\gamma}} \frac{p_{ref}}{\sqrt{T_{ref}}} \quad (127)$$

where r [J/(kg·K)] is the specific gas constant (the inlet gas density is no longer part of the formula). The relationship between the corrected mass flow rate through an ideal nozzle and the expansion ratio is visualized in Figure 70.

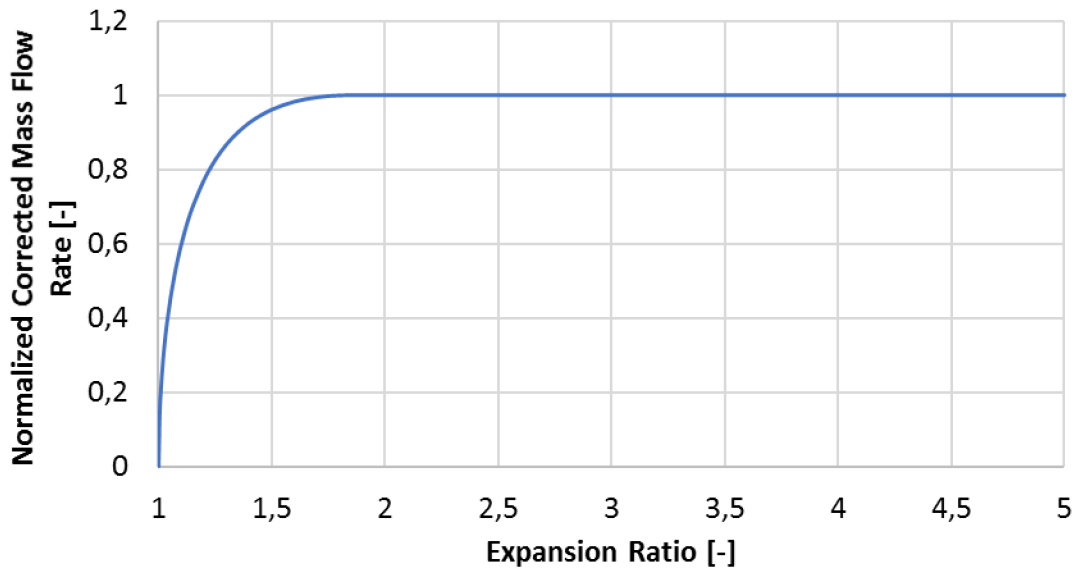


Figure 70: Corrected mass flow rate through the ideal nozzle

The fact that a real turbine cannot be modelled as the ideal nozzle has two major implications. First, a real turbine is choked at a different expansion ratio. Second, the corrected mass flow rate is affected by the centrifugal force and decreases with the spinning speed at a constant expansion ratio. The latter effect is, however, negated at zero turbine speed.

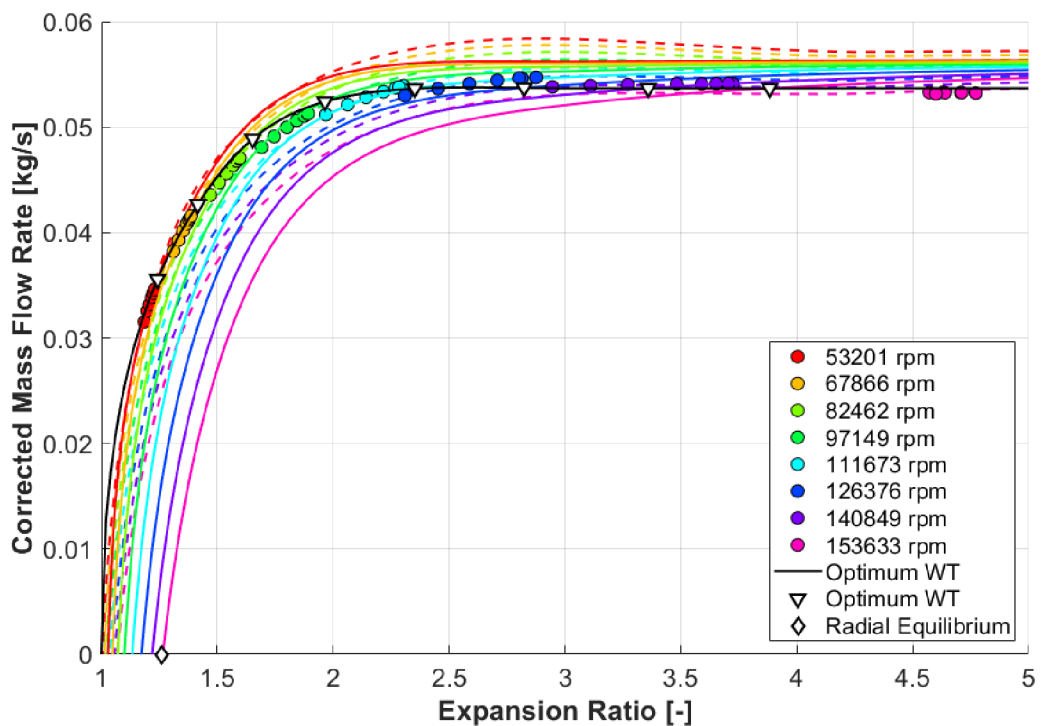


Figure 71: Fully extrapolated corrected mass flow rate map with non-decreasing optimum corrected mass flow rate (full lines) vs. the baseline fit (dashed)

Because the corrected mass flow rate at zero turbine speed is proportional to the optimum corrected mass flow rate (see Equation 105), it can be concluded that the

optimum corrected mass flow rate must be non-decreasing with respect to expansion ratio. Once this condition is implemented in the fitting algorithm, the fully extrapolated corrected mass flow rate map shown in Figure 71 is obtained. At the same time, however, the input data points at the highest speed line are no longer fitted. Although the optimum corrected mass flow rate no longer increases above the expansion ratio at choke, the optimum corrected turbine speed does, which is in alignment with the linear shape of the optimum BSR function (see Figures 32 & 76). Therefore, every speed line must cross the optimum corrected mass flow rate at certain expansion ratio, which means that the corrected mass flow rate at every non-zero speed line must be monotonically increasing with respect to expansion ratio. However, this behaviour is in contradiction to the measurement. Furthermore, if the theory of radial equilibrium were assumed to approximate the centrifugal effect at non-zero mass flow rates, it would imply that the offset with respect to expansion ratio is independent of the turbine inlet pressure (see Equation 122) and all speed lines should be parallel at choke. The only way all these constraints can be satisfied at the same time is by keeping the optimum corrected speed constant above the expansion ratio at choke.

4.3 Optimum Corrected Speed Limitation

Based on the findings introduced in Chapter 4.2, the optimum corrected speed should remain constant above the expansion ratio at choke to enable proper fitting of the corrected mass flow rate. This means that the optimum blade speed ratio no longer depends on expansion ratio under the conditions of choke, because the corresponding isentropic spouting velocity is limited (see Equation 45). Therefore, the topology of the affected characteristic function of the turbine performance model must be updated. For this purpose, a piece-wise polynomial is a convenient solution (see Figure 72).

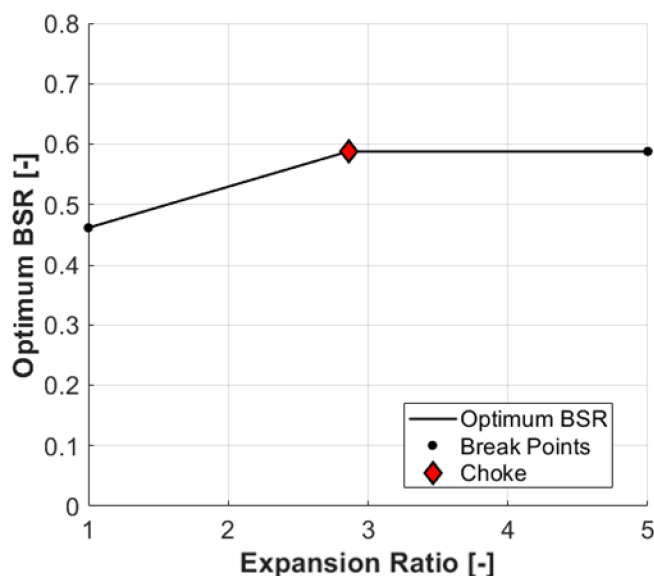


Figure 72: Optimum blade speed ratio spline with the limitation at choke

Also, the blade speed ratio at every operating point of the map must be calculated respecting the isentropic spouting velocity limit too. On the contrary, normalized blade speed ratio is independent of the isentropic spouting velocity and can be determined simply as the ratio of the actual and optimum corrected speeds (see Equation 98)

$$BSR_{norm} = \frac{BSR}{BSR_{opt}} = \frac{\frac{u}{c_0}}{\frac{u_{opt}}{c_0}} = \frac{NT}{NT_{opt}} \quad (128)$$

Turbine operating points of the same speed line are associated with the same normalized blade speed ratio under the conditions of choke. Furthermore, the maximum turbine efficiency is defined relative to the corrected speed in the standard algorithm introduced in Chapter 1.1.10 (see also Chapter 2.1.3). This would produce a constant maximum efficiency at choke. To interpret such a behaviour, it is convenient to take a closer look at the loss mechanisms in a turbine stage.

At choke, it is assumed that the wheel-inlet flow velocity and the absolute flow angle (in stationary frame of reference) are independent of expansion ratio. Therefore, it can be concluded that the highest efficiency is achieved at such a wheel circumferential speed, which results in the most convenient relative flow angle at the leading edge of the turbine blades (see Figure 3). On the one hand, this concept would support the idea of a constant optimum corrected speed at choke, while on the other hand there are further loss mechanisms, which must be considered too.

Most importantly, certain loss is always related to the velocity and density of the wheel exiting gas, which take away otherwise useful kinetic energy. Although the fluid cannot accelerate beyond the speed of sound in and upstream of the critical cross section, it can do so in the downstream channel provided its cross-section area is larger. In such a case, the working gas can either finish the expansion before exiting the turbine wheel, or it can expand further in the outlet diffuser. Based on the specific turbine stage geometry, this process is related to a bigger or a smaller overall efficiency loss.

Based on the above analysis, it can be concluded that the idea of a constant optimum corrected speed at choke is feasible, but the maximum turbine efficiency must remain variable with expansion ratio. This can be achieved by making the spline a function of expansion ratio directly. Although the optimum corrected mass flow rate should stay constant at choke, it is beneficial to be defined relative to the isentropic spouting velocity, since a strong correlation is expected there (see Figure 73). Another advantage of this approach is that the relationship between the isentropic spouting velocity and expansion ratio involves a square root, so that the output is tangent to the vertical for a zero-valued argument (with respect to the expansion ratio). That is very important, because the curve of optimum corrected mass flow rate must be vertical at the intercept with the expansion ratio axis (at $PRT = 1$, see Figure 71). This process can be interpreted as a transformation of coordinates.

It needs to be emphasized that the expansion ratio at choke is unknown in the beginning of the fitting process and must be obtained by optimization. An assumption that the optimum corrected mass flow rate is tangent to the horizontal at choke determines the required topology of the corresponding fitting function. The initial spline is defined by two end-points and two end-slopes. The first end-point is placed in the origin of coordinates and the second end-slope is set to zero (horizontal tangency). The first end-slope, the isentropic spouting velocity at choke and the relative corrected mass flow rate at choke are obtained using the simplex method, the objective of which is to minimize the average squared deviation from the measured data (least squares fitting).

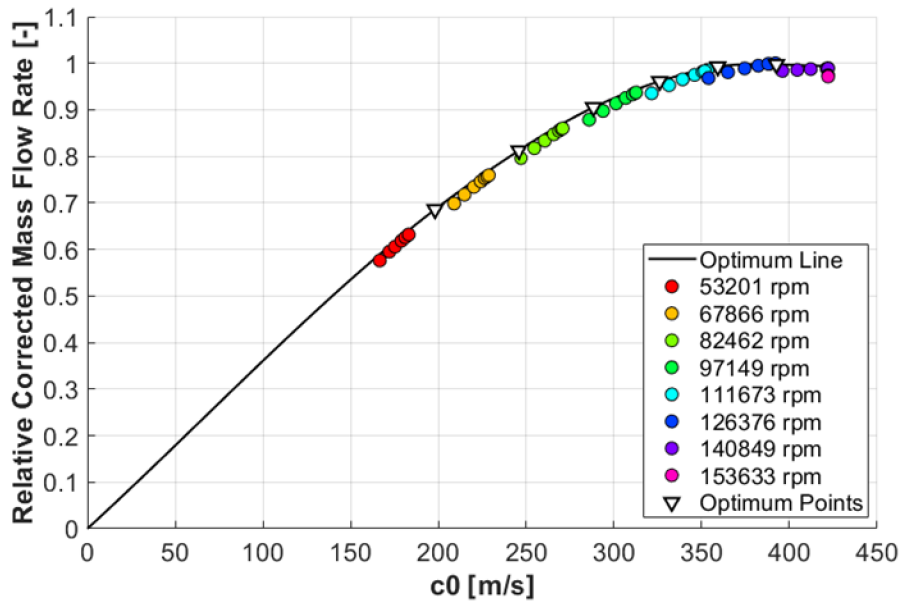


Figure 73: Optimum corrected mass flow rate as a function of isentropic spouting velocity (c_0)

As an important consequence, there is no optimum expansion ratio associated with the speed lines above the choke speed limit, so they cannot intersect with the maximum efficiency curve (see Figure 74).

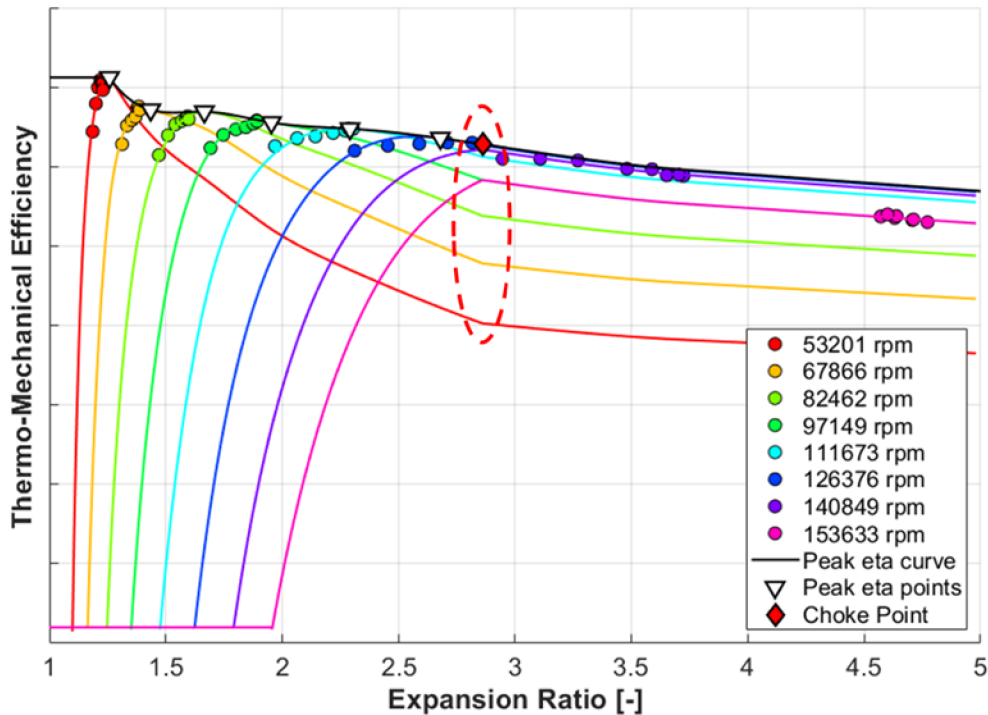


Figure 74: Fully extrapolated efficiency map with a sharp limitation of the optimum BSR

A simple limitation of the optimum blade speed ratio results in sharp bends of speed lines at the choke expansion ratio (see Figure 74). Therefore, the transition to the choke region must be made smooth. The easiest way is to split the optimum blade speed ratio curve in three intervals that a piece-wise polynomial is defined on.

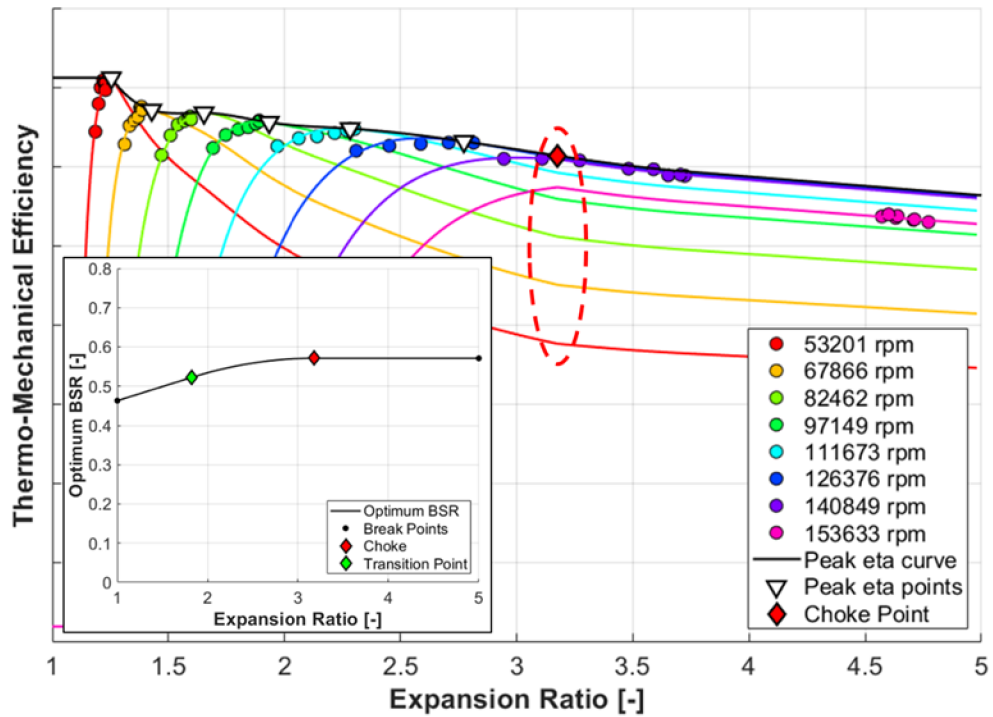


Figure 75: Extrapolated efficiency map with a smooth limitation of the optimum BSR

In Figure 75 it is shown that even a smoothed out optimum BSR function is no guarantee for smooth speed lines in the fully extrapolated efficiency map.

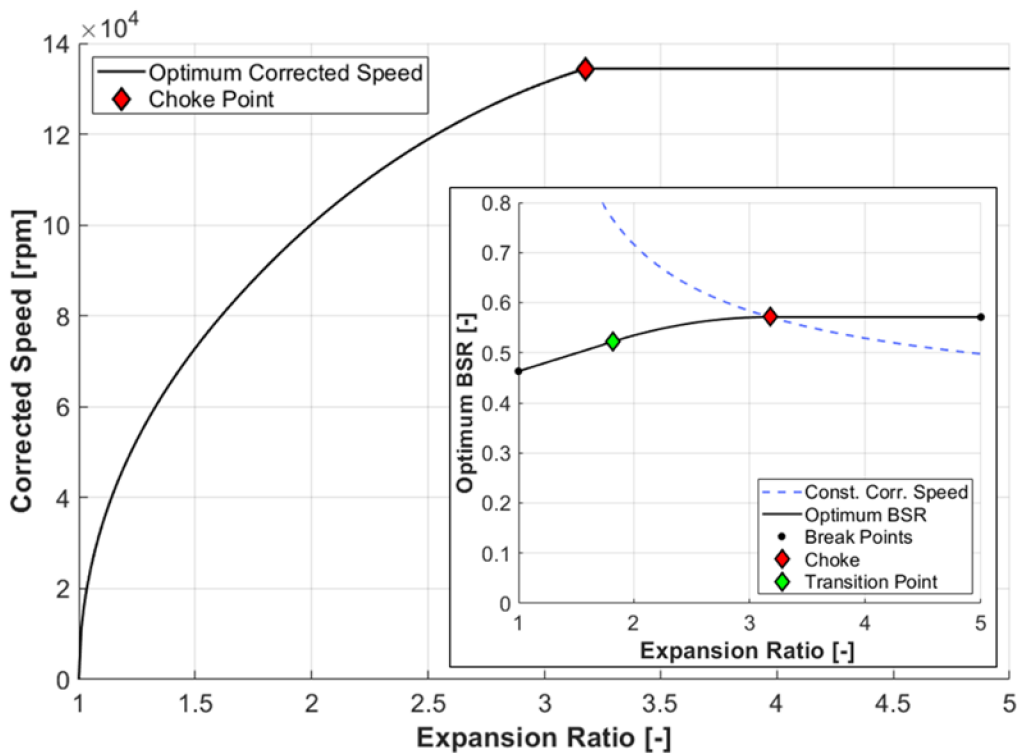


Figure 76: Optimum corrected speed for the smooth limitation of the optimum BSR

To avoid the sharp changes in normalized efficiency, there must be no sharp changes in the normalized BSR (see Equation 128). Therefore, the optimum BSR function must be

tangent to the curve of constant corrected speed at choke (see Figure 76). Nevertheless, the optimum *BSR* must remain constant at the expansion ratios above the choke point (see Figure 77).

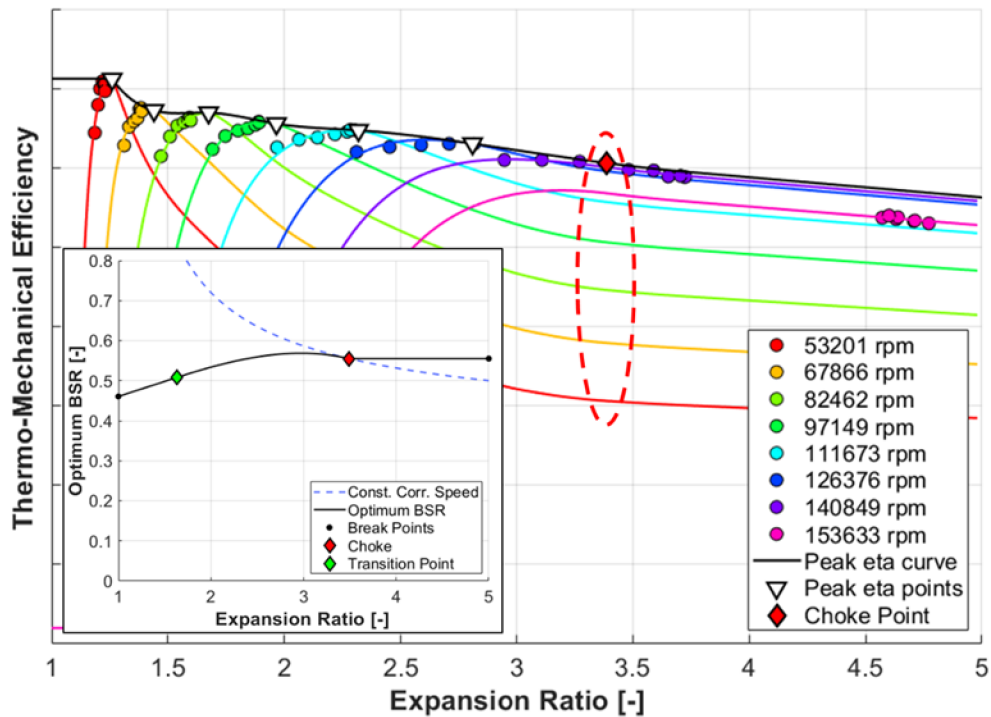


Figure 77: Fully extrapolated efficiency map with a tangential limitation of the opt. BSR

The impact on the corrected mass flow rate extrapolation can be assessed in Figure 78.

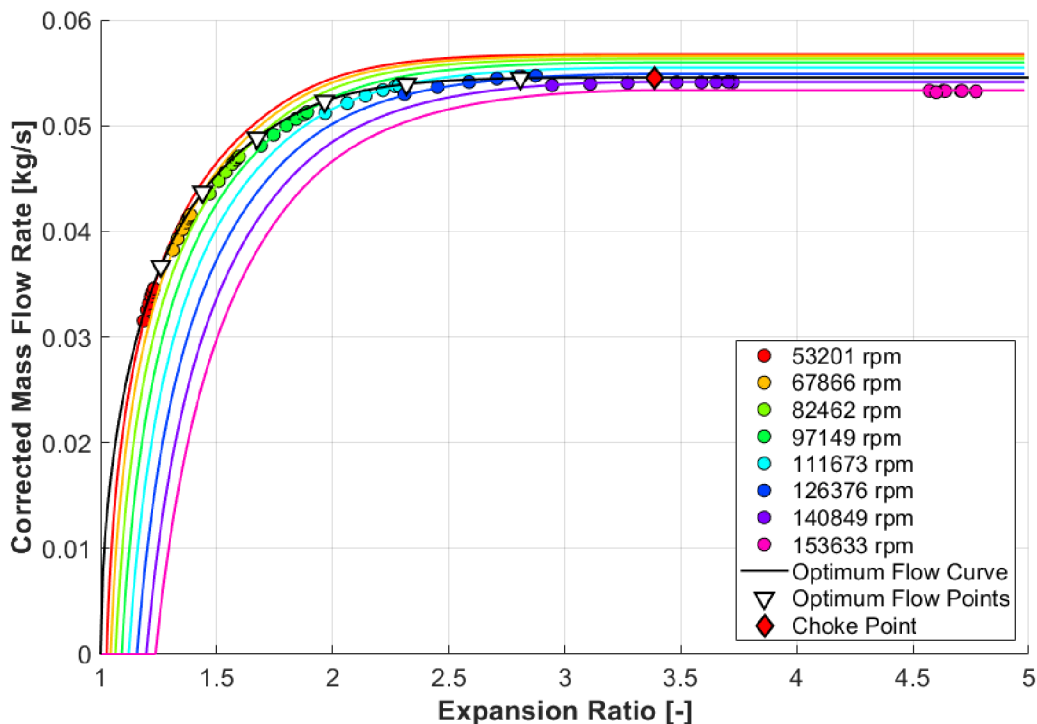


Figure 78: Fully extrapolated mass flow rate map with the tangential limitation of the optimum BSR

It has been confirmed that the measured data points can be reasonably fitted using the algorithm with the limited optimum corrected speed. Furthermore, the fully extrapolated corrected mass flow rate map meets the requirements identified in Chapter 4.2 (see Figure 78).

4.4 Fit Quality

After the sample turbine map obtained by a hot gas stand measurement is fitted, the quality of the new performance model can be evaluated. The deviations of the efficiency and the corrected mass flow rate at each operating point are evaluated to enable the calculation of the standard statistics (see Table 8).

Table 8: Statistics of the sample turbine map fit quality (the new algorithm used)

	Efficiency	Corrected mass flow rate
Minimum error	-1.04%	-0.29%
Maximum error	1.13%	0.40%
Mean error	-0.04%	0.01%
Median error	0.00%	-0.02%
Mean absolute error	0.31%	0.13%
MSE	0.18	0.03
RMSE	0.43%	0.16%

Compared to the initial non-optimized fitting of the sample turbine map (see Table 2), the new algorithm enabled the reduction of the efficiency root-mean-square error from 1.22% to 0.43% and from 0.58% to 0.16% for the corrected mass flow rate. The distribution of error size is displayed in Figure 79.

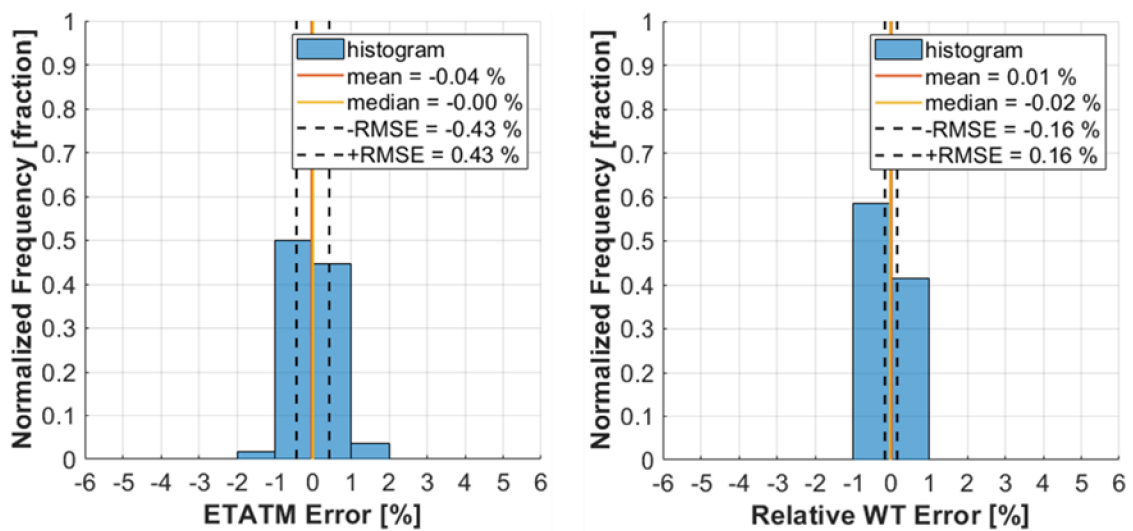


Figure 79: Histograms of fit error size for the efficiency (left) and the corrected mass flow rate (right)

It can be concluded that the measured efficiency is noisier than the corrected mass flow rate. Also, a more detailed view at the error at each operating point is provided in Figure 80, where it is made possible to distinguish between each speed line.

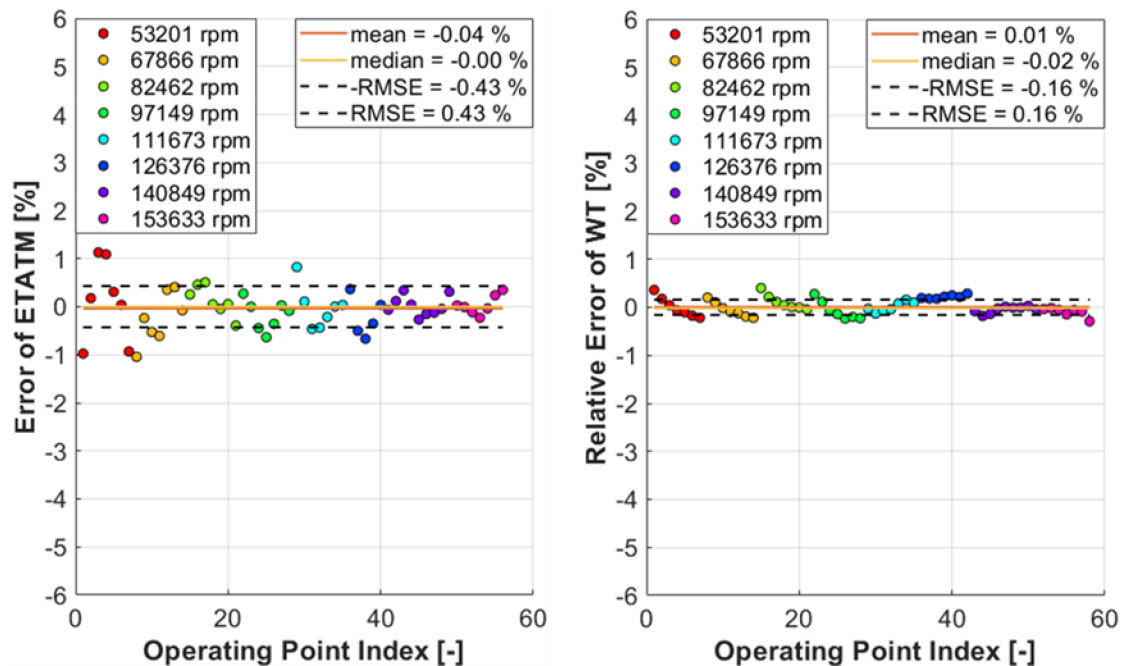


Figure 80: Fit error size as a function of data point index for the efficiency (left) and the corrected mass flow rate (right)

The biggest uncertainty is related to the lowest speed lines (see Figure 80), which is a similar conclusion as in the case of the initial fit (see Chapter 2.3.1). Nevertheless, almost all operating points deviate by less than one percentage point on efficiency and by less than zero-point-four percent on corrected mass flow rate, which is a very good fit.

4.5 Remarks on Implementation

The new turbine fitting algorithm is initialized by the identification of speed lines and the operating points with the highest efficiency in the input data (see Chapter 2.1.1). The five fitting functions model the same variables as in the baseline method, but the way they are defined is different. First, the maximum efficiency and the optimum corrected mass flow rate are functions of isentropic spouting velocity. The latter has a topology adjusted according to the theory of choke with the critical expansion ratio determined by optimization (see Chapter 4.3). The optimum BSR is initially fitted by a line and transformed into a spline after the critical expansion ratio is introduced. The linear part, nevertheless, retains its initial slope and the intersection with the y-axis (see Figure 77). Then, the normalized efficiency and mass flow rate are fitted in the standard way, except that the theory of radial equilibrium is accounted for with the latter (see Chapter 4.1). Optimization is applied to find the best properties of the characteristic functions, such that the minimum mean square error of the efficiency and the corrected mass flow rate is obtained. The complete process is iterative as described in Chapter 3.4. In the new algorithm, however, each main step consists of five successive optimization loops.

Maximum efficiency spline

The process of maximum efficiency spline optimization is described in Chapter 3.2. With the new fitting algorithm, no optimum points are linked to the speed lines above the corrected speed at choke, but the highest-expansion-ratio operating point at each speed line can be used to substitute the missing spline nodes. Further, a linear extrapolation is applied to cover the full range of expansion ratio. Only in the case the maximum efficiency spline would have negative slope at its lower end, a flat extrapolation is used to avoid the extension above one (see Figure 77).

Lower end-point of the optimum BSR spline

The three parts of the optimum *BSR* spline are identified in Figure 81. The slope of the linear piece is determined by the key-points A and B, while the optimum *BSR* at the expansion ratio one (the point A) is the value to be optimized. The y-coordinate of the key-point B is defined by the optimum *BSR* at choke, which can be determined based on the expansion ratio and the optimum corrected speed at choke. In the initial iteration step, the expansion ratio (x-coordinate) at the second key-point is equal to the one at choke. Later, it is determined by an independent optimization process.

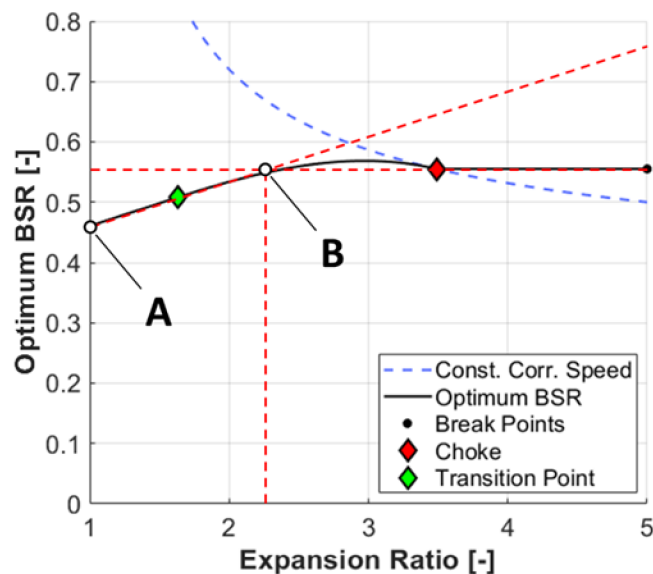


Figure 81: Optimum blade speed ratio spline

Choke point

Adjustment of the expansion ratio at choke has impact on the optimum *BSR* spline and the optimum relative corrected mass flow rate spline. The optimization process involves searching for both the expansion ratio and the optimum corrected speed at choke, which are translated into the blade speed ratio at choke. Therefore, the optimum *BSR* spline must be updated, but its linear part remains unaffected (the line connecting the point A and the transition point in Figure 81). The control point B is newly defined as a cross section between an extended linear part starting in the point A and a constant *BSR* line passing through the choke point. Since the adjustment of the optimum corrected speed at choke impacts the high-end corrected mass flow rate fit, the relative corrected mass flow rate at choke must be part of the optimization process. Its new

value is implemented in the corresponding spline in such a way that only the last piece is affected. The current algorithm uses only a subset of the optimum operating points linked to each speed line to define the nodes. By selecting the first four optimum points, where the expansion ratio is lower than two, it is safeguarded that the optimum relative corrected mass flow rate spline is non-decreasing (see Figures 72 & 78).

Control point B of the optimum BSR spline

To make sure the extended linear piece (the red dashed line in Figure 81) does not fall below the *BSR* at choke at the corresponding expansion ratio, a constrained one-dimensional optimization is applied (see Chapter 1.4.2). The x-coordinate of the control point B can vary between the expansion ratio two and the one at choke, while the y-coordinate is kept at the choke *BSR* level. By this, the slope of the linear piece is updated (the control point A remains unchanged) and the coordinates of the transition point are determined as the mid-point of the line segment AB.

Optimum relative corrected mass flow rate

The spline is defined on the interval delimited by the origin of the coordinate system from the left and the choke point from the right. The breakpoints correspond to the optimum operating points at each speed line. However, above the isentropic spouting velocity at the expansion ratio two, no more breakpoints are included to make sure the transition to choke is non-decreasing (see Figure 73).

4.6 Robustness Check

The new turbine map fitting algorithm proved to be reasonable at modelling the sample turbine stage performance, the source data of which was acquired on a hot gas stand.

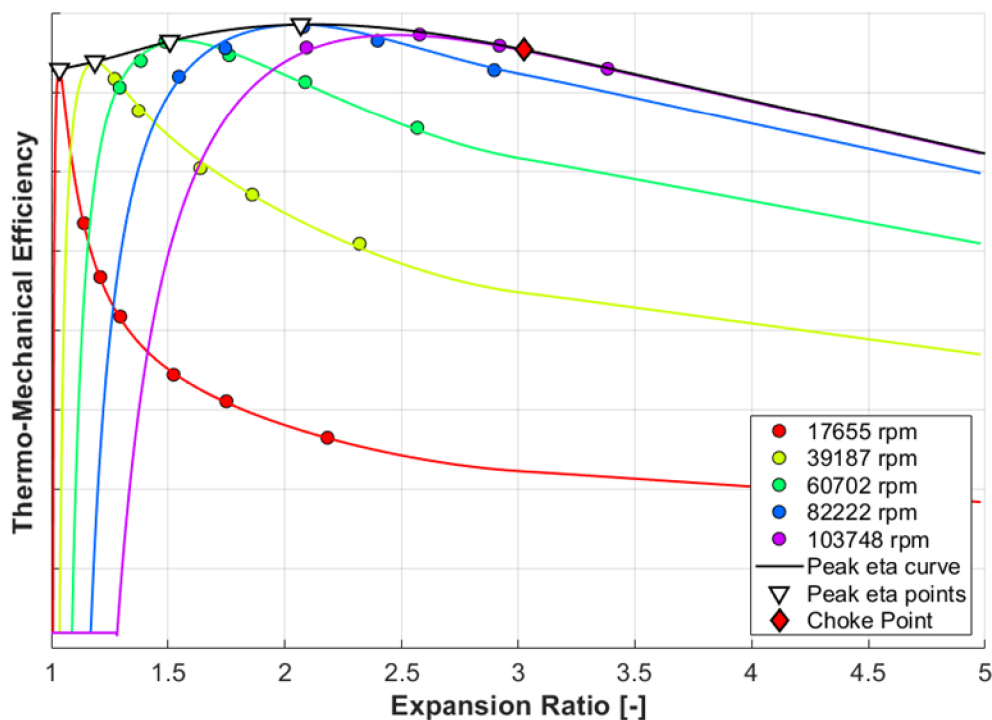


Figure 82: Dyno data fitted using the new algorithm (fully extrapolated efficiency map)

To check the robustness of the method, the same dyno map was fitted as in the case of the baseline algorithm (see Chapter 2.3.3). Based on the assessment of the fully extrapolated efficiency map, it can be concluded that a good fit quality is achieved with the dyno map too (see Figure 82, the root-mean-square error is 0.38%). Furthermore, the new algorithm demonstrated to be capable of *predicting the maximum turbine efficiency* in areas, where sub-optimal measured data points only are available (see the first two speed lines in Figure 82). This is made possible by the application of optimization methods and the rule that all turbine operating points should lie on the same curve in the normalized efficiency versus normalized blade speed ratio diagram.

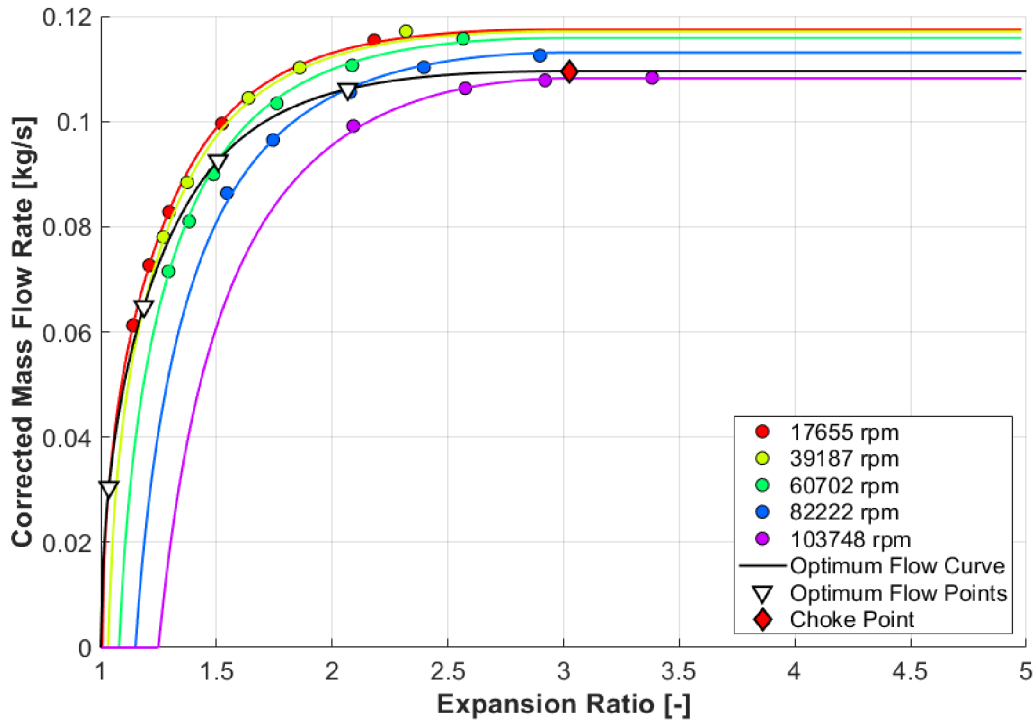


Figure 83: Fully extrapolated corrected mass flow rate map generated using the data obtained on a turbine dynamometer (fitting with the help of the new algorithm)

The extrapolated corrected mass flow rate map in Figure 83 shows a good agreement between the model and the input data too, although some points are deviated more than in the case of efficiency (the root-mean-square error is 0.59%).

All in all, the new turbine performance fitting algorithm proved to be effective at dealing with both the hot gas stand and dyno maps. Especially in the latter case, a huge fit quality improvement could be observed compared to the baseline algorithm, which did not use optimization (see Chapter 2.3.3).

5 APPLICATIONS OF FITTED TURBINE MAPS

A fitted turbine model makes it possible to interpolate or extrapolate the performance properties at any operating point within its domain of definition. This is particularly important in conjunction with engine thermodynamics simulations as explained in Chapter 1.1.9. Another big advantage, though, is the possibility to compare different turbine stages at equal operating conditions.

5.1 Map Database & Fitting Workflow

To compare multiple turbine stages at a time, the corresponding performance maps and the fitted models must be available to the application. Required data can be stored either as variables (e.g. using the .mat file) or in a database. The main difference is that a database system is equipped with built-in data management tools, which provide enhanced functionality. To the frequently used belong the searching, the filtering, the merging of related entries or the ordering according to selected parameters. On top of that, database systems include multi-access management, which makes it possible for multiple users to work with the same database file in the same time.

In this work, the SQLite 3 database was selected for its availability and an easy implementation in a MATLAB application (see [25]). It has a tabular structure, where each type of input is represented by one table (e.g. gas stand maps, dyno maps, fitted performance models). Within a table, variables are organized in columns, while the data related to each entry is stored at a row. In the user interface, the database content is listed to facilitate the selection of desired inputs (see the left-hand-side column in Figure 87).

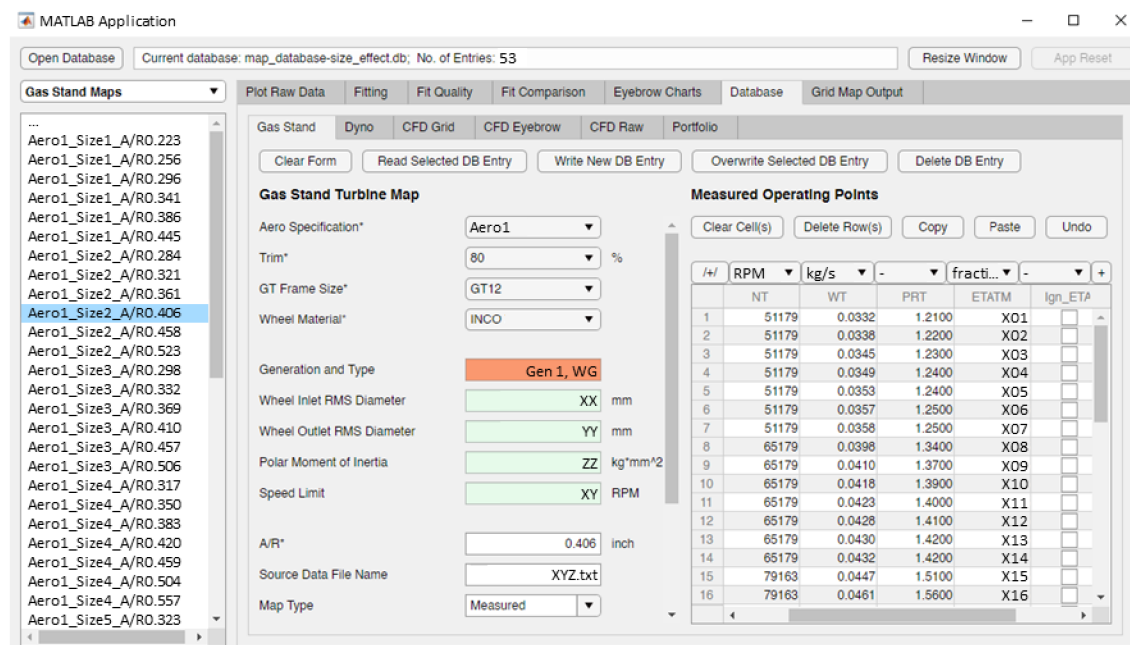


Figure 84: User interface for the database interactions related to gas stand maps

The developed application is equipped with a dedicated interface for a user-friendly creation of new database entries. In the case a measured map is needed to be entered,

the user must provide information required to identify the origin and the features of the related hardware. Then, measured operating points are inserted in a tabular format (see Figure 84). Once raw data is fed into the database, it can be fitted by a turbine performance model to enable all postprocessing features built in the application. The initiation of this process takes one click, but the quality of the output must be checked before saving (see Figure 85). In the case individual outlying points are identified, it should be considered that they might be measurement errors (especially if there is a clear misalignment with an overall trend). In such a situation, selected operating points can be ignored to avoid model distortion after a repeated fitting. This feature supports mouse picking, while the associated points are immediately marked in the database.

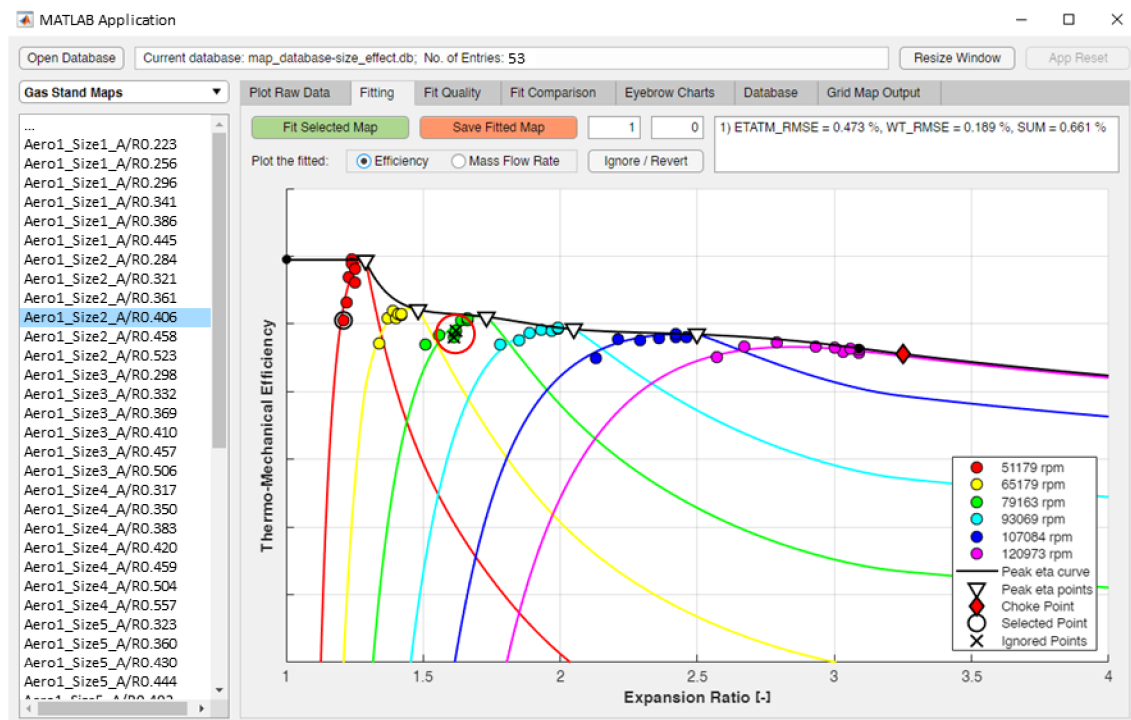


Figure 85: Initial fit quality assessment with the possibility to ignore outlying operating points (highlighted by the red circle)

The process of a gas stand map fitting takes about half a minute on a contemporary personal computer. However, additional time is needed to feed the raw measured data into the database (see Figure 84). Altogether, one measured map can be entered, fitted and saved in the database in a couple of minutes. That is ok, unless a large number of maps must be processed at once. Nevertheless, subsequent postprocessing operations are automated and require only the selection of desired database entries (e.g. to compare turbine efficiencies).

For the eventuality it is needed to apply a fitted turbine performance model outside of the developed application, an export function is integrated. The output is a fully extrapolated map in a tabular form, which can be copied and pasted in other software tools. The user can define the number of speed lines to be generated, as well as the number of operating points at each. Among the uses of this output is the simulation of a turbocharged combustion engine working cycle. In the case of the GT-SUITE, the so-called grid map format is used to import the data, see further in Chapter 5.5.

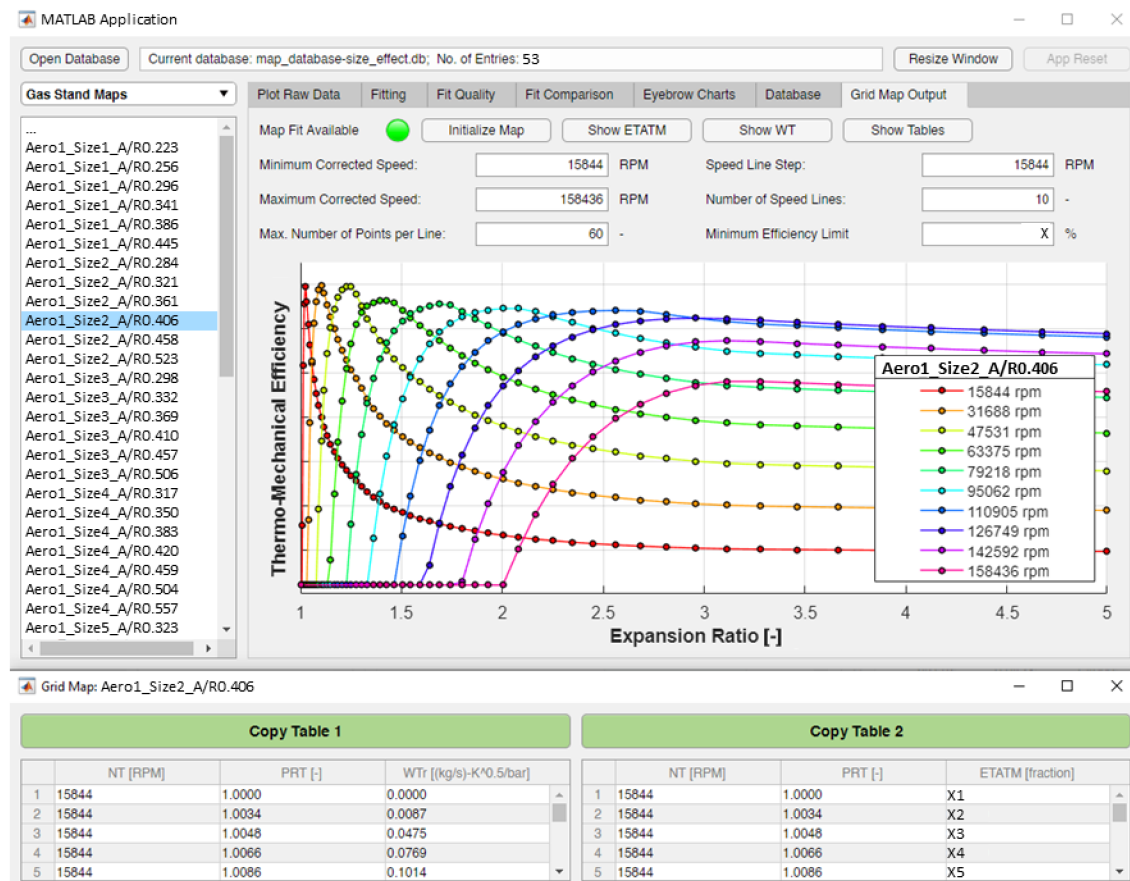


Figure 86: Exporting of a fully extrapolated turbine performance map

5.2 Comparison of Turbine Performance

To the standard methods of turbine stage aerodynamic adaptation to specific engine requirements belong the selection of the wheel size, the trim and the A/R parameter of the volute (see Chapter 1.1.2). The purpose of each feature is mainly to define the mass flow capacity (ordered from the most effective to the least effective), however there is certain impact on the efficiency pattern too. In a typical case, turbine wheel diameter is selected based on both the flow capacity requirement and the convenient speed matching with the compressor. Further, turbine trim is usually an inherent property of a specific blade design and cannot be easily changed (complete mechanical qualification would be required). Adaptation of the A/R parameter, on the other hand, can be done freely within certain range, which makes it the most frequently used method of turbine flow capacity fine-tuning. Therefore, the visualization of its implications on turbine performance is a commonly requested task.

The necessary first step is to gather a set of turbine maps of the same blade design and wheel diameter that cover certain range of A/R (see Figure 87). In the next phase, performance models are fitted to the measured data to enable all postprocessing features, which is possible only under the conditions an agile data management system is available. This requirement is addressed by the implementation of the SQLite 3 database, which proved to be advantageous in multiple ways (see [25]).

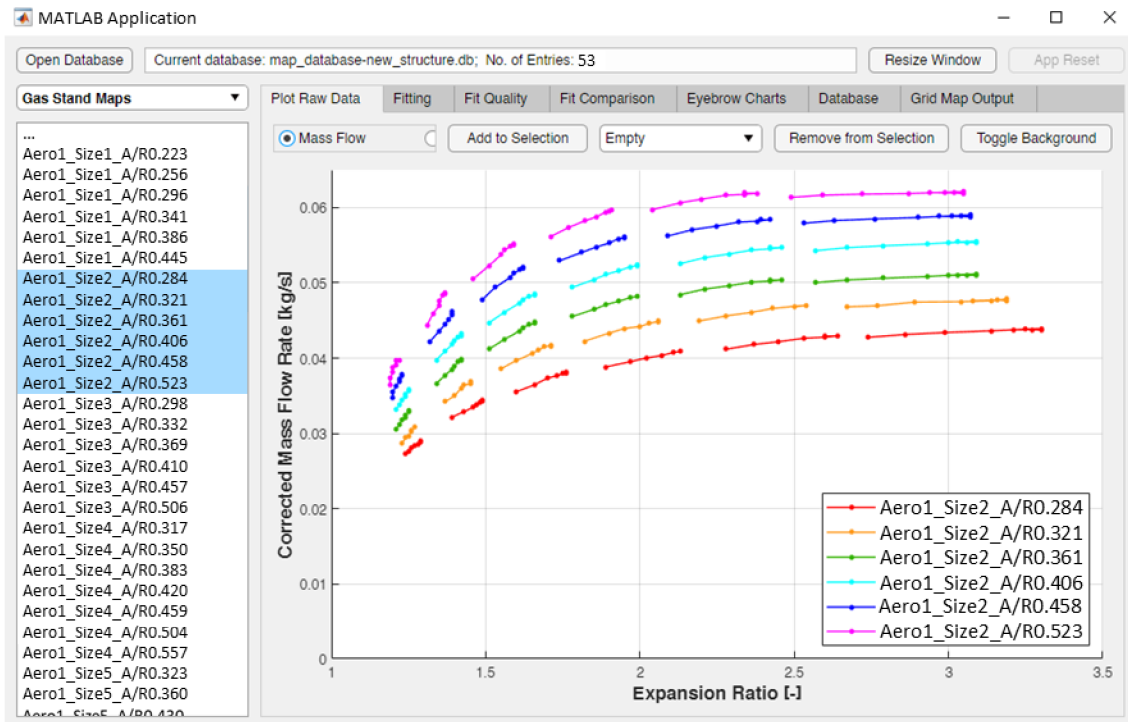


Figure 87: Raw corrected mass flow rate linked to the selected database entries

Plotting of raw corrected mass flow rate for a common range of A/R shows that the flow capacity of the largest option is roughly by a half bigger than the smallest (see Figure 87). The comparison of raw efficiency is less straightforward though (see Figure 88).

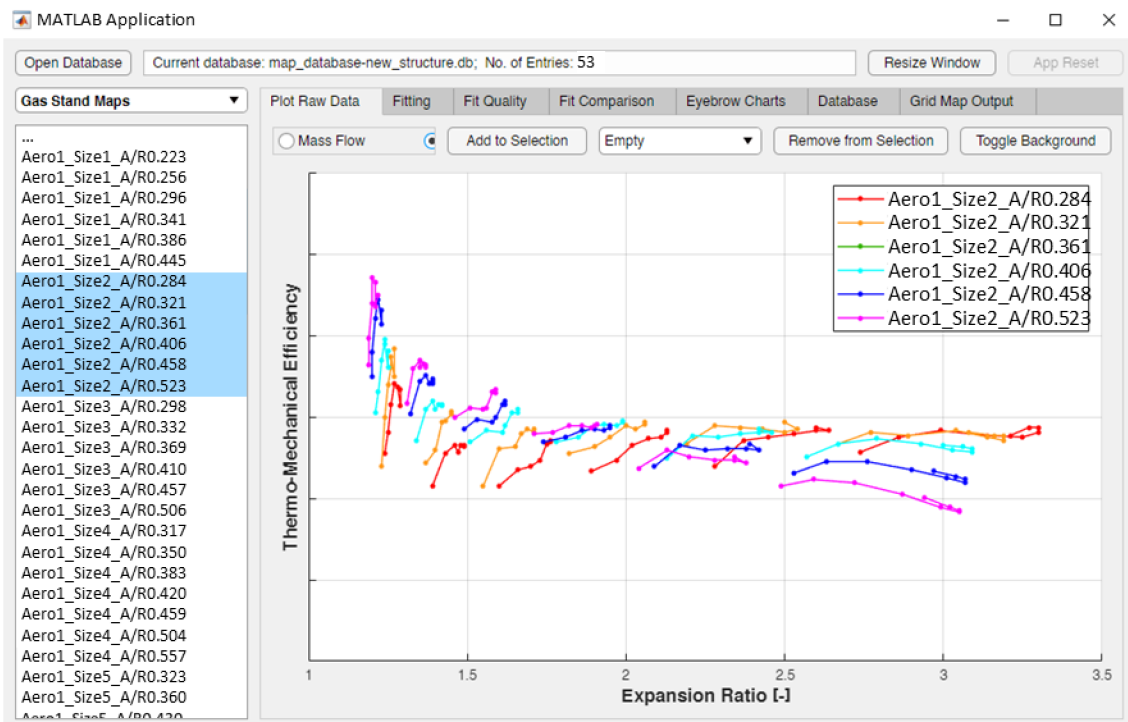


Figure 88: Raw efficiency linked to the selected database entries

Since the maximum-efficiency operating points are generally not included among measured data, it may be difficult to draw a clear conclusion about the performance

trade-offs between multiple turbine options. That is where fitting may help to better understand the overall trends provided the quality is sufficient for the required level of resolution. An advantage worth mentioning is that a turbine performance model inherently contains information about the location of the maximum-efficiency operating points, which makes it easy to plot.

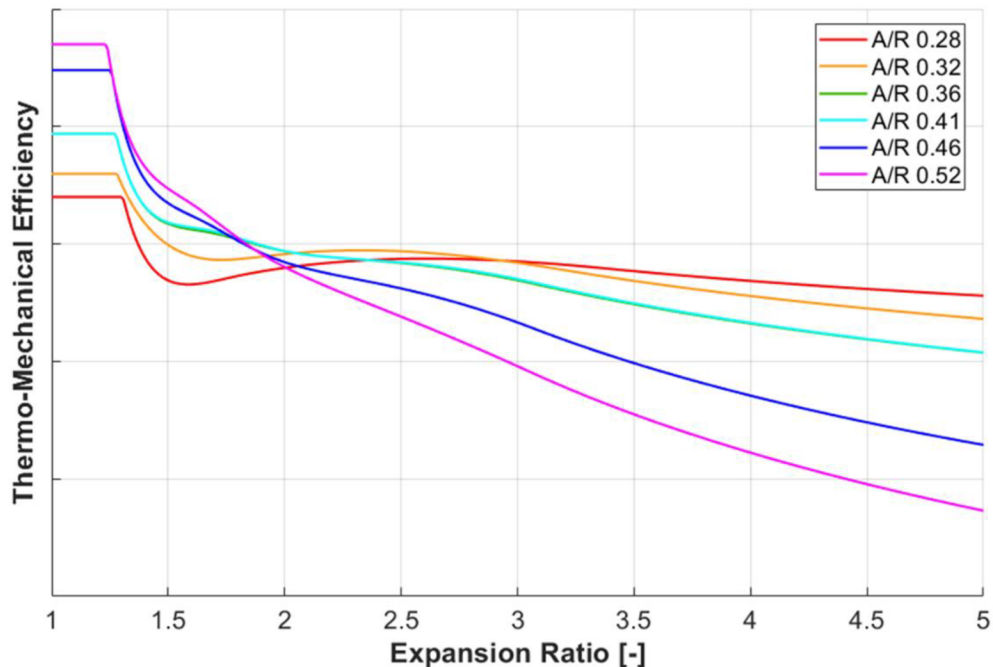


Figure 89: Fitted maximum efficiency vs. expansion ratio for a range of A/R

From the comparison in Figure 89 can be concluded that increasing value of A/R parameter results in tilting of the maximum-efficiency curves. While at low expansion ratios the highest maximum turbine efficiency can be achieved with the largest volute, the opposite is true at the high end. An interesting behaviour can be identified near the expansion ratio two, where the maximum turbine efficiency is almost independent of the A/R parameter.

Another clear trend, that can be identified, is a sudden increase of the maximum efficiency below the expansion ratio one point five. This is not a true behaviour of the turbine, but an implication of heat transfer that influences the measured compressor outlet temperature on a hot gas stand. The studied turbochargers are equipped with water cooling, but the coolant temperature is kept at ninety degrees Celsius to emulate on-engine conditions. That is higher than the compressed air temperature during low-speed mapping. Therefore, higher compressor outlet temperature is measured due to a heat inleak from the centre housing. As a result, the calculated compressor efficiency appears lower and the turbine efficiency determined from power balance with the compressor appears higher (see [19]).

Optimum corrected mass flow rate can be plotted over expansion ratio in a similar way to the maximum efficiency. In this case, the appearance of such a chart is very similar to the one showing the raw data (see Figures 87 and 90). Nevertheless, the constraints of the constant optimum corrected mass flow rate at high expansion ratios and the crossing of the origin of coordinates are well illustrated in it.

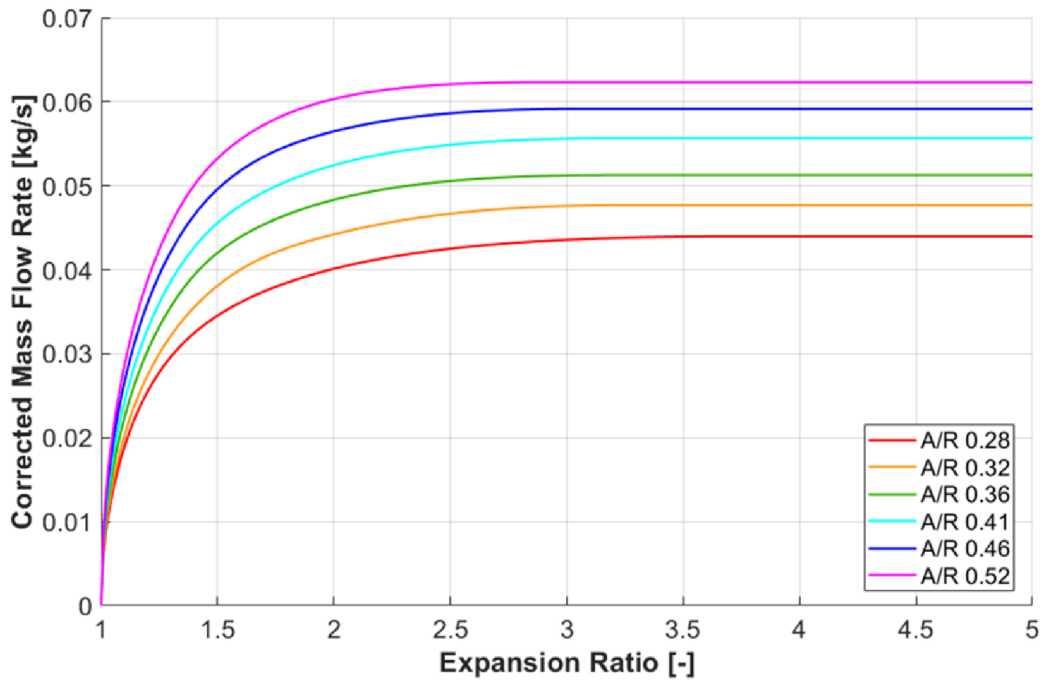


Figure 90: Optimum corrected mass flow rate vs. expansion ratio for a range of A/R

To the remaining functions constituting a turbine performance model along the optimum *BSR*, the normalized efficiency and the normalized mass flow rate. They are visualized for the same set of turbine maps like in the above charts (see Figure 91).

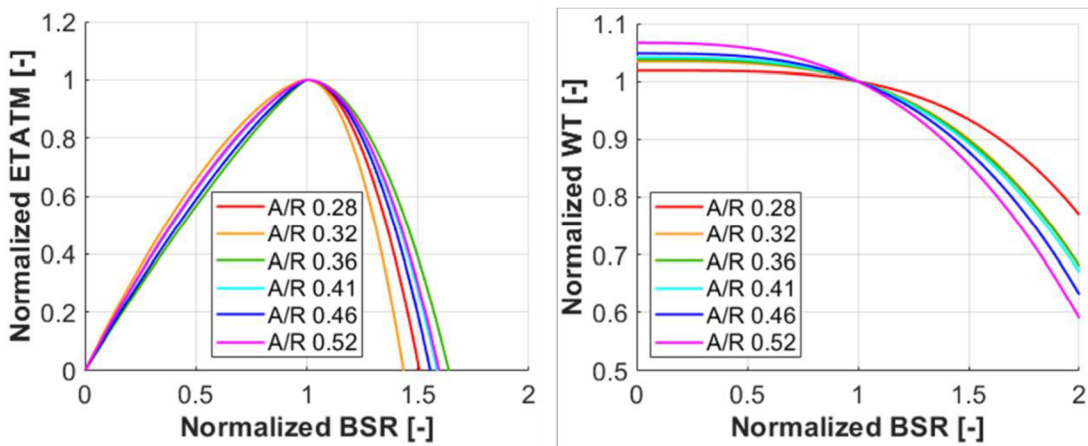


Figure 91: Normalized efficiency (left) and normalized mass flow rate (right) vs. normalized blade speed ratio for a range of A/R

The functions of normalized efficiency and normalized mass flow rate in Figure 91 show the important turbine behaviour at sub-optimal operating conditions. The flatter the normalized efficiency, the more robust is the turbine stage against variation of operating conditions (pulsation, speed match, altitude etc.). In the case of the normalized mass flow rate, a steeper relationship means a bigger variation of corrected mass flow rate with the spinning speed (i.e. stronger centrifugal effect).

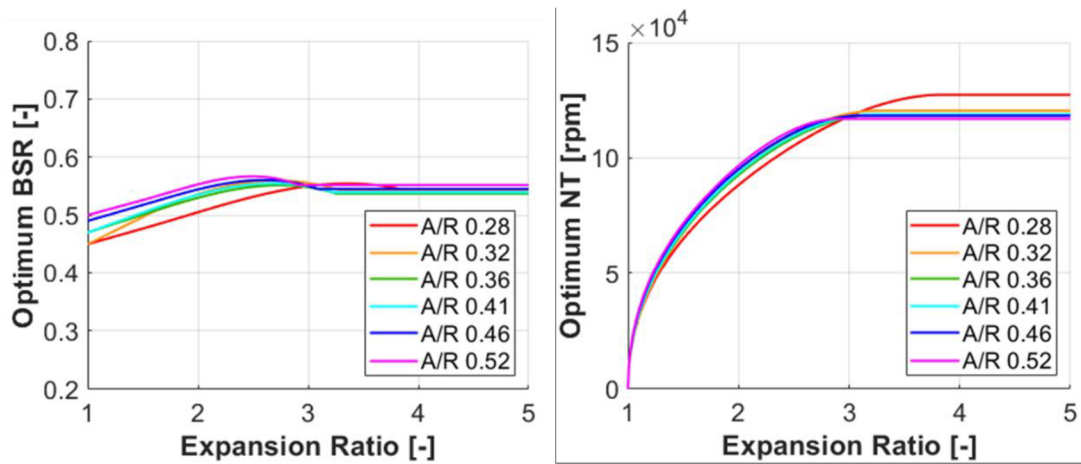


Figure 92: Optimum blade speed ratio (left) and optimum corrected speed (right) versus expansion ratio for a range of A/R

In some cases, however, it is desired to display these relationships in the physical scale (not normalized). For this purpose, a fixed expansion ratio must be selected.

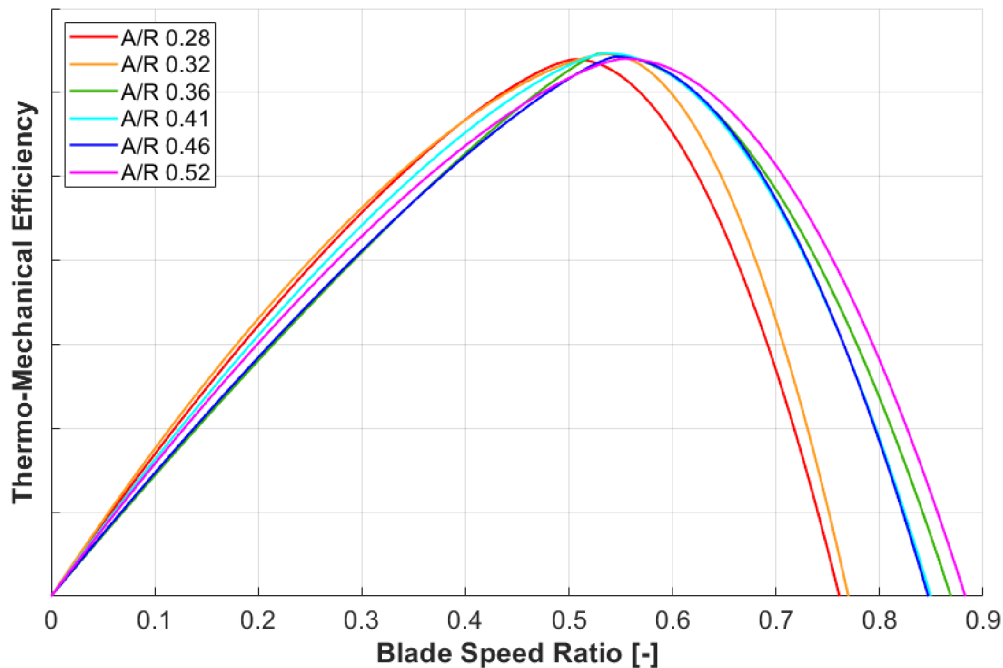


Figure 93: Efficiency vs. blade speed ratio at the expansion ratio two for a range of A/R

Although there is blade speed ratio on the x-axis in Figure 93, a constant expansion ratio causes that *BSR* is directly proportional to spinning speed (see Equation 46). Therefore, a lower *BSR* at the peak means the maximum efficiency would be achieved at lower spinning speed. Similar is the situation in the case of corrected mass flow rate (see Figure 94).

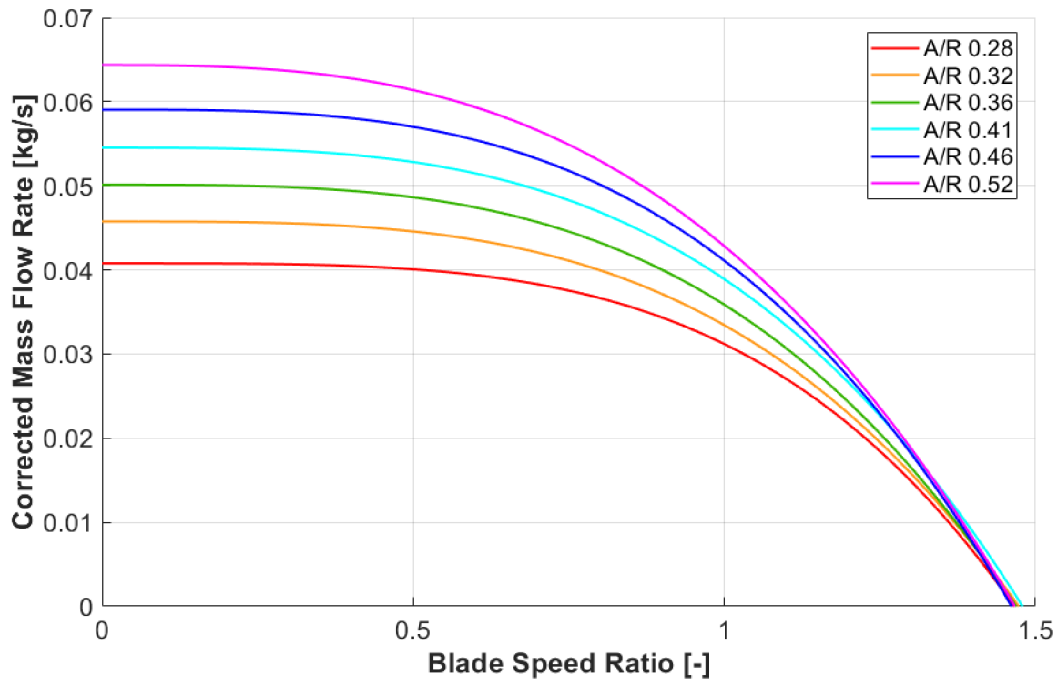


Figure 94: Optimum corrected mass flow rate vs. blade speed ratio at the expansion ratio two for a range of A/R

5.3 Compound Charts

Another common way to compare different turbine stages is by combining the efficiency and the corrected mass flow rate at the same operating conditions into a single chart (sometimes referred to as an “eyebrow chart”). In a typical case, the maximum efficiency is plotted against the optimum corrected mass flow rate at a constant expansion ratio for a set of maps distinguished by the A/R parameter (see Figure 95).

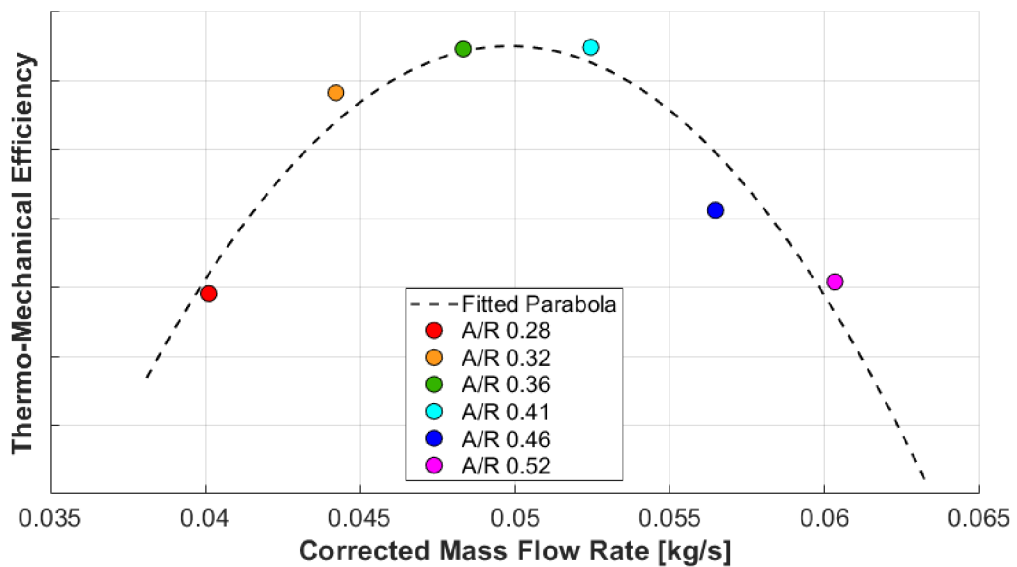


Figure 95: Max. efficiency vs. opt. corr. mass flow rate at PRT = 2 for a range of A/R

It is possible to generate a similar chart as in Figure 95, but extended by another dimension for the expansion ratio (see Figure 96).

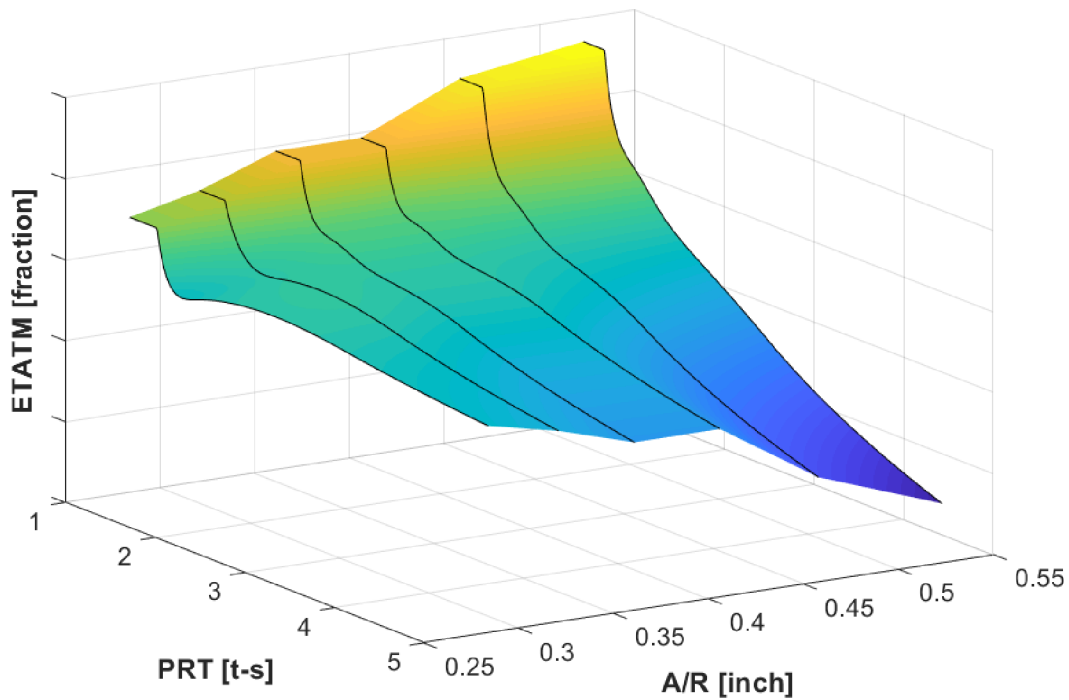


Figure 96: Maximum efficiency vs. expansion ratio vs. A/R parameter

The comparison of maximum efficiency curves for a range of A/R parameter in Figure 96 confirms that their slope decreases together with the A/R. The corresponding optimum corrected mass flow rate surface is displayed in Figure 97.

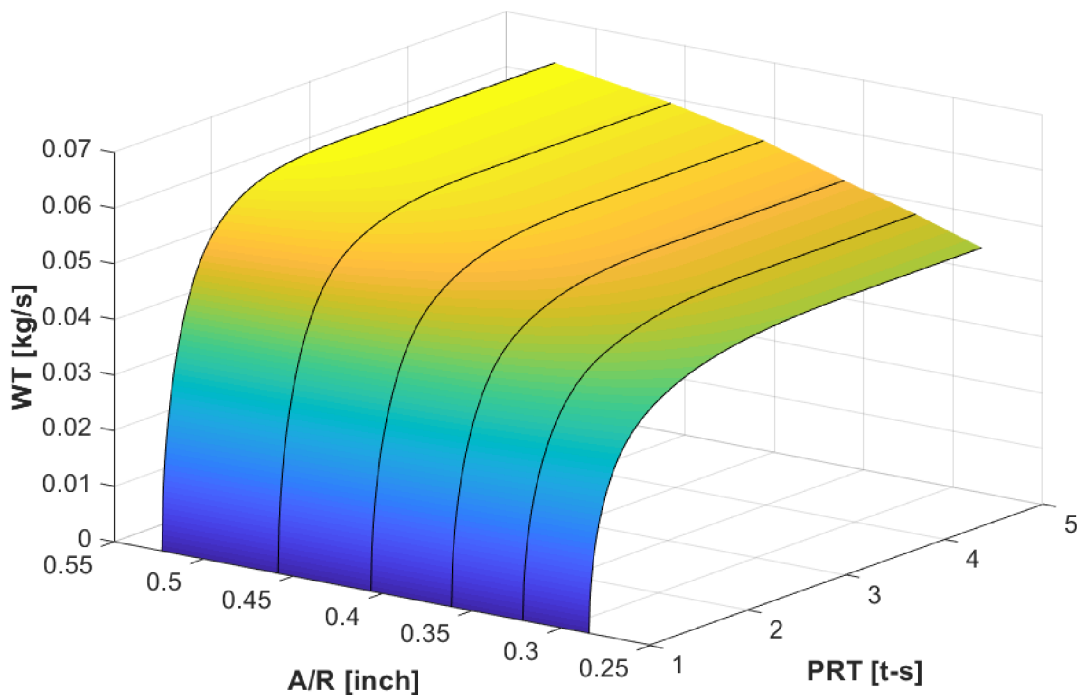


Figure 97: Optimum corrected mass flow rate vs. expansion ratio vs. A/R parameter

Figure 97 shows an almost linear relationship between the flow capacity and the A/R parameter. Also, the higher-positioned curves are notably sharper bent, which suggests an increasing effect of centrifugal forces on the mass flow rate with larger volutes.

5.4 Size Effect

After the relationship between the maximum turbine efficiency and the volute size has been resolved, the investigation can be extended by another important parameter, which is the wheel diameter. The product is sometimes referred to as the size effect.

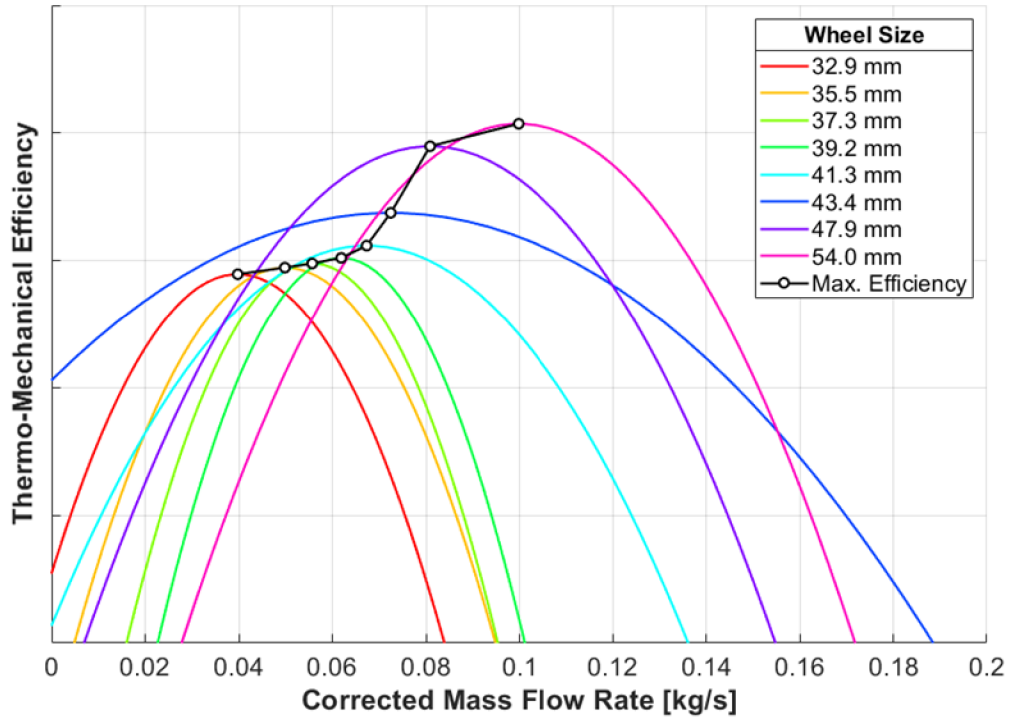


Figure 98: Composition of eyebrow charts generated at the expansion ratio two for a range of turbine sizes sharing the same wheel aerodynamic design

The above diagram was created with the help of 53 fitted turbine maps. It is possible to generate a similar chart for the optimum performance with the wheel size on the x-axis.

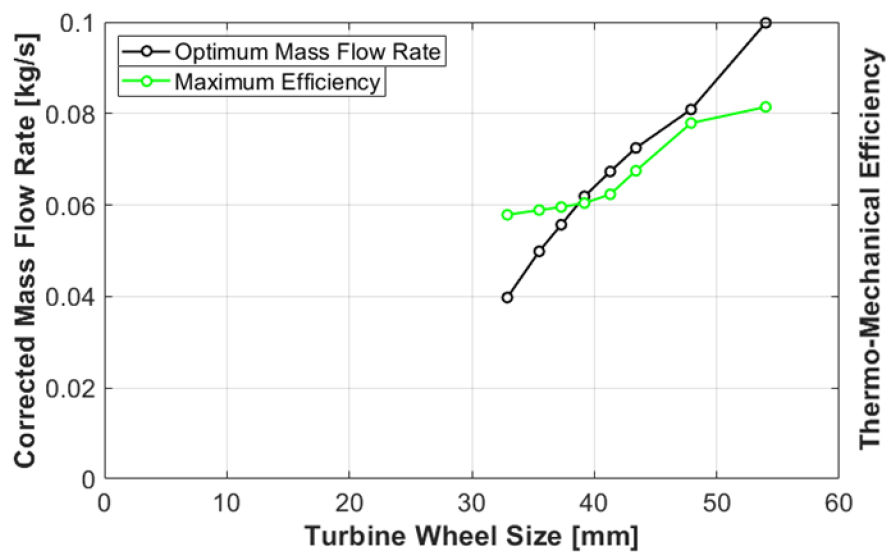


Figure 99: The optimum corrected mass flow rate and the maximum efficiency vs. the turbine wheel diameter at the expansion ratio two

5.5 Engine Simulation

The ultimate application of a turbine performance model is an engine performance simulation. In GT-SUITE™, which is a commonly used simulation tool, fitted turbine maps can be imported in the so-called *grid format*. It consists of the same data as a standard turbine map (corrected speed, expansion ratio, reduced mass flow rate and efficiency), but it is extrapolated to the full operating range (see Chapter 2.2). Thanks to that, the application can use this data to simply interpolate required turbine performance properties without the need to perform any further fitting.

To compare the impacts of a default (GT-SUITE) and the proposed fitting algorithms on engine performance, a 1.2 L three-cylinder engine model was selected. The example turbine stage studied in the previous chapters (35.5 mm wheel diameter) well matches to this engine and will continue to be used in the following paragraphs.

An important feature of the selected engine is that its low-end performance is limited by the available turbine power (wastegate closed). Therefore, any difference in the fitted turbine efficiencies is expected to have impact on the achievable break torque.

5.5.1 Steady-state performance with the gas stand map

For purpose of a steady state comparison, an engine simulation mapping the full load performance was selected. At these conditions, the throttle valve is fully opened and brake torque is controlled by the boost pressure. In the low-end region, the turbine is supplied by an insufficient exhaust gas mass flow rate, which results in the power deficit to drive the compressor and deliver the required boost pressure. Therefore, the maximum torque cannot be reached. At higher engine speeds, boost pressure is controlled by the wastegate (turbine by-pass regulation).

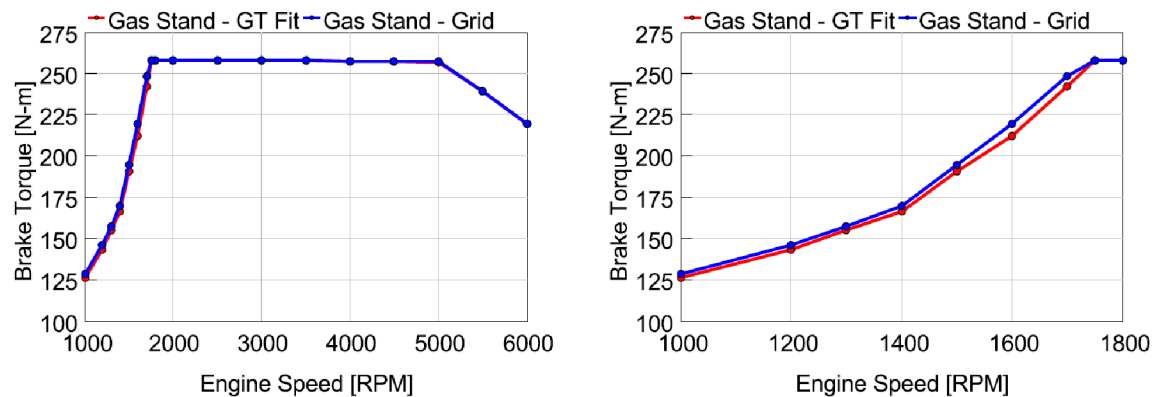


Figure 100: Full load simulation with the fitted turbine maps obtained by a hot gas stand measurement (red – the default fit, blue – the proposed algorithm)

The biggest difference in the full-load performance can be observed at 1600 rpm¹, where the default fit gives by 7 Nm lower brake torque compared to the proposed algorithm (see Figure 100). That corresponds to an approximately 3% difference, which can be evaluated as a good agreement between the two methods. Nevertheless, it is worth tracking back the root cause for the difference.

¹ The unit *rpm* stands for *revolutions per minute* (equivalent to *1/min*).

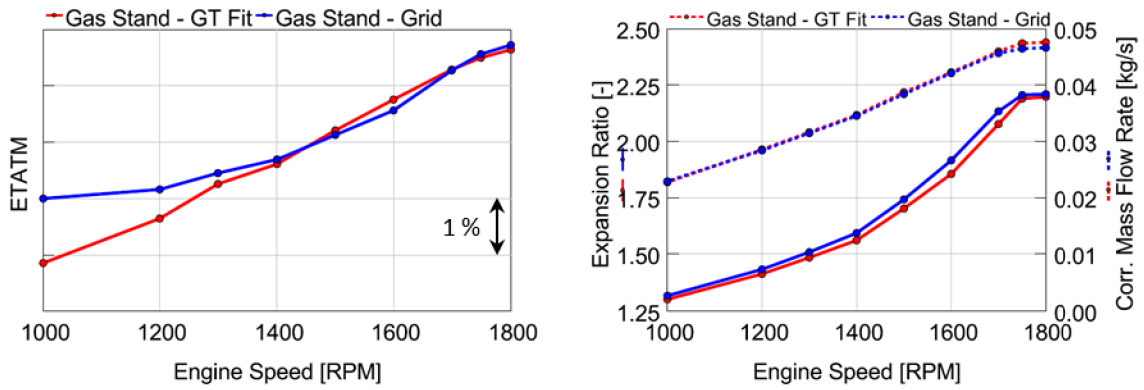


Figure 101: Turbine efficiency (ETATM), expansion ratio & corrected mass flow rate

Although the proposed fit yields a lower average efficiency (isentropic power weighted) at 1600 rpm, the expansion ratio is higher (see Figure 101). Corrected mass flow rate is almost the same though, which suggests there is a difference between the maps.

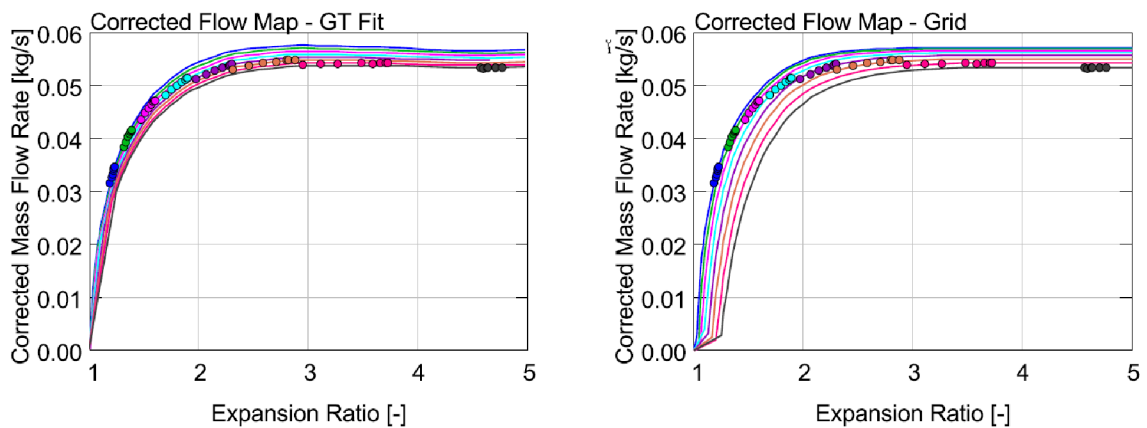


Figure 102: Comparison of the corrected mass flow rate maps generated using the default (left) and the proposed (right) algorithms

Corrected mass flow rate map with the default fit features condensed speed lines at low expansion ratios, where the proposed algorithm resolves the centrifugal force effect (see Chapter 4.1 & Figure 102). This must be evaluated over a complete engine cycle.

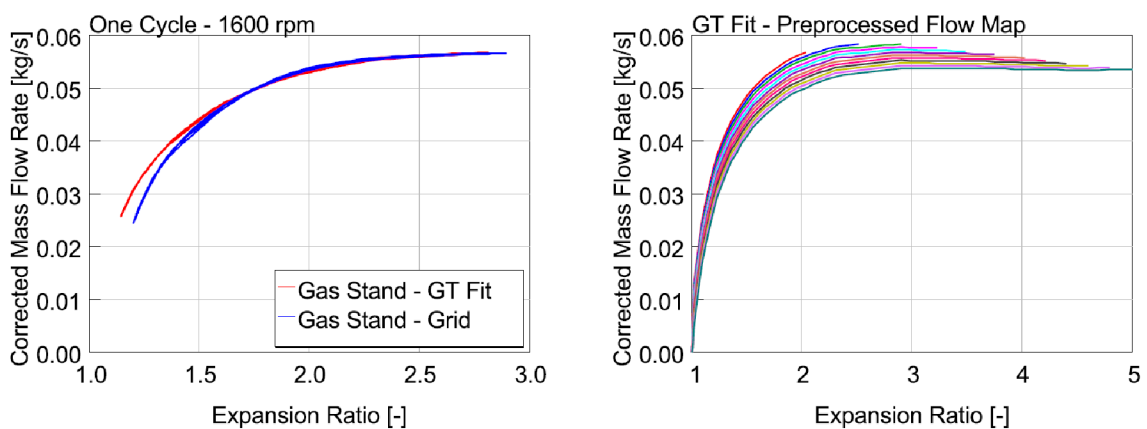


Figure 103: Instantaneous turbine operating points during one engine cycle (left) and the extrapolated mass flow map as per the default fit (right)

The analysis of instantaneous turbine operation confirms that the difference in average expansion ratio is related to the resolution of centrifugal forces effect (see Figure 103).

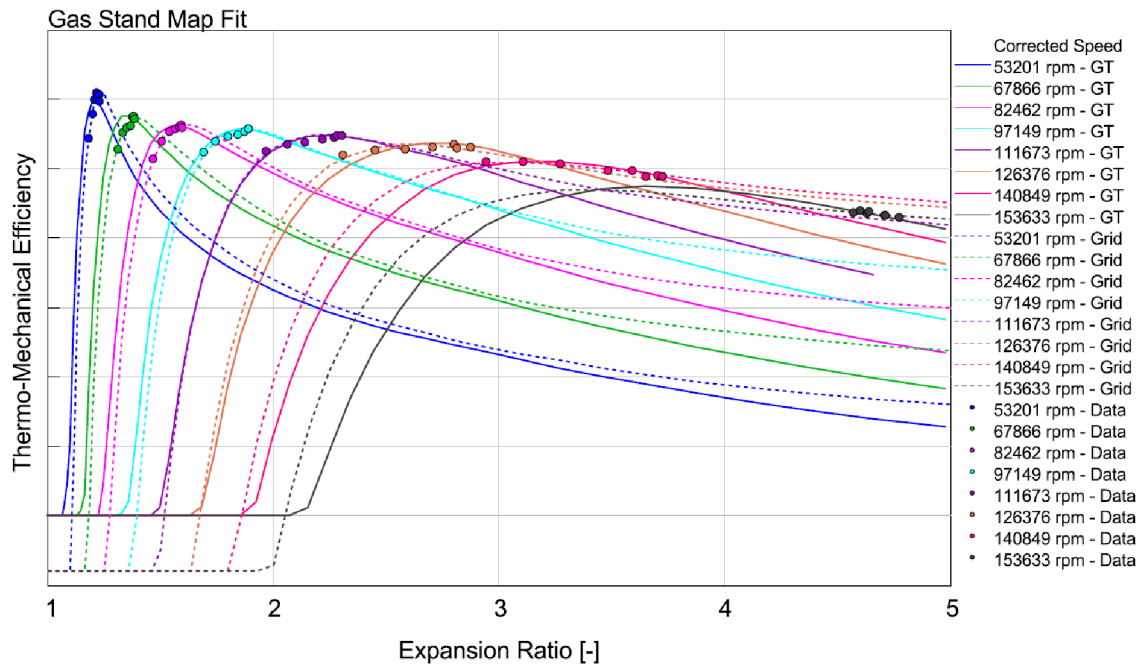


Figure 104: Efficiency maps for the default (full lines) & the proposed fits (dashed)

In terms of efficiency, the default and the proposed fits are similar (see Figure 104). The biggest difference is in the shift of the peak efficiency operating points with respect to expansion ratio, which is caused by the specific optimum blade speed ratio fitting.

5.5.2 Steady-state performance with the dyno map

Mapping using a turbine dynamometer is different from a hot gas stand as explained in Chapters 1.1.4, 2.3.3 and 4.6. To compare the turbine models fitted using the default and the proposed algorithms, the same engine simulation is used as in Chapter 5.5.1.

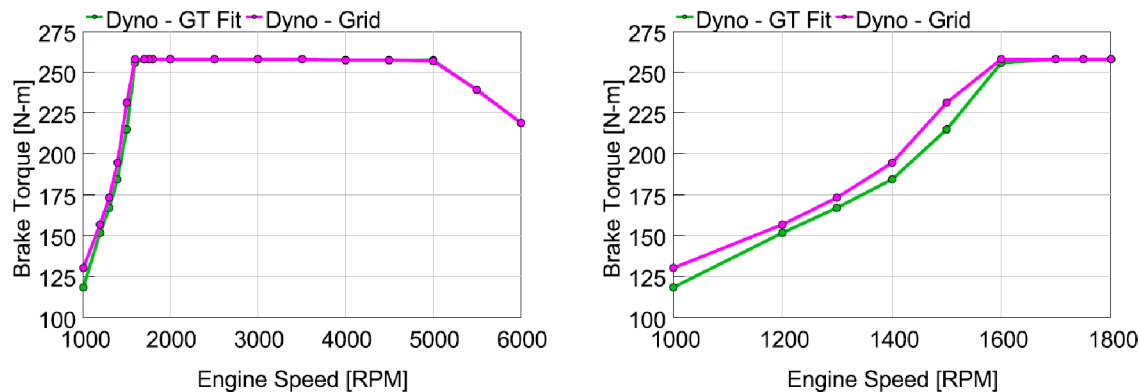


Figure 105: Full load torque (green – the default fit, pink – the proposed algorithm)

The impact of a fitting method on the achievable low-end torque is bigger with the dyno map compared to the case of the gas stand map in the previous chapter (see Figures 100 & 105). The biggest difference can be observed at 1500 rpm, where it is as high as 16.5 Nm or 7.7%. Such a gap is already significant and needs to be further analysed.

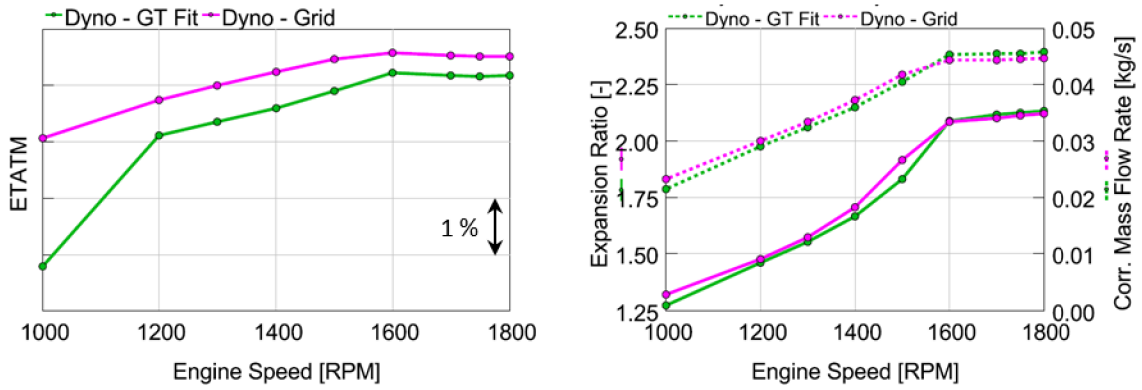


Figure 106: Turbine efficiency (ETATM), expansion ratio & corrected mass flow rate

A non-negligible difference between the two map fits can be observed with respect to both efficiency and mass flow rate (see Figure 106). In this case, however, an increased expansion ratio correlates with a higher corrected mass flow rate, which suggests that efficiency might be the main driver of the low-end torque misalignment.

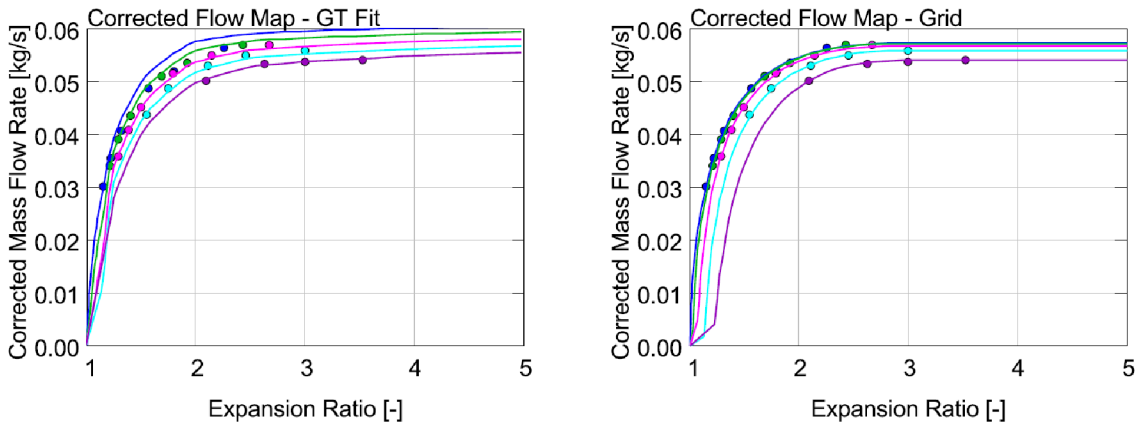


Figure 107: Comparison of the default (left) and the proposed (right) fits

Speed lines are condensed again at low expansion ratios in the default fit of corrected mass flow rate (see Figure 107). The centrifugal effect is, therefore, not properly captured, which was the case with the gas stand map too (see Figure 102).

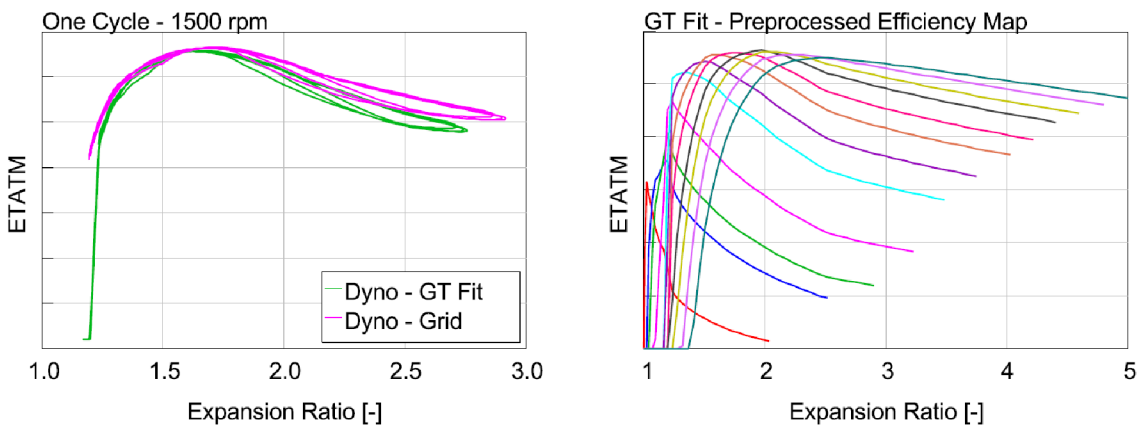


Figure 108: Instantaneous turbine operating points during one engine cycle (left) and the extrapolated efficiency map as per the default fit (right)

Plotting of the instantaneous turbine efficiency during one engine cycle showed that the default fit features an unusual drop at low expansion ratios (see Figure 108).

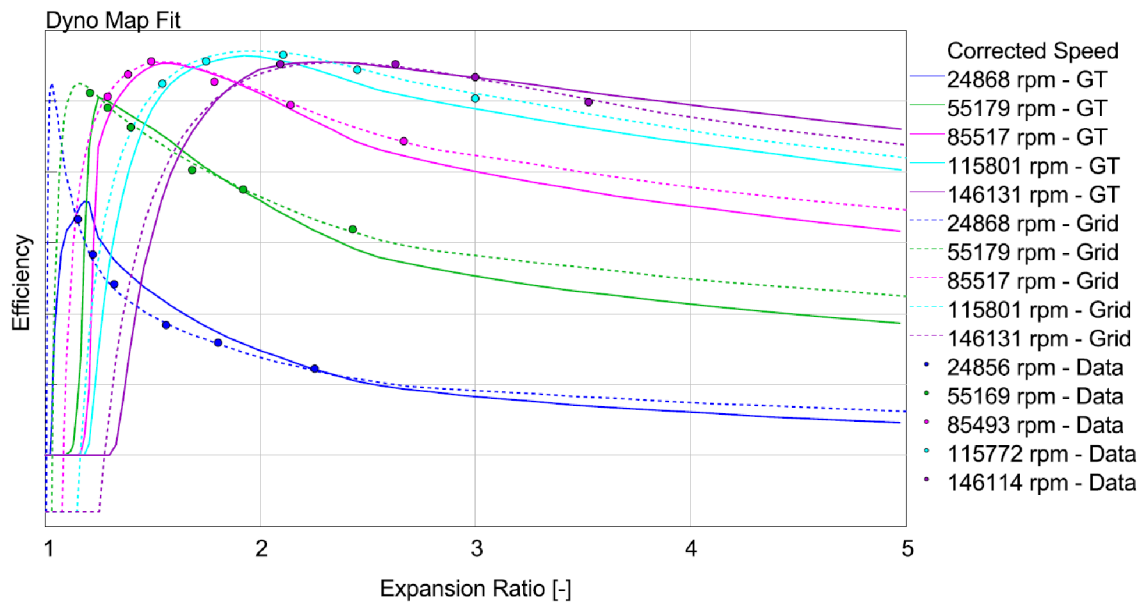


Figure 109: Efficiency maps for the default (full lines) & the proposed fits (dashed)

With the default algorithm, maximum turbine efficiency is fitted in such a way that the highest measured point at any speed line is not exceeded. This enables a conservative extrapolation, but it may be a disadvantage in the cases, when the maximum efficiency is not captured by the measurement at one or more speed lines (see Figure 109).

5.5.3 Transient load step with the gas stand map

The speed of a turbocharged engine response to a load step request is critical to the driver’s perception of a car’s dynamics. At the same time, simulation of transient turbocharger performance is rather challenging, because the initial spinning speed is low, while the turbine is fully loaded. This is a difficult-to-capture combination for conventional mapping techniques and substantial extrapolation must be applied. For consistency of the results, the same engine model is used as in the full-load simulations.

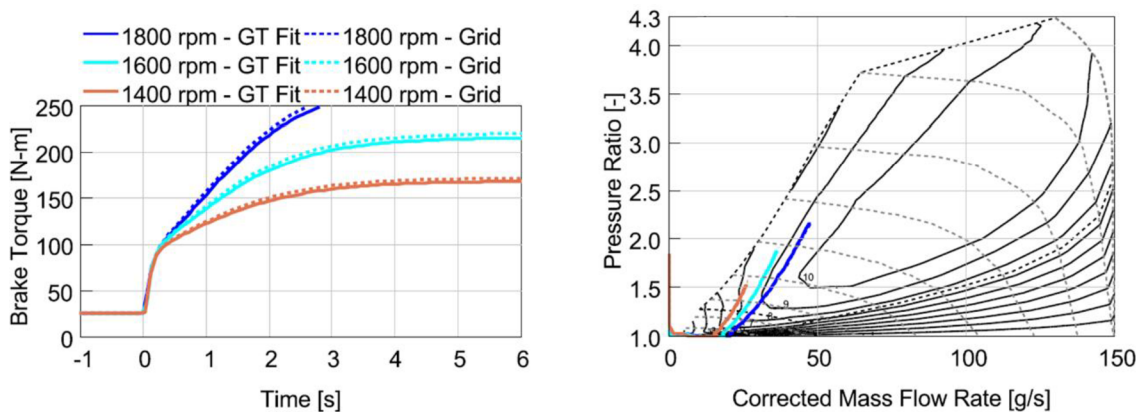


Figure 110: Engine brake torque (left) and compressor operating points (right) at a constant engine speed (gas stand map)

Overall, the transient performance with the default and the proposed fitting of the gas stand map is very similar, which, together with the steady-state comparison, confirms a good agreement between both methods (see Figures 100 & 110). Despite that, a small advantage can still be identified with the proposed fitting algorithm.

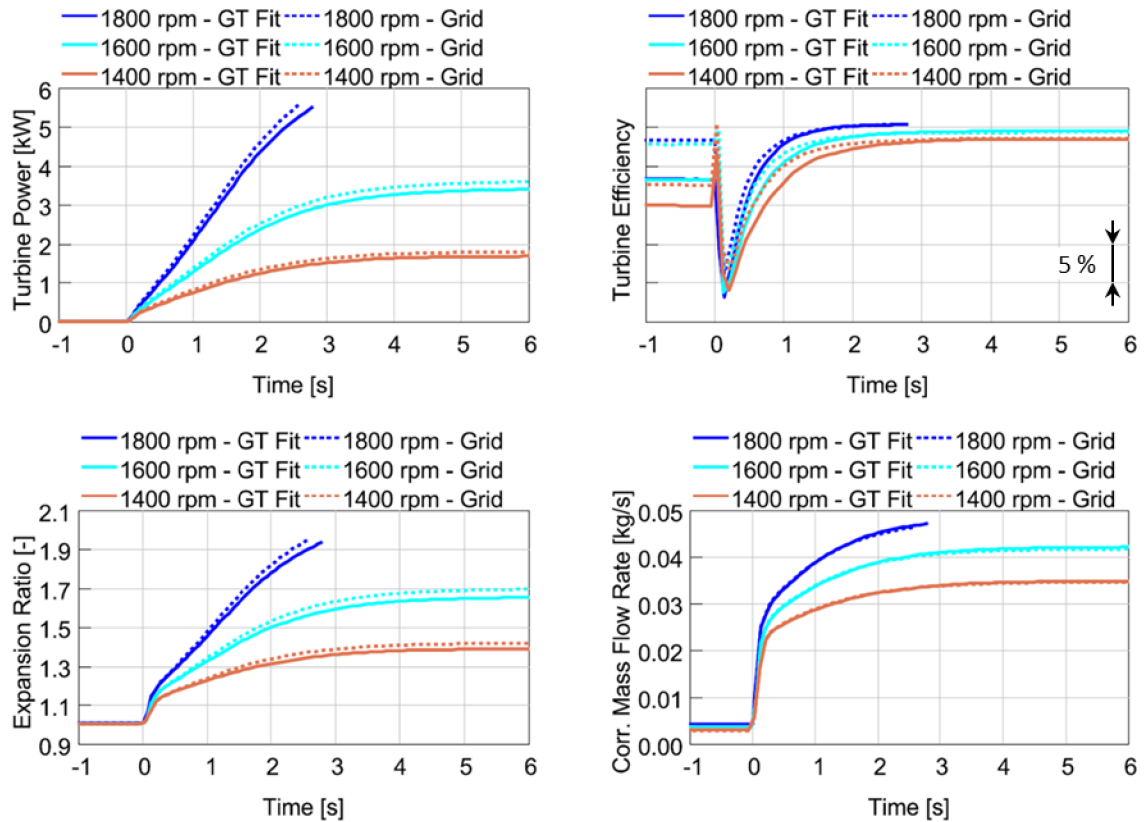


Figure 111: Turbine performance during the transient operation (gas stand map)

A detailed analysis of the transient turbine operation leads to a conclusion that the advantage of the grid map is caused by higher efficiency in the beginning of the load steps and by higher expansion ratio in the end. The first is due to a difference in the fitted efficiency at expansion ratios above the peak-efficiency point at each speed line, where the turbine generates the biggest power during pulsating operation (see the difference in Figure 104). Higher expansion ratio in the end of the transient engine load steps with the grid map is caused by both higher spinning speed (the better performing turbocharger spools up faster) and by the difference in corrected mass flow rate maps (see Figure 102).

5.5.4 Transient load step with the dyno map

The same engine model is used for the simulation of transient engine load steps with the dyno map (compare to Chapter 5.5.3). In this case, however, a much bigger difference can be recognized between the speed of brake torque increase with the default and the proposed fits. Nevertheless, an interesting conclusion is that the transient engine performance simulated with the turbine maps obtained by the hot gas stand and the dynamometer measurement is comparable (see Figures 110 & 112).

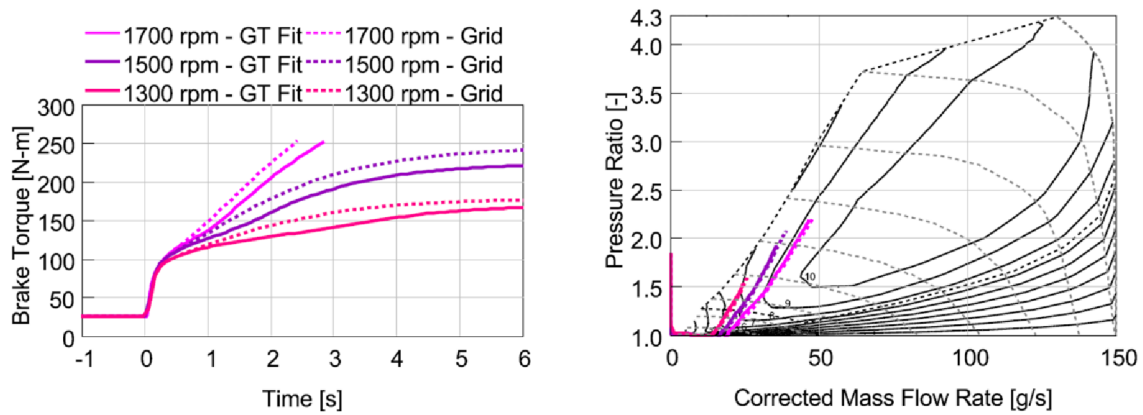


Figure 112: Engine brake torque (left) and compressor operating points (right) at constant engine speed (dyno map)

The default fitting of the dyno map results in a bit slower response at all engine speeds. A detailed view at the instantaneous turbine performance during the transient load steps is provided in Figure 113.

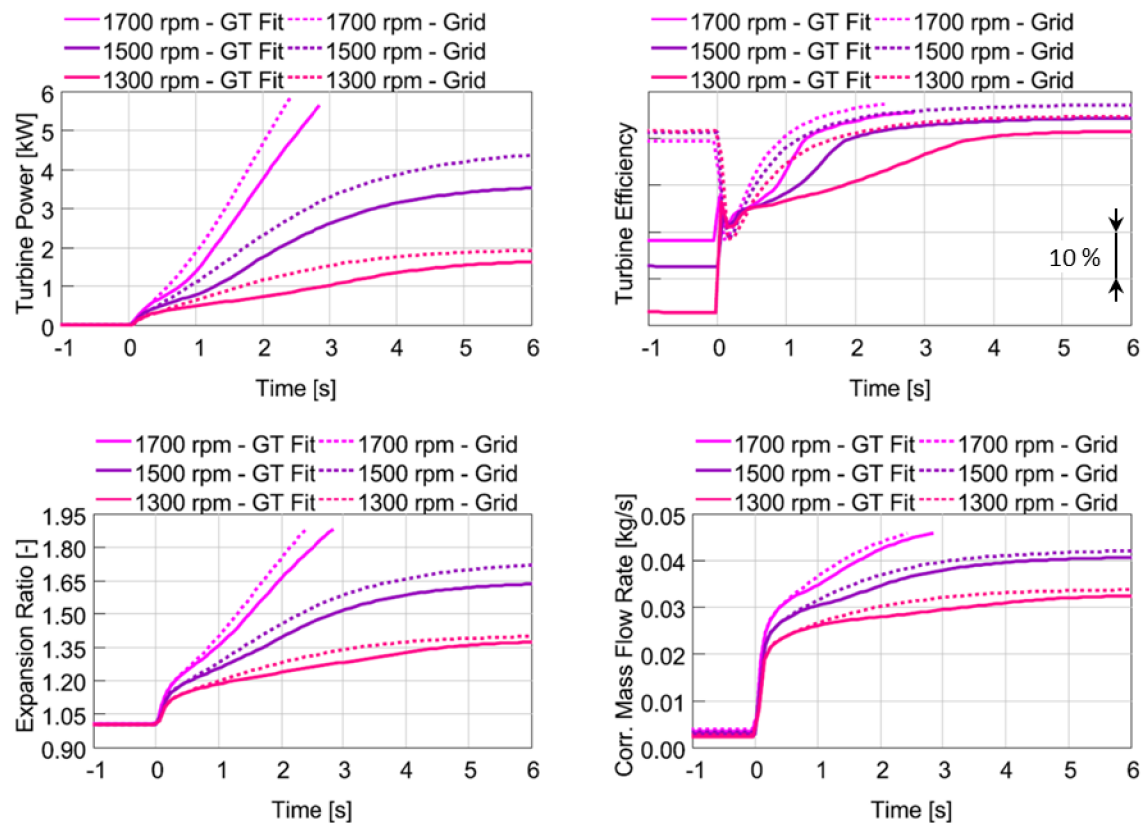


Figure 113: Turbine performance during the transient operation (dyno map)

Turbine efficiency increases very slowly with the default fit in the beginning of the engine load steps (see Figure 113). This is caused by the unwanted limitation of the maximum efficiency at low corrected speeds as identified in Chapter 5.5.2. After the rotor speed increases, turbine efficiency sharply recovers to an expected level. However, the delay already caused the engine brake torque to rise more slowly compared to the case of the dyno map fitted by the proposed algorithm.

CONCLUSION

At the beginning of this dissertation project was the need for a tool that would facilitate postprocessing of measured turbine maps of automotive turbochargers. This involves performance data management in the first place, but also its visualisation and numerical treatment to enable back-to-back comparisons. Furthermore, to assess the differences at equal operating conditions, efficiency and corrected mass flow rate must be interpolated or extrapolated depending on the distribution of measured operating points. Therefore, the input data must first be fitted by a convenient turbine model.

The implementation of a turbine fitting algorithm is the main objective of this work. For that purpose, a MATLAB™ application has been developed, which enabled testing of different numerical procedures. The first step was to understand the existing industrial practice and use it to establish the baseline method (also studied in [A1]). The algorithm included in GT-SUITE™ was chosen, because it represents a state-of-the-art solution that is widely used in the industry. However, the process is not exhaustively documented in available information sources, so custom procedures had to be proposed where necessary (see [10, 20]). Therefore, the baseline turbine fitting method, as implemented in the MATLAB application, is not fully representative of the one integrated in GT-SUITE. Nevertheless, it was possible to conclude that the declared linear relationship between the optimum blade speed ratio and the expansion ratio does not allow the proper extrapolation of the corrected mass flow rate. This was the main motivation for the development of a custom process.

The main difference between the proposed and baseline turbine models is that the new model features the *choke phenomenon*. Consequently, optimum blade speed ratio is limited above the critical expansion ratio in such a way that optimum corrected speed remains constant. Also, emphasis is placed on the implementation of physics principles to improve the fidelity of extrapolation. The theory of *radial equilibrium* is used to quantify the effect of centrifugal force on the corrected mass flow rate at low expansion ratios. Further, by the new structure of characteristic functions, it is ensured that corrected mass flow rate at each speed line is non-decreasing with expansion ratio. That is the expected behaviour based on an analogy with the discharge through an *ideal nozzle*.

Thanks to the application of *optimization methods* to identify the properties of turbine performance models, it is possible to estimate the maximum efficiency in situations, where this maximum is not included among input data points. The mechanism is based on the assumption that minimization of fit error at sub-optimal operating points can be used to determine the maximum efficiency at the same expansion ratio. Repetitive refinement of this relationship during the complete fitting process ensures reasonable results without impacting convergence.

Initial testing confirmed that the method is functional and robust when fitting the outputs of hot gas stand and turbine dynamometer measurements. With the help of a higher-level approximation, it is possible to visualize performance trends related to the variability of the A/R parameter. A similar approach is followed to plot the relationship between maximum efficiency and optimum corrected mass flow rate across multiple turbine sizes. As the last step, exported turbine performance models are used within

engine steady state and transient load step simulations in GT-SUITE (in the so-called *grid* format). In the case of the sample gas stand map, both algorithms (GT-SUITE default and the proposed one) result in similar engine performance at steady state and transients. However, with the default fit of the dyno map, transient engine performance is compromised by overly conservative efficiency extrapolation to low corrected turbine speeds.

The further evolution of the proposed turbine fitting procedure will involve mainly a refinement of the middle part of the optimum blade speed ratio spline (the section between the transition and the choke points in Figure 81). As per the current definition, the end-slopes are controlled, but the curvature is not. Besides, the MATLAB application will be extended with additional post-processing features. As of now, variable nozzle geometry, twin-scroll and sector-divided technologies are not supported, but the proposed methodology is well suited for this extension. A strong new trend calls for a separate treatment of the different aspects of turbocharger modelling. Namely, the heat transfer and bearing friction, both of which are normally included in compressor and turbine maps obtained by hot gas stand measurements. It will be advantageous to remove and model these effects independently to use gas stand maps in simulations.

REFERENCES

- [1] HEYWOOD, J. B. *Internal Combustion Engine Fundamentals*. 1st ed. New York: McGraw-Hill, 1988. ISBN 007028637X.
- [2] WATSON, N., JANOTA, M. S. *Turbocharging the Internal Combustion Engine*. 1st ed. London: The Macmillan Press Ltd., 1982. ISBN 0333242904.
- [3] BAINES, N. *Fundamentals of Turbocharging*. 1st ed. Vermont: Concepts NREC, 2005. ISBN 0933283148.
- [4] KADRNOŽKA, J. *Lopatkové stroje*. 1st ed., edited. Brno: Akademické nakladatelství CERM, 2003. ISBN 80-720-4297-1.
- [5] HIERETH, H. and PRENNINGER, P. *Charging the internal combustion engine*. 1st ed. Wien: Springer-Verlag, 2007. ISBN 9783211330333.
- [6] KLAPKA, J. *Metody operačního výzkumu*. 2nd ed. Brno: VUTIUM, 2001. ISBN 80-214-1839-7.
- [7] ČERMÁK, L. and HLAVIČKA, R. *Numerické metody*. 2nd ed. Brno: Akademické nakladatelství CERM, 2008. ISBN 978-80-214-3752-4.
- [8] KARPÍŠEK, Z. *Matematika IV: statistika a pravděpodobnost*. 3rd ed., appended. Brno: Akademické nakladatelství CERM, 2007. ISBN 978-80-214-3380-9.
- [9] PAVELEK, M. *Termomechanika*. Brno: Akademické nakladatelství CERM, 2011. ISBN 978-80-214-4300-6.
- [10] PESYRIDIS, A., SALIM, W. S-I. W. and MARTINEZ-BOTAS, R. F. Turbocharger Matching Methodology for Improved Exhaust Energy Recovery. In *Institution of Mechanical Engineers: 10th International Conference on Turbochargers and Turbocharging, 15-16 May, 2012*. Cambridge: Woodhead Publishing Ltd., 2012. p. 203-218. ISBN 9780857096135.
- [11] THEOTOKATOS, G. and KYRTATOS, N. P. Diesel Engine Transient Operation with Turbocharger Compressor Surging. *SAE Technical Paper 2001-01-1241*, 2001, ISSN 0148-7191, DOI 10.4271/2001-01-1241.
- [12] SHAABAN, S. and SEUME, J. Impact of Turbocharger Non-Adiabatic Operation on Engine Volumetric Efficiency and Turbo Lag. *International Journal of Rotating Machinery*, 2012, vol. 2012, Article ID 625453, DOI 10.1155/2012-625453.
- [13] CERDOUN, M. and GHENAIET, A. Unsteady behaviour of a twin entry radial turbine under engine like inlet flow conditions. *Applied Thermal Engineering*, 2018, vol. 130, p. 93-111. ISSN 1359-4311, DOI 10.1016/j.applthermaleng.2017.11.001.
- [14] LÜDDECKE, B., FILSINGER, D. and BARGENDE, M. On Wide Mapping of a Mixed Flow Turbine with Regard to Compressor Heat Flows during Turbocharger Testing. In *Institution of Mechanical Engineers: 10th International Conference on Turbochargers and Turbocharging, 15-16 May, 2012*. Cambridge: Woodhead Publishing Ltd., 2012, p. 185-202. ISBN 9780857096135.

- [15] BOZZA, F. and DE BELLIS, V. Steady Modeling of a Turbocharger Turbine for Automotive Engines. *ASME Journal of Engineering for Gas Turbines and Power*, 2014, vol. 136, issue 1. ISSN 0742-4795, DOI 10.1115/1.4025263.
- [16] DE BELLIS, V., BOZZA, F., SCHERNUS, C. and UHLMANN, T., Advanced Numerical and Experimental Techniques for the Extension of a Turbine Mapping. *SAE International Journal of Engines*, 2013, vol. 122, issue 3, p. 1771-1785. ISSN 1946-3936, DOI 10.4271/2013-24-0119.
- [17] JENSEN, J.-P., KRISTENSEN, A. F., SORENSON, S. C., HOUBAK, N. and HENDRICKS, E. Mean Value Modeling of a Small Turbocharged Diesel Engine. *SAE Technical Paper No. 910070*, 1991, ISSN 0148-7191, DOI 10.4271/910070.
- [18] SHEN, Y., LI, C., HEIMONEN, A., MEURMAN, J. H., NUNN, M. E., MILLER, D. R., VAN DYKE, T. E., BOLLU, P., KAAJA, R. and JANKET, S. A pilot study on maternal oral health and birth weight of twins. *Open Journal of Epidemiology*, 2014, vol. 4, p. 7-13. DOI 10.4236/ojepi.2014.41002.
- [19] SIRAKOV, B., CASEY, M. V. Evaluation of Heat Transfer Effects on Turbocharger Performance. In *Proceedings of the ASME 2011 Turbo Expo: Turbine Technical Conference and Exposition. Volume 7: Turbomachinery, Parts A, B, and C*. Vancouver, British Columbia, Canada. June 6–10, 2011. pp. 2075-2086. ASME. DOI 10.1115/GT2011-45887
- [20] GAMMA TECHNOLOGIES. *GT-SUITE: GT-SUITE Flow Theory Manual*. GT-SUITE v.2016, Gamma Technologies, LLC., Westmont, IL., US
- [21] AUSTRALIAN TURBO. *Turbocharger cutaway* [online]. 2014 [cited 2014-12-28]. Available at: <http://australianturbo.com.au/images/Blog/Blog%20Pictures/Cutaway.jpg>
- [22] WIKIPEDIA. *Flat spline* [online]. 2020 [cited 2020-11-17]. Available at: [https://commons.wikimedia.org/wiki/File:Spline_\(PSF\).png](https://commons.wikimedia.org/wiki/File:Spline_(PSF).png)
- [23] GAMMA TECHNOLOGIES. *GT-SUITE* [online]. 2020 [cited 2020-8-2]. Available at: <https://www.gtisoft.com>
- [24] MATHWORKS. *MATLAB* [online]. 2020 [cited 2020-8-23]. Available at: <https://www.mathworks.com>
- [25] MATHWORKS. *MATLAB SQLite 3 driver* [online]. 2019 [cited 2019-10-21]. Available at: https://uk.mathworks.com/matlabcentral/fileexchange/57123-kyamagu-matlab-sqlite3-driver?s_tid=srchtitle
- [26] CONCEPTS NREC. *RITAL* [online]. 2021 [cited 2021-6-27]. Available at: <https://www.conceptsnrec.com/solutions/software/computer-aided-engineering/preliminary-design/rital>

LIST OF AUTHOR'S PUBLICATIONS

- [A1] VONDRÁK, A. Fitting & Extrapolation of Turbine Performance Maps of Automotive Turbochargers. In LENHARD, R. and KADUCHOVÁ, K., eds. *XXII. International Scientific Conference - The Application of Experimental and Numerical Methods in Fluid Mechanics and Energy, Piestany, Slovakia, 7-9 October, 2020*. published online: MATEC Web of Conferences, 2020, vol. 328, DOI 10.1051/mateconf/202032803010
- [A2] POHOŘELSKÝ, L., VONDRÁK, A., TURNER, N., LUARD, N., COOPER, B., LANE, A., OSBORNE, R. The coupling of Advanced Gasoline Combustion and a fast-transient Boost System to produce a Low CO₂ vehicle Concept. In Zellbeck, H., ed. *23. Aufladetechnische Konferenz, Dresden, Germany, 20-21 September, 2018*. Dresden: TU Dresden, 2018. s. 397-422.
- [A3] POHOŘELSKÝ, L., VONDRÁK, A., CHOBOLA, P., JECKEL, D., DAVIES, P. RDE and CO₂ Relevant Boosting Technologies for Passenger Cars. In Zellbeck, H., ed. *22. Aufladetechnische Konferenz, Dresden, Germany, 28-29 September, 2017*. Dresden: TU Dresden, 2017. p. 133-152.
- [A4] VONDRÁK, A., ŠPIČÁK, M., BUCHTA, M. Turbocharged Single Cylinder as a Promising Formula Student Powertrain. *ATZ Extra*, November 2016, vol. 1, p. 42-50. ISSN: 1862-1791.
- [A5] VONDRÁK, A., POHOŘELSKÝ, L., ROUX, J. S. Advanced Boosting for EU6d Gasoline Engines. In *European GT Conference 2016, Frankfurt, Germany, 17-18 October, 2016*. Westmont: Gamma Technologies, LLC., 2016. Available at: <https://www.gtisoft.com/wp-content/uploads/2016/11/Honeywell-Advanced Boosting for EU6d Gasoline Engines WEB.pdf>
- [A6] VONDRÁK, A., ŠPIČÁK, M., JANOUŠEK, M. Turbocharging a single cylinder engine. In PÍŠTĚK, V., ed. *KOKA 2016, Brno, Czech Republic, 5-6 September, 2016*. Brno: VUT Brno, 2016, p. 241-248. ISBN: 978-80-214-5379-1.
- [A7] VONDRÁK, A., LANSKÝ, L., POHOŘELSKÝ, L., FINDEJS, J. Design of OnRAMP Model Predictive Control for On-Engine and GT-Power Transient Validation. In PÍŠTĚK, V., ed. *KOKA 2016, Brno, Czech Republic, 5-6 September, 2016*. Brno: VUT Brno, 2016, p. 231-240. ISBN: 978-80-214-5379-1.

DEFINITIONS/ABBREVIATIONS

Symbol	Unit	Meaning
a	[-]	lower boundary of an interval
a	[m/s]	speed of sound
A	[m ²]	area (cross section)
A_n	[m ²]	orifice cross section area
b	[-]	upper boundary of an interval
b_{fit}	[-]	exponent of normalized efficiency fit
BSR	[-]	blade speed ratio
BSR_{cor}	[-]	blade speed ratio obtained using corrected speed and reference temperature
$BSR_{norm_ETA_int}$	[-]	normalized BSR at zero efficiency
$BSR_{norm_WT_int}$	[-]	normalized BSR at zero mass flow rate
BSR_{WT_int}	[-]	blade speed ratio at zero mass flow rate
c	[m/s]	fluid velocity in stationary frame of reference
\mathbf{c}	[m/s]	vector of fluid velocity in stationary frame of reference
C	[-]	polynomial coefficient
c_{fit}	[-]	coefficient of normalized efficiency fit
c_0	[m/s]	isentropic spouting velocity
c_m	[-]	constant part of normalized mass flow rate fit
c_p	[J/(kg·K)]	specific heat at constant pressure
c_u	[m/s]	circumferential component of fluid velocity in stationary frame of reference
d	[-]	first derivative of a function
d_w	[-]	smaller wheel diameter (turbine outlet or compressor inlet)
D_w	[m]	bigger wheel diameter (turbine inlet or compressor outlet)
D_m	[m]	mean-flow diameter of a wheel
D_T	[m]	turbine wheel diameter (inlet, mean-flow)
$ETATM$	[-]	thermo-mechanical turbine efficiency
\mathbf{F}	[N]	vector of fluid force acting on blades

$f(x)$	[-]	function value at location x
F_c	[N]	centrifugal force (acting on fluid element)
\mathbf{F}_f	[N]	vector of force acting on the fluid in a blade channel
$\mathbf{F}_{f_overall}$	[N]	vector of overall force acting on the fluid in a control volume
h	[J/kg]	specific enthalpy
h_d	[-]	discretization length
$\mathbf{H}(x)$	[-]	Hessian matrix at location x
$\dot{\mathbf{H}}_f$	[kg·m/s ²]	vector of momentum flux
$\dot{\mathbf{H}}_{f_overall}$	[kg·m/s ²]	vector of overall momentum flux in or out of a control volume
\mathbf{H}_f	[kg·m/s]	momentum vector of the fluid in a blade channel
H_u	[J/kg]	fuel lower heating value
I_{TC}	[kg·m ²]	rotor moment of inertia
k	[-]	constant
$L(x)$	[-]	Lagrange's polynomial value at location x
$l(x)$	[-]	Lagrange's fundamental polynomial value at location x
L_t	[-]	stoichiometric air-fuel ratio
\mathbf{M}	[N·m]	torque vector
m	[-]	natural number (summation limit)
m_{fit}	[-]	exponent of normalized mass flow fit
\dot{m}	[kg/s]	mass flow rate
\dot{m}_0	[kg/s]	mass flow rate through an ideal nozzle
\dot{m}_{cor}	[kg/s]	corrected mass flow rate
\dot{m}_{red}	[(kg/s)·(K ^{0.5} /Pa)]	reduced mass flow rate
Ma_c	[-]	Mach number of rotor inlet flow
Ma_u	[-]	Mach number of rotor circumferential speed
n	[-]	natural number (summation limit)
n_{cor}	[1/min]	corrected speed
n_e	[1/min], [rpm]	engine speed

n_{red}	[1/(min·K ^{0.5})]	reduced speed
NT	[1/min]	corrected turbine speed
n_{TC}	[1/min]	rotor speed
P	[W]	power
p	[Pa]	pressure
$P(x)$	[-]	polynomial value at location x
P_e	[W]	engine brake power
p_{int}	[Pa]	intake (manifold) air pressure
P_m	[W]	bearing friction loss power
p_R	[Pa]	pressure at radius R
PRC	[-]	pressure ratio on compressor
p_{ref}	[Pa]	reference pressure (1 bar for compressor, 1.01325 bar for turbine)
PRT	[-]	expansion ratio on turbine
P_{shaft}	[W]	shaft power (of a turbomachine)
q	[-]	constant
$q(x)$	[-]	function value at location x
r	[J/(kg·K)]	specific gas constant
r_{ref}	[J/(kg·K)]	reference specific gas constant (287 J/(kg·K) for air and 289 J/(kg·K) for burnt gas)
\mathbf{r}	[m]	location vector (radius)
R	[m]	radius
$R(x)$	[-]	regression function above x
r_d	[-]	data point deviation from fit (residual)
$r_{d_ordered}$	[-]	ordered residuals (ascending order)
$S(x)$	[-]	spline interpolant
t	[s]	time
T	[K]	temperature
T_{ref}	[K]	reference temperature (298 K for compressor, 288 K for turbine)
$Trim$	[-]	wheel trim
u	[m/s]	circumferential (rotor) velocity in stationary frame of reference

\mathbf{u}	[-]	unit vector
V_d	[m ³]	engine displacement volume
WT	[kg/s]	corrected turbine mass flow rate
x	[-]	independent variable (e.g. in a polynomial)
\mathbf{x}	[-]	vector of independent variables
y	[-]	function value
\mathbf{y}	[-]	vector of function values
α	[-]	coefficient
β	[-]	coefficient
$\boldsymbol{\beta}$	[-]	vector of unknown coefficients
β_{crit}	[-]	critical expansion ratio
γ	[-]	Specific heat ratio (Poisson constant)
γ_{ref}	[-]	Reference specific heat ratio (1.4 for air and 1.35 for burnt gas)
κ	[-]	ratio of numbers
η	[-]	efficiency
η_e	[-]	engine brake efficiency
η_{Tm}	[-]	turbine thermo-mechanical efficiency
η_V	[-]	engine volumetric efficiency
λ	[-]	air excess ratio
λ_d	[-]	selected point of a function domain of definition
μ_d	[-]	selected point of a function domain of definition
ρ	[kg/m ³]	density
ρ_{int}	[kg/m ³]	intake (manifold) air density
τ	[-]	number of crankshaft revolutions per engine cycle
Φ	[-]	system of basis functions
φ	[rad]	polar coordinate
$\varphi(x)$	[-]	basis function value at location x
$\boldsymbol{\omega}$	[rad/s]	angular velocity vector
ω_{TC}	[rad/s]	rotor angular velocity

Subscripts

Index	Meaning
1	inlet
2	outlet
i	summation index
j	summation index
k	summation index
air	for air
exh	for exhaust/burnt gas
C	compressor
T	turbine
tot	total
is	isentropic
opt	optimum
norm	normalized
min	minimum
max	maximum
mean	arithmetic mean
median	median
RMS	root-mean-square
MSE	mean-square error
RMSE	root-mean-square error